UNIVERSITY OF CALIFORNIA, SAN DIEGO

Thin Film Growth and Characterization of the Electron-doped Superconductor $Sm_{2-x}Ce_xCuO_{4-y}$

A dissertation submitted in partial satisfaction of the requirements for the degree Doctor of Philosophy

in

Materials Science and Engineering

by

Daniel Joseph Scanderbeg

Committee in charge:

Professor M. Brian Maple, Chair
Professor Dimitri N. Basov
Professor Sungho Jin
Professor Sunil K. Sinha
Professor Kenneth Vecchio

2007

The dissertation of Daniel Joseph Scanderbeg is approved, and it is acceptable in quality and form for publication on microfilm:

Chair

University of California, San Diego

2007

To mom and dad and my wife

Thank you for all your love, support, and encouragement

I love you

To give anything less than your best is to sacrifice the gift.

Steve Prefontaine

TABLE OF CONTENTS

LIST OF FIGURES

LIST OF TABLES

ACKNOWLEDGEMENTS

I would first like to thank my advisor, Brian Maple, for affording me the opportunity to work in his laboratory. Without him, I would not have been able to complete this body of work.

Huge thanks goes to my mom and dad for always being supportive and loving throughout all my endeavors despite the fact they thought, many a times, I was going to kill myself doing them. Meg, I don't know how I managed without you. You are amazing! Thank you for all you have given me. Thanks to Donica, Eddie, Darren and Kaitlin for always being there and I know I can always count on you. Thanks to all my family, for everything, I couldn't have done any of this without you.

I am grateful for all the friends I have made along the way, both in academics and athletics. I especially want to recognize and thank my old roommate Adrian. Adrian always had great words of wisdom and encouragement for me and accompanied me through our "Trial of Miles, and Miles of Trials". Adlar, thanks for putting up with me for 6+ hour bike rides, my crazy rants during those times, and incessantly wanting to drop the hammer. Jerry Rice, yes, THE Jerry Rice: we had some crazy adventures over the years and its been a blast. I also wish to thank Scotty for passing on the honor of "the picture". It has pulled me through and now, as I finish my graduate career, I must pass it on to the next chosen one. Thanks for the hill repeats, snaking me, and general fun times. I owe a great deal of gratitude to UCSD Master's very own Sickie, not only are you a great swim coach but life coach too. Also, thanks to the Big Blue crew who were always willing to jump in the snake pit at 11^{th} street, no matter the conditions. This list goes on but is way too long to list everyone and for that I apologize.

Thank you to all the members of the Maple lab who contributed in various ways to this project, side projects, general learning, or just fun. Ben Taylor was the other high T_c co-conspirator who assisted with different phases of this project,

participated in many discussions, accompanied me to the National High Magnetic Field Laboratory, and also proofread this thesis. Ryan Baumbach helped with modifications of the oxide chamber, thin film growths, and proofread this thesis as well. Nick Butch, Jason Jeffries, Todd Sayles, Bill Yuhasz, and Pei-Chun Ho were always willing to lend help and some time when I needed something or lent an ear when I needed to practice a presentation. Finally, there was our resident Canadian (which we didn't hold against him...too much), Johnpierre Paglione, who was instrumental in the thermal transport measurements, always open to questions, taught me a great deal in the past two years, and willing and able to help at all times. Thank you labbies!

I would also like to also acknowledge Ivan Schuller for allowing me to do the photolithography in his clean room. Also, thanks to all his lab members, especially Maribel Montoya and Javier Villegas for their guidance and help teaching me the ropes.

A great big thanks to the late Andy Pommer, from the physics machine shop, who taught me a great deal and instilled in me a great love of machining. Had he not done this, I might not have met my wife, whom I did actually meet for the first time in the physics machine shop while machining an accessory to the PLD chamber. You will always be remembered by Meg and me.

Thank you to the guys in the physics electronics shop; Clem Demmitt, Allen White, George Kassabian, and Mike Rezin who all aided me throughout my career with various assistance with electronic devices. Also, thanks to John Lasky and Dan McMullin in the chemistry stockroom who could always find exactly what I was looking for, even when I wasn't sure what "it" was.

I would also like to acknowledge Dr. Eric C. Palm, Mr. Timothy Murphy, and Mr. Glover Jones who assisted with instrumentation and operation at the National High Magnetic Field Laboratory (NHMFL), Tallahassee.

Finally, thank you to our funding agencies: The US Department of Energy, under Grant No. FG03-86ER-45230, and the Cular program, No. 9985-001.

A portion of the text and data in Chapter III is a reprint of the material as it appears in "Growth via Pulsed Laser Deposition and Characterization of Thin Films of the Electron-Doped Superconductor $Sm_{2-x}Ce_xCuO_{4-y}$," D. J. Scanderbeg, B. J. Taylor, and M. B. Maple, Physica C **443**, 38 (2006). The dissertation author was the primary investigator and author of this article.

VITA

2000	B.S. (Physics), University of California, San Diego
2000–2007	Research Assistant, University of California, San Diego
2001,2003	Teaching Assistant, Department of Physics University of California, San Diego
2001	M.S. (Physics with Specialization in Materials Physics), University of California, San Diego
2002	M.S. (Materials Science and Engineering), University of California, San Diego
2007	Ph.D. (Materials Science and Engineering), University of California, San Diego

PUBLICATIONS

"Characterization of the Electron-Doped Superconductor $Sm_{1.85}Ce_{0.15}CuO_{4-y}$ across the doping spectrum," D. J. Scanderbeg, R. E. Baumbach, J. Paglione, B. J. Taylor, K. T. Chan, and M. B. Maple, manuscript in preparation.

"Vortex Glass Scaling of the Electron-Doped Superconductor $Sm_{2-x}Ce_xCuO_{4-y}$," D. J. Scanderbeg, B. J. Taylor, R. E. Baumbach, K. T. Chan, and M. B. Maple, manuscript in preparation.

"Lattice dynamics in arsenic-based skutterudites PrT_4As_{12} (T = Fe, Ru, Os)," T. Sayles, J. Paglione, D. Scanderbeg, W. Yuhasz, T. Yanagisawa, M. B. Maple, and Z. Henkie, manuscript in preparation.

"Quantum Fluctuation, Critical Dynamic Vortex Motion, and the Vortex Solid-Liquid Transition," B. J. Taylor, D. J. Scanderbeg, M. B. Maple, C. Kwon, and Q. X. Jia, accepted Phys. Rev. B (2006).

"Growth via Pulsed Laser Deposition and Characterization of Thin Films of the Electron-Doped Superconductor $Sm_{2-x}Ce_xCuO_{4-y}$," D. J. Scanderbeg, B. J. Taylor, and M. B. Maple, Physica C **443**, 38 (2006).

"Effect of hole doping in $Li_xCu_{1-x}O$," X. G. Zheng, H. Yamada, Daniel J. Scanderbeg, M. Brian Maple, and C. N. Xu, Physical Review B **67**, 214516 (2003).

FIELDS OF STUDY

Major Field: Physics and Materials Science and Engineering
Studies in Superconductivity and Magnetism.
M. Brian Maple, Bernd T. Matthias Professor of Physics,
University of California, San Diego

ABSTRACT OF THE DISSERTATION

Thin Film Growth and Characterization
of the Electron-doped Superconductor $Sm_{2-x}Ce_xCuO_{4-y}$

by

Daniel Joseph Scanderbeg
Doctor of Philosophy in Materials Science and Engineering
University of California, San Diego, 2007
Professor M. Brian Maple, Chair

$Sm_{2-x}Ce_xCuO_{4-y}$ belongs to a class of materials known as electron-doped superconductors ($Ln_{2-x}M_xCuO_{4-y}$; Ln = Pr, Nd, Sm, Eu; M = Ce, Th) and has a moderately high superconducting critical temperature, T_c, of $\sim$ 20 K at optimal doping (x = 0.15). The trivalent rare earth site is doped with tetravalent Ce or Th; hence the name "electron-doped". $Sm_{2-x}Ce_xCuO_{4-y}$ also exhibits a unique magnetic structure at low temperatures (T < 6 K) due to the antiferromagnetic ordering of the Sm^{3+} ions. In this study, thin films of the electron-doped superconductor $Sm_{2-x}Ce_xCuO_{4-y}$ (SCCO) have been grown by pulsed laser deposition (PLD) for a cerium concentration range of x = 0.13 to x = 0.19. The films have been characterized through x-ray diffraction, electrical transport, and thermal transport measurements. A temperature versus cerium content (T-x) phase diagram has been constructed from the electrical transport measurements and yields a superconducting region similar to that of two of the other electron-doped superconductors $Nd_{2-x}Ce_xCuO_{4-y}$ and $Pr_{2-x}Ce_xCuO_{4-y}$. Thermopower measurements were also performed on the samples and show a dramatic change from the underdoped region (x < 0.15) to the overdoped region (x > 0.15). Additionally, the

standard Fisher-Fisher-Huse (FFH) vortex glass scaling model has been applied to the magnetoresistance data, as well as a modified scaling model (RRA), and the analysis yields values of the vortex glass melting temperature, T_g, and critical exponent, ν(z-1). A magnetic field versus temperature (H-T) phase diagram has been constructed for the films with cerium content $x \geq 0.14$, displaying the vortex glass melting lines. Magnetoresistance data taken as a function of angle, Θ, is also discussed in the context of the vortex glass scaling model.

I

Introduction

Since the invention of the laser in 1960, much research has been conducted regarding the laser-matter interaction. One of the spin-offs of this work is the subject we currently know as pulsed laser deposition (PLD). Thin film deposition by this method has now been around for about two decades and has clear advantages over other thin film deposition techniques, especially in regards to the high temperature superconducting cuprate oxides. This will be discussed further in a subsequent chapter.

Superconductivity, since its discovery in 1911 by H. Kamerlingh Onnes, is still at the forefront of research with many aspects yet to be discovered. A boom in research followed the discovery of high temperature superconductors (high-T_c) in the late 1980's with hopes of great technological applications. Despite considerable progress, many applications and room temperature superconductivity have yet to be realized. Today, there is still a heavy research emphasis on high temperature superconductivity. There is still much to be learned about these materials and the exploration of their properties will hopefully lead to a complete theoretical picture of the mechanism behind high temperature superconductivity.

The work presented here is a mesh of both fields, combining both the fabrication of thin films of the electron-doped superconducting compound $Sm_{2-x}Ce_xCuO_{4-y}$ (SCCO) by the PLD method, and also measurements of various physical properties aimed at grasping the basic underlying physics of high

temperature superconductivity in this compound.

$Sm_{2-x}Ce_xCuO_{4-y}$ is an interesting system to research for several reasons, one of which being that a complete phase diagram of the superconducting region has not been mapped out in single crystal or thin film form. Additionally, the Sm^{3+} ions in SCCO order antiferromagnetically below its Néel temperature $T_N \sim 6$ K into an arrangement never seen before in any other high-T_c material. Nd^{3+} in $Nd_{2-x}Ce_xCuO_{4-y}$ (NCCO) also orders antiferromagnetically, but it is in a different magnetic moment configuration, and at a lower temperature $T_N \sim 1.2$ K. Therefore, SCCO not only has an unusual antiferromagnetic magnetic structure coexisting with superconductivity, but it has a more readily accessed temperature region with $T_N \sim 6$ K, and allows the study of the effect of magnetic order on the superconducting vortex state. The interplay of superconductivity and magnetism is potentially important in the search for the pairing mechanism in the high T_c compounds. This could possibly provide further evidence that magnetic excitations are responsible for pairing [1, 2].

This project involved the design and development of a thin film deposition chamber for growth of oxide based thin films. Following construction of the chamber and setup of optics, PLD targets of $Sm_{2-x}Ce_xCuO_{4-y}$with varying x were synthesized, thin films were grown while the growth conditions were optimized, and finally the films were characterized through measurements including x-ray diffraction and electronic transport.

Chapter 1 serves as an introduction to both the laser ablation process and superconductivity so as to familiarize the reader for subsequent chapters on pulsed laser deposition (PLD) of superconducting thin films of SCCO. A brief background and fundamental principles governing both phenomena, will be presented before moving on to a more detailed discussion in Chapter 2 of the materials and methods used in this study. Chapter 3 contains the results and analysis obtained from experiments performed on the thin films. Chapter 4 consists of conclusions that can be drawn from this body of work as well as possible future directions for

continued work on SCCO.

I.1 Introduction to Laser Ablation

Soon after the invention of the first laser in 1960, experiments were conducted to observe the laser-solid interaction [3, 4], while additional experiments were performed on the laser-liquid [5] and laser-gas [6] interaction. Not long after these experiments, Smith and Turner [7] were the first to demonstrate the deposition of a thin film using a laser ablation method. The two major breakthroughs that contributed to the boom in pulsed laser deposition of thin films were: 1) invention of the Q-switch, leading to a short pulse, high power output of the laser, and 2) the first successful growth of a high temperature superconducting thin film [8]. The Q-switch was important since it allowed for short pulse duration with high peak pulse power, meaning that the laser could be used to break down materials into a plume, given sufficient power. This plume can contain electrons, ions, atoms, molecules, clusters, solid particulates, and molten globules. Additionally, the short duration laser pulses coupled with shorter wavelength laser radiation provided for more congruent melting of the target and thus transfer of the target stoichiometry to the substrates.

Theory of the laser ablation process has been driven by experiment. Theoretical modelling of the process has been challenging with no model able to perfectly describe all the phenomena observed during ablation. Many proposals were set forth concerning this interaction and before long, it was found that a complete theoretical picture of the laser-target interaction was extremely complex. Even with no complete picture, it is commonly agreed upon that the process involves the following multiple absorption processes: volume absorption by the electrons and phonons in the lattice, absorption at the surface, and absorption by the plume ejected from the target surface.

A qualitative overview of the idealized absorption and ablation process

can be described as follows:

1) The laser beam strikes the target material being ablated and photons are absorbed at the surface creating a molten layer of material (Knudsen Layer).

2) The material is vaporized and molten droplets are expelled from the surface due to a high recoil pressure from the vaporization.

3) Ejected material in the plume is struck with the incoming laser beam increasing the energy of the plume constituents.

Breaking these down further, we have a more thorough qualitative explanation that begins with the laser radiation absorption at the surface of the target raising the atoms and molecules into excited states. These excited species can either photodesorb or relax by releasing phonons. If they produce phonons rapidly enough, the surface will have temperature spikes capable of evaporating the target surface. As the target material evaporates and is released, a dense layer of particles above the target is formed, the Knudsen layer. In this region, the particles leaving the target experience a large number of collisions with the resulting particle flux almost entirely normal to the surface of the target. This dense plasma layer allows some passage of the UV photons to continue ablating the target while some photons are directly absorbed by the plasma. In this picture, one can see that laser fluence is an important parameter in film growth and also target to substrate distance since particles reaching the substrates must have the energy of formation to form the correct phase. There are, however, numerous other growth parameters involved in growing a film with the proper phase and this is addressed in the following section.

I.2 Introduction to Thin Film Growth

The growth of thin films by pulsed laser deposition (PLD) is a complicated process, not only because of the laser-solid target interaction and the underlying dynamics, but also because of the multidimensional phase space governing the

quality of the thin film growth. Even with these complexities, PLD is very versatile and has several advantages over other film growth methods including, but not limited to: growth in a reactive gas environment, complex multilayers, applicability to many systems, and fast growth/turn around times. Epitaxially grown thin films are excellent for experiments such as electrical transport measurements. Thin films can be easily patterned into known geometrical configurations so as to accurately measure the electrical resistivity, Hall effect, thermopower, Nernst effect, etc., along a single crystallographic direction. Also, many of the films can be grown with much larger surface areas than flux grown single crystals, making the attachment of electrical contacts much easier and also proving useful for optical spectroscopy, x-ray and neutron studies, and penetration depth measurements. Thin films also open the possibility of growing multilayers and studying the properties of layered structures. Additionally, particular to this thesis, thin films of the electron-doped cuprate materials are particularly advantageous owing to the fact that the superconducting properties of these materials are extremely dependent on both the cerium concentration and also the oxygen concentration. The laser deposition process allows film deposition of the same homogeneous stoichiometry as that of the target material, meaning the correct Ce concentration. In-situ annealing can be used to properly reduce the electron-doped films as well, and once an optimized recipe for growth and annealing has been established, it can be repeated to produce films with proper oxygen reduction.

For thoroughness, the disadvantages of PLD should be addressed. One of the two major drawbacks of PLD is the fact that due to the high energy process, there is the possibility of large particulates being released from the surface of the target, referred to as splashing. It can therefore be difficult to get very smooth, particulate free film surfaces, but not impossible. Much research has been done in the area of splashing and reduction of particulates on the film surface. Since we are dealing with ceramic oxides in this thesis, only research pertaining to the high-T_c oxides will be discussed and cited. It has been shown in the high temperature

oxide superconductor $YBa_2Cu_3O_{7-\delta}$ (YBCO) that there is a threshold laser fluence below which particulates are unobservable [9]. However, above this threshold, particulates increase rapidly with increasing fluence until saturation at a higher fluence.

Laser wavelength is another parameter involved in splashing. Again, in YBCO, decreasing wavelength leads to an increase in the absorption coefficient, α, and decreasing penetration depth, which ultimately decreases the size and density of particulates [10]. Therefore, ultraviolet (UV) lasers are the preferred choice for thin film growth, compared to other wavelengths, because of the high absorbtion, minimal reflection, and decrease of particulates in the UV wavelength.

Finally, ambient gas pressure in the deposition chamber and target to substrate distance will effect splashing. The pressure and target to substrate distance are coupled parameters and will be discussed later.

The second disadvantage of PLD is the difficulty in large area deposition; e.g., scale up for production of commercial products with large area films. This is mentioned for practicality but not addressed any further because this does not pertain to the research contained in this dissertation.

Physicists at the Cavendish laboratory began studying thin film growth around 1920. However, the flurry of work that resulted in experimental and theoretical development, as well as numerous publications, didn't occur until the 1950's and 1960's. By the 1970's there was a general consensus regarding the growth mechanisms. Three types of film growth and nucleation mechanisms described by Lewis and Anderson in 1978 [11] are: Volmer-Weber, Frank-van der Merwe, and Stranski-Krastanov. A brief introduction to each mechanism is outlined in the following paragraphs.

The Volmer-Weber mechanism is a deposition that results in three dimensional island formations on the surface of the substrate due to a higher cohesive energy between the deposited atoms than between the deposited atoms and the substrate. Frank-van der Merwe type growth is a two dimensional layered deposi-

tion, depositing only one monolayer of material at a time and resulting in a very smooth epitaxially grown film. This occurs when the cohesive energy of the deposited atoms is less than that of the deposited atoms and the substrate. Finally, Stranski-Krastanov film growth is a combination of the two previous growths, hence a mixed growth. It has the characteristics of beginning as Frank-van der Merwe type growth, but at some point, monolayer growth becomes less energetically favorable and the growth becomes a Volmer-Weber type growth. An illustration of the different growth methods is shown in Figure I.1.

The preferred method is a monolayer growth; hence, a Frank-van der Merwe type growth. However, this type of growth is often not possible, although growth conditions can be adjusted such as to encourage this type of growth. Successful growth requires proper species deposition on the substrate as well as enough surface mobility on the substrate, which is a function of several parameters: substrate temperature, substrate location, laser fluence, target to substrate distance, and pressure of the background gas in the deposition chamber.

I.3 Introduction to Superconductivity

In 1911, three years after first liquifying helium, the Dutch physicist H. Kamerlingh Onnes discovered superconductivity in mercury [12]. Onnes found that the electrical resistance dropped sharply to zero at a specific temperature. This specific temperature is defined as the superconducting critical temperature T_c, which is a characteristic of the material being measured. Perfect conductivity is one of the two defining characteristics of superconductivity, the second being perfect diamagnetism, which will be addressed below. His work marked the dawn of a new field of study in physics: superconductivity.

It was not long before superconductivity was discovered in other elements, then alloys, and finally compounds. However, it wasn't until 1933 that the other defining property of superconductivity was established: the Meissner effect. Meiss-

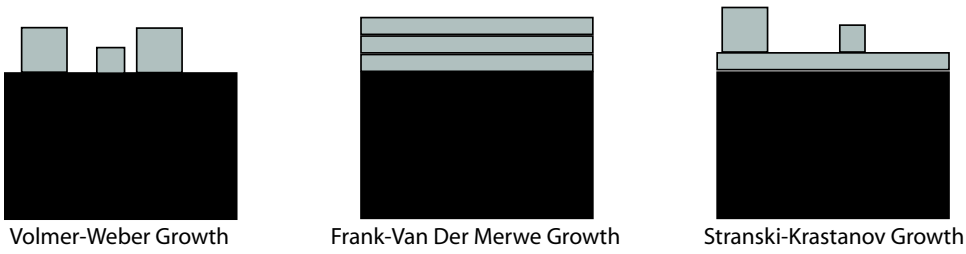

Figure I.1: The three common types of film nucleation and growth from [11].

ner and Oschenfeld found that a material in the superconducting state expels a magnetic field [13]. Two years later, in 1935, F. London and H. London put forth a quantitative description of superconductivity including superconducting electrons and an explanation of the Meissner effect [14]. The implications of the London equations are such that the magnetic field only penetrates into a superconducting material a particular depth, the penetration depth λ_L, the formula for which is given in Eqn. (I.1), and that surface currents exist in a superconducting material that screen out the applied magnetic field.

$$\lambda_L = \left(\frac{mc^2}{4\pi n_s e^2} \right)^{1/2} \tag{I.1}$$

An important step forward in the theory of superconductivity was made in 1950 by Ginzburg and Landau. The Ginzburg-Landau (GL) theory put forth a macroscopic description of superconductivity [15] but was largely overlooked until after Bardeen, Cooper, and Schrieffer published their now well known theory of superconductivity (BCS). Later, Gor'kov was able to show that GL theory was just a limiting form of BCS theory [16]. The major breakthrough in GL theory was the introduction of the complex order parameter Ψ, which can be thought of physically as the wavefunction describing the center of mass of a Cooper pair.

A complete theoretical description of superconductivity remained elusive for many years until BCS theory, which is described in the next section, I.3.1. This remained as a satisfactory theoretical description of the classical superconductors until the discovery of high temperature superconductivity in 1986 by Bednorz and M*ü*ller [17]. With the discovery of these new high-T_c compounds, there was an intense surge in the field and new materials with even higher critical temperatures were rapidly discovered.

One can see the incredibly rapid increase in superconducting critical temperature T_c when plotted versus the year of discovery, shown in Fig. I.2 [18]. These new high temperature superconductors belong to a class of materials known as type II superconductors and are discussed in section I.3.2. Finally, a brief introduction

is given to vortex-glass scaling in section I.3.3 following the work of Fisher, Fisher, and Huse [19]. For a more rigorous coverage of superconductivity the reader is referred to an undergraduate level introduction by Kittel [20] or to a more advanced discussion by Tinkham [21] or Benneman [22].

I.3.1 BCS Theory of Superconductivity

John **B**ardeen, Leon **C**ooper and Robert **S**chrieffer (**BCS**) put forth the first complete description of superconductivity in 1957 [23], which earned them the Nobel Prize in Physics in 1972. The BCS theory, in the simplest qualitative picture, has electrons condense into Cooper pairs under the influence of an attractive interaction. Normally, in a material described by a Fermi gas environment, electrons would strongly repel each other via the Coulomb force and, in a simple picture, as the electrons move through the material energy is lost through "collisions" with the lattice; however, it was postulated that in a material, even a weak attractive interaction would be sufficient to bind together two electrons. These two electrons form the Cooper pair and have dissipation free motion through the lattice. All the Cooper pairs condense into a single state that is phase coherent and there is an isotropic energy gap Δ that is formed near the Fermi energy ϵ_F. The BCS coherence length ξ_o represents the size of the Cooper pair and is related to the energy gap:

$$\xi_o = a\frac{\hbar v_F}{k_B T_c} = \frac{\hbar v_F}{\pi \Delta(0)} \tag{I.2}$$

where a = 0.18, v_F is the Fermi velocity, T_c is the superconducting critical temperature, and Δ is the energy gap.

BCS theory does not specify the attractive interaction, only that one is needed. One such interaction is the electron-phonon interaction. In the simplest picture of classical superconductors, imagine a negatively charged electron moving through a crystalline lattice. The positively charged ions will be attracted to the electron and be displaced from their equilibrium position as they move towards the

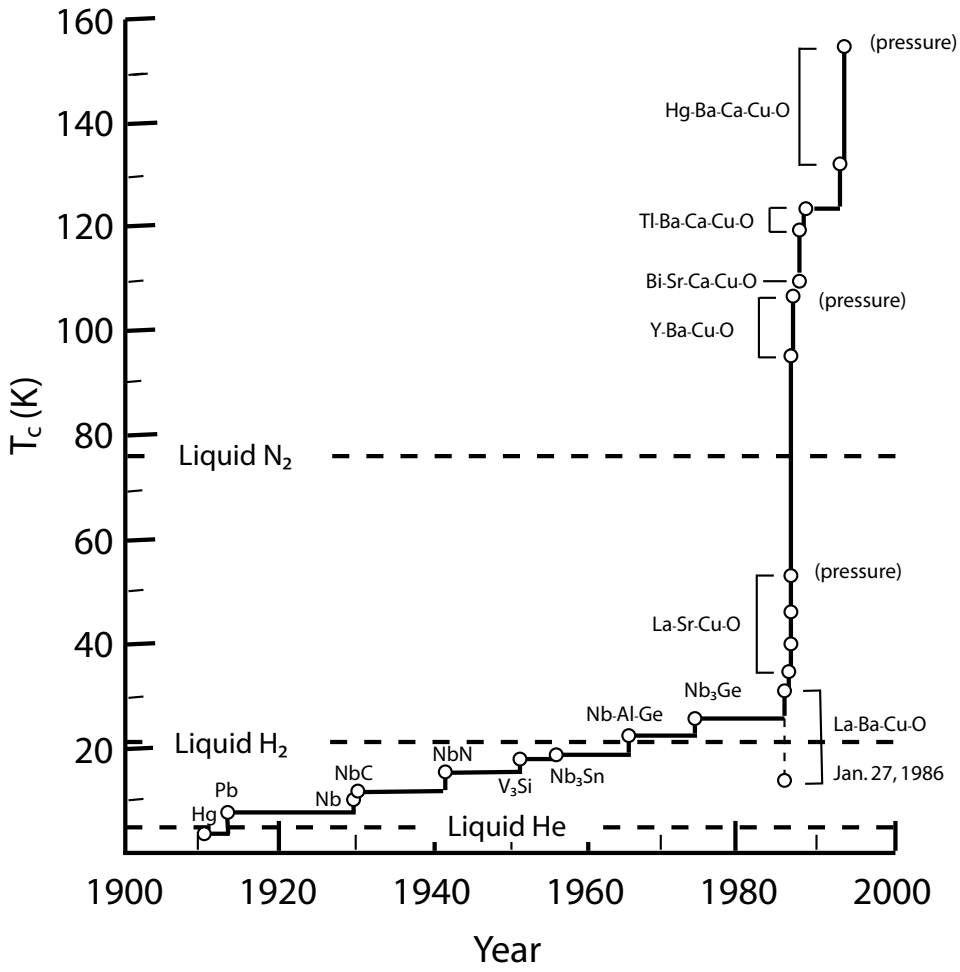

Figure I.2: Superconducting critical temperature T_c versus year discovered from [18].

electron. After the electron has passed, there will be a net positive charge in the region of the displaced ions before they have relaxed; thereby attracting a second electron, effectively binding the two electrons together, resulting in a Cooper pair.

I.3.2 Type I Superconductivity

Superconductors are divided into two classes, Type I and Type II. Type I superconductors are those in which there is no bulk penetration of an external magnetic field into the material while it is in the superconducting state; $T < T_c$ and $H < H_c$. An applied external magnetic field only penetrates the sample to the London penetration depth λ_L, as supercurrents are established on the outer "skin" of the material, which build up a magnetization equal and opposite to the applied magnetic field. The Meissner effect, or perfect diamagnetism, introduced earlier, was one of the two defining characteristics of a superconductor along with perfect conductivity. This is shown graphically in Figure I.3. In Fig. (I.3a), one can see the sample will be in the Meissner state below the superconducting region formed by the temperature and applied magnetic field. Another way to look at this is the internal magnetic field versus applied magnetic field, shown in Fig. (I.3b). Again, one can see that the internal magnetic field of the superconductor is zero up to the critical field H_c at which time the superconductor becomes normal and the magnetic field can penetrate the sample. A Type II superconductor is different from a Type I, in that it allows the penetration of the applied magnetic field in a very specific way and will be discussed in the next section.

I.3.3 Type II Superconductivity

In the same year as BCS theory (1957), Alexi Abrikosov published a paper based on GL theory that theorized a new class of superconductors [24], which he dubbed "Type II superconductors". The key feature of these new materials was the penetration of magnetic flux into the material at a lower critical magnetic field H_{c1}. However, this new class of materials exhibited not one, but two, distinct

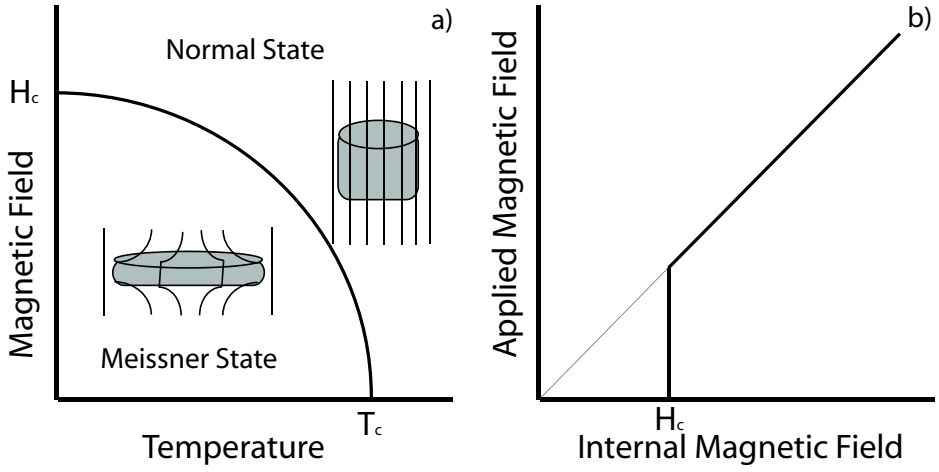

Figure I.3: Type I superconductivity. a) Cartoon picture of a sample displaying flux expulsion in the Meissner state below H_c; and penetration of the magnetic field into the sample in the normal state above H_c. b) Behavior of the applied magnetic field versus internal field. Due to the flux expulsion in the Meissner state, there is no field penetration into the sample until it becomes normal at H_c.

critical magnetic fields, H_{c1} and H_{c2}. Below the lower critical magnetic field H_{c1}, the superconducting material behaves the same as a Type I superconductors, expelling the applied magnetic field. Remarkably, above the lower critical field but below the upper critical field, $H_{c1} < H < H_{c2}$, the material allows the penetration of the applied magnetic field in quantized vortices without the loss of bulk superconductivity. Each vortex has a normal core that allows the magnetic field to pass through and is surrounded by a shielding supercurrent, screening out the magnetic field locally, analogous to the screening of the bulk in Type I superconductors described above. An illustration of Type II superconductors is shown in Figure I.4. One can see in Fig. (I.4a), that below H_{c1} is the usual Meissner state, like that found in Type I superconductors. However, above H_{c1} but below H_{c2}, is the mixed state with magnetic flux penetration through the sample before coming to H_{c2}, above which superconductivity is destroyed and the sample becomes normal. The vortices are arranged in a regular lattice in the mixed state. Although originally described as a square lattice, it was later shown that a triangular lattice has a lower energy and the vortex lattice has been confirmed experimentally [25–27]. Each vortex carries a fixed value of flux, the single flux quantum Φ_o given by:

$$\Phi_o = \frac{hc}{2e} = 2.07 \times 10^{-7}\ G\ cm^2 \tag{I.3}$$

There are considerable complexities associated with the vortex state of a Type II superconductor and it turns out that the practicality (read technological application) depends largely on the vortex dynamics. If a current is applied to a Type II superconductor, in a magnetic field B greater than H_{c1}, the the vortices experience a Lorentz force

$$\vec{F} = \vec{J} \times \frac{\vec{B}}{c} \tag{I.4}$$

from the applied current and magnetic flux in the core. Eqn. (I.6) can be rewritten in terms of the single vortex flux quantum Φ_o as

$$\vec{f} = \vec{J} \times \frac{\vec{\Phi_o}}{c}. \tag{I.5}$$

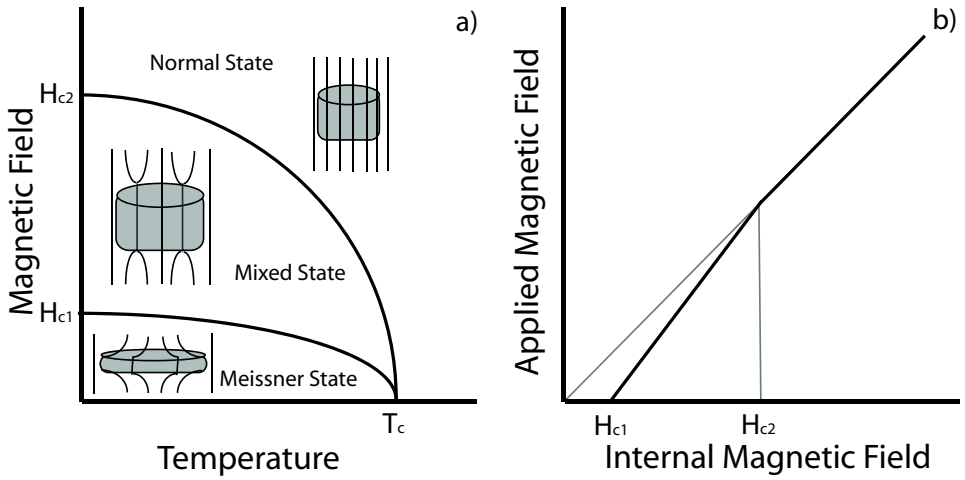

Figure I.4: Type II superconductivity. a) Cartoon diagram like the previous picture for Type I superconductors. However, Type II superconductors have an additional phase between H_{c1} and H_{c2}, the mixed phase, that allows partial penetration of the magnetic field via flux lines. b) Applied magnetic field versus internal field for a Type II. There is no penetration until H_{c1}, after which there is partial flux penetration as vortices. The sample then becomes normal at H_{c2}.

Eqn. (I.7) is now the Lorentz force on a single vortex. This force will cause the vortices to move transverse to the applied current, effectively creating a electric field:

$$\vec{E} = \vec{B} \times \frac{\vec{v}}{c} \tag{I.6}$$

where $\vec{v}$ is the vortex velocity. This electric field is parallel to the applied current and acts like a resistive voltage, thus leading to dissipation of power. This dissipation of power is the hurdle in the technological application of Type II superconductors, but if the vortices could be constrained from moving, we could recover dissipation free current flow up to the pair breaking current. Bardeen and Stephen [28] showed that in an idealized homogeneous sample, the vortex flux motion would be retarded only by a viscous-like drag. However, this is an idealized case and real materials exhibit some defects. These defects suppress superfluid density locally, which is why the vortices "like" defects, and the defects lead to pinning sites, effectively pinning the vortices and preventing their motion. The vortices will stay pinned so long as the pinning force is larger than the Lorentz force. Vortex motion or vortex flow will commence once the pinning force is overcome.

Additionally, Anderson and Kim put forth a theory where thermal fluctuations play an integral role in vortex motion [29, 30]. In their model, at finite temperatures, flux motion or flux creep is described by vortices hopping out of their pinning sites due to thermal activation leading to a finite resistance that was observed to have a linear temperature dependence [31].

This provides a basis for the next section on the vortex glass model, further describing vortex dynamics.

I.3.4 Vortex glass theory

Extending previous work on the mixed state of Type II superconductors, Matthew Fisher proposed a new phase, the "vortex glass" phase [32]. This work was later refined into the Fisher-Fisher-Huse (FFH) vortex glass model [19].

Their theory takes into account thermal fluctuations and quenched dis-

order (fixed inhomogeneities in a material), along with the anisotropy associated with the Type II high temperature superconductors. In this picture, the mixed state or vortex state becomes a very rich field that can be further subdivided into two more regimes: the vortex solid/glass and vortex liquid regimes. The dividing line between these two phases is described as either the melting field $H_m(T)$ or vortex glass transition temperature $T_g(H)$. This is shown in the cartoon-type diagram of Fig. I.5.

Qualitatively speaking, if a material is below the field $H_m(T)$ the vortex array is in the solid (glass) state consisting of a regular vortex lattice (or a disordered array of vortices, analogous to a glass and hence called a vortex glass) state. Above $H_m(T)$, the vortex array makes a transition to a mobile state, or liquid state. Here the vortices are able to move about, resulting in a noticeable loss of the true dissipationless superconducting state and the appearance of a small but finite resistance.

The major difference between the Anderson-Kim model and the FFH model lies in the fact that FFH assumes a correlation between vortex lines over the vortex glass correlation length ξ_G. The transition is assumed to be second order and scaling arguments are applied introducing the critical exponents ν and z (both defined below), which, due to the nature of scaling, should be universal and only vary depending on the nature of the phase transition.

The critical exponent ν is the static critical exponent, related to the vortex glass correlation length, and z is the dynamical critical exponent, related to the vortex glass relaxation time. With these exponents, we can now go back and write an expression for the form of the vortex glass correlation length, which diverges near the vortex glass temperature, T_g, as,

$$\xi_G \sim |T - T_g|^{-\nu} \tag{I.7}$$

The characteristic relaxation time τ_G scales with the correlation length as,

$$\tau_G \sim \xi_G^z. \tag{I.8}$$

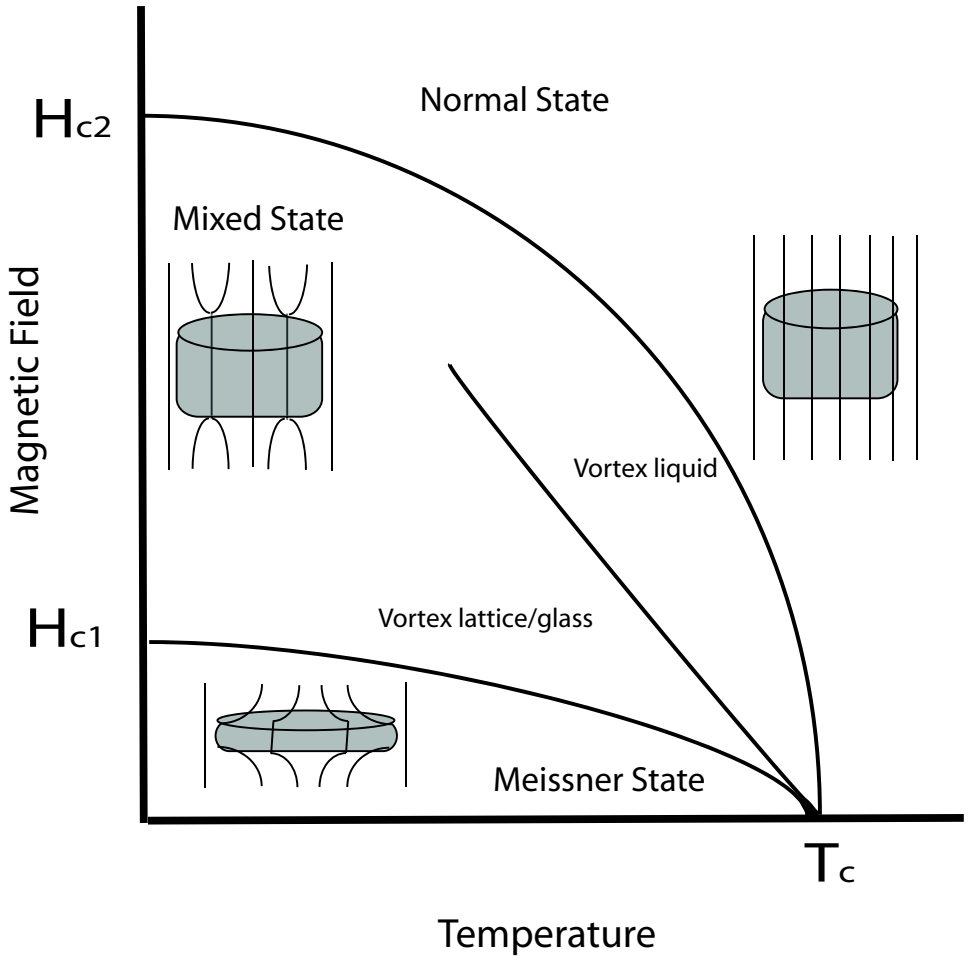

Figure I.5: Modified H-T phase diagram for Type II superconductivity.

The vortex glass melting temperature, T_g, and the critical exponents can be found through electrical transport measurements since the model predicts a linear temperature dependence of the resistivity above T_g such that

$$\rho \sim (T - T_g)^{\nu(z+2-d)}, \tag{I.9}$$

where d is the dimensionality of the system, which will be assumed to be equal to 3 from this point forward, hence reducing the critical exponent ν(z+2-d) to ν(z-1). This expression can be rearranged to give

$$\left(\frac{dln\rho}{dT}\right)^{-1} = \frac{T - T_g}{\nu(z-1)} \tag{I.10}$$

and so by plotting (d ln ρ/dT)$^{-1}$ vs. T, the data will yield a straight line over the temperature range of the vortex glass critical region. The line extrapolates to zero at the vortex glass melting temperature, T_g, and the slope of the line is the critical exponent, ν(z-1). An example of this is shown in Fig. I.6 for NCCO [33].

I.4 High Temperature Superconductivity in the Copper Oxides

There was a breakthrough in the field of superconductivity in 1986 with the discovery of high temperature superconductivity at $T_c > 30$ K by Bednorz and M*ü*ller [17] in the compound $La_{2-x}Ba_xCuO_4$. With this new discovery, there was a swarm of research with the hopes of using high temperature superconductivity in many technological applications. It was not long before several cuprate compounds were found with superconducting (SC) critical temperatures $T_c > 77$ K (77 K is the boiling point of liquid nitrogen), and quickly thereafter, compounds with T_c's as high as ~ 133 K at ambient pressure ($HgBa_2Ca_2Cu_3O_8$) [34]. Later, it was found that the SC critical temperature of $HgBa_2Ca_2Cu_3O_8$ could be pushed above 160 K under high pressure. Of more than 100 different cuprate materials discovered, the most significant ones are listed in Table I.1 [18].

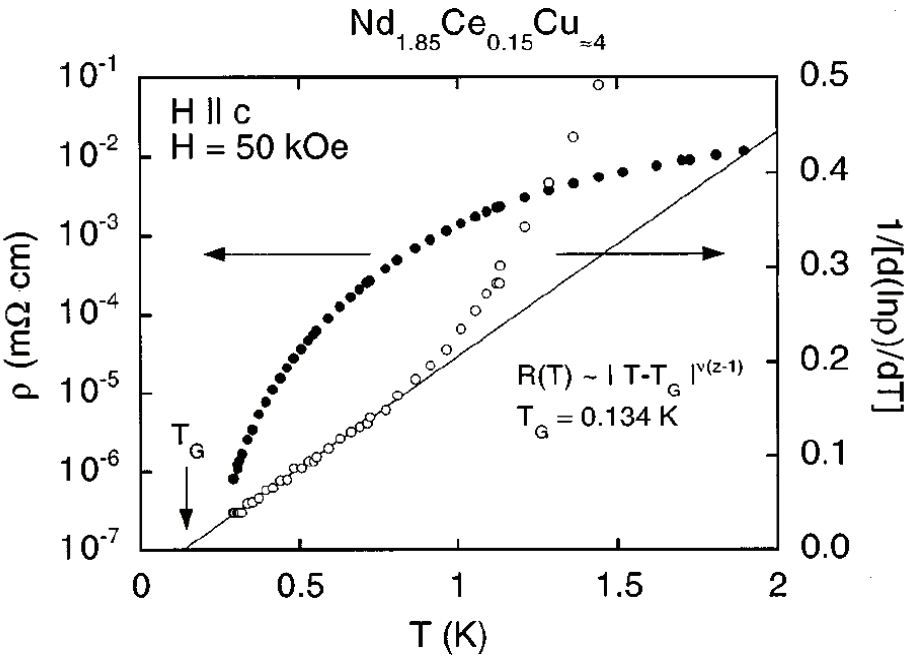

Figure I.6: Example of the FFH scaling model applied to a NCCO thin film sample [33]. Resistivity ρ (left hand axis) versus temperature T is shown along with $(\mathrm{d}\ \ln\ \rho/\mathrm{dT})^{-1}$ (right hand axis) versus T, which yields a straight line that extrapolates to the glass temperature T_G and the slope of the linear region gives the critical exponent ν(z-1).

Table I.1: Table of some of the more significant high T_c compounds [18].

Material	Maximum T_c (K)
$La_2 - xM_xCuO_4$; M = Ba, Sr, Ca, Na	~ 40
$Ln_2 - xM_xCuO_4 - y$; Ln = Pr, Nd, Sm, Eu; M = Ce, Th	~ 25
$YBa_2Cu_3O_{7-\delta}$	92
$LnBa_2Cu_3O_{7-\delta}$ Ce and Tb do not form phase Pr does form phase but is not SC'ing	~ 95
$RBa_2Cu_4O_8$	~ 80
$Bi_2Sr_2Ca_{n-1}Cu_nO_{2n+4}$ (n = 1, 2, 3, 4)	(n = 3) 110
$TlBa_2Ca_{n-1}Cu_nO_{2n+3}$ (n = 1, 2, 3, 4)	(n = 4) 122
$Tl_2Ba_2Ca_{n-1}Cu_nO_{2n+4}$ (n = 1, 2, 3, 4)	(n = 3) 122
$HgBa_2Ca_{n-1}Cu_nO_{2n+2}$ (n = 1, 2, 3, 4)	(n = 3) 133

The cuprates have layered perovskite-like crystal structures consisting of conducting CuO_2 planes and layers of the other elements of the compound. Fig. I.7 shows a comparison of the hole-doped $La_{2-x}M_xCuO_4$ (M = Ca, Ba, Sr) superconductors' T-structure and the electron-doped $Ln_{2-x}M_xCuO_{4-y}$ (Ln = La, Pr, Nd, Sm, Eu; M = Ce, Th) superconductors' T'-structure. The T-structure is orthorhombic with an octahedral arrangement of oxygen atoms around the copper atoms. However, the T'-structure is tetragonal with a square planar arrangement of oxygen atoms around the copper atoms. The most striking difference is the lack of apical oxygen atoms in the T'-structure.

Most of the cuprate compounds are hole-doped compounds whose name arises from the mobile charge carriers in the material. However, there are a handful of electron-doped compounds, which will be discussed further in the next subsection. The mobile charge carriers of these cuprates are believed to reside in the CuO_2 planes and the non-CuO_2 layers are believed to serve as charge reservoirs, controlling the doping of the CuO_2 layers. A number of the cuprate compounds, whether they be hole-doped or electron-doped, originate from an insulating antiferromagnetic parent compound that is made superconducting through the substitution of an element, or doping. An example of a hole-doped compound would consist of La_2CuO_4 in which Sr has been substituted for La, introducing mobile holes and producing superconductivity up to $\sim$ 40 K [35]. Likewise, for an electron-doped compound, one can also substitute Ce for Nd in Nd_2CuO_{4-y}, adding mobile electrons, giving rise to superconductivity up to $\sim$ 25 K [36]. Fig. I.8 is a generic diagram that shows a comparison between the temperature, T, versus concentration, x, phase diagrams of hole-doped and electron-doped cuprates emphasizing the general similarities and differences. It is interesting to note the symmetry between the hole-doped phase diagram and the electron-doped phase diagram. Both display an antiferromagnetic (AFM) region at low doping levels that is quenched with increased doping and eventually gives rise to a region of superconductivity. The superconducting dome is much more continuous and broad in the hole-doped

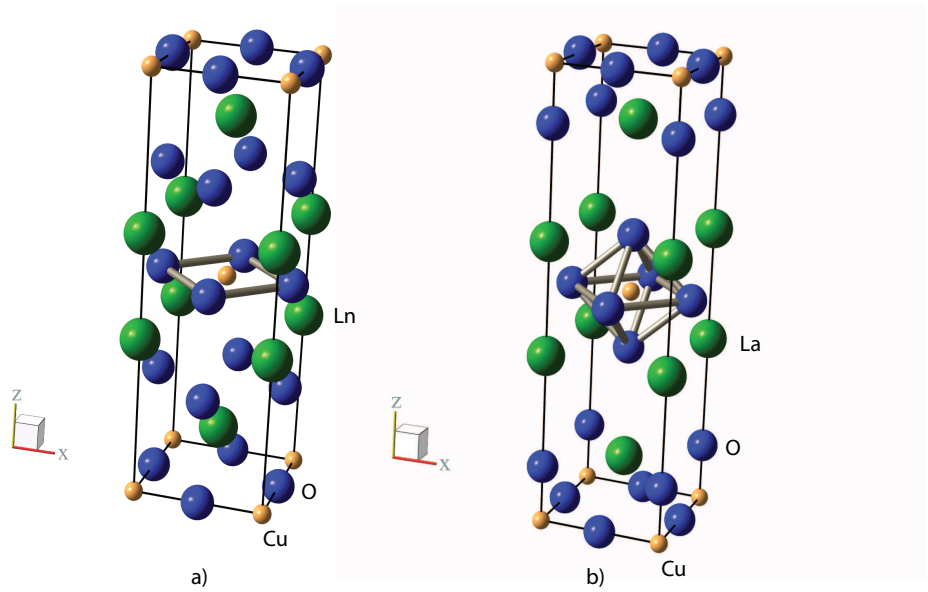

Figure I.7: Comparison of the T' and T structures. a) Generic T' structure with the Ln atoms as large green spheres, O as intermediate size blue spheres, and Cu atoms as small tan colored spheres. b) T structure shown with La atoms in green, O and Cu the same as in a).

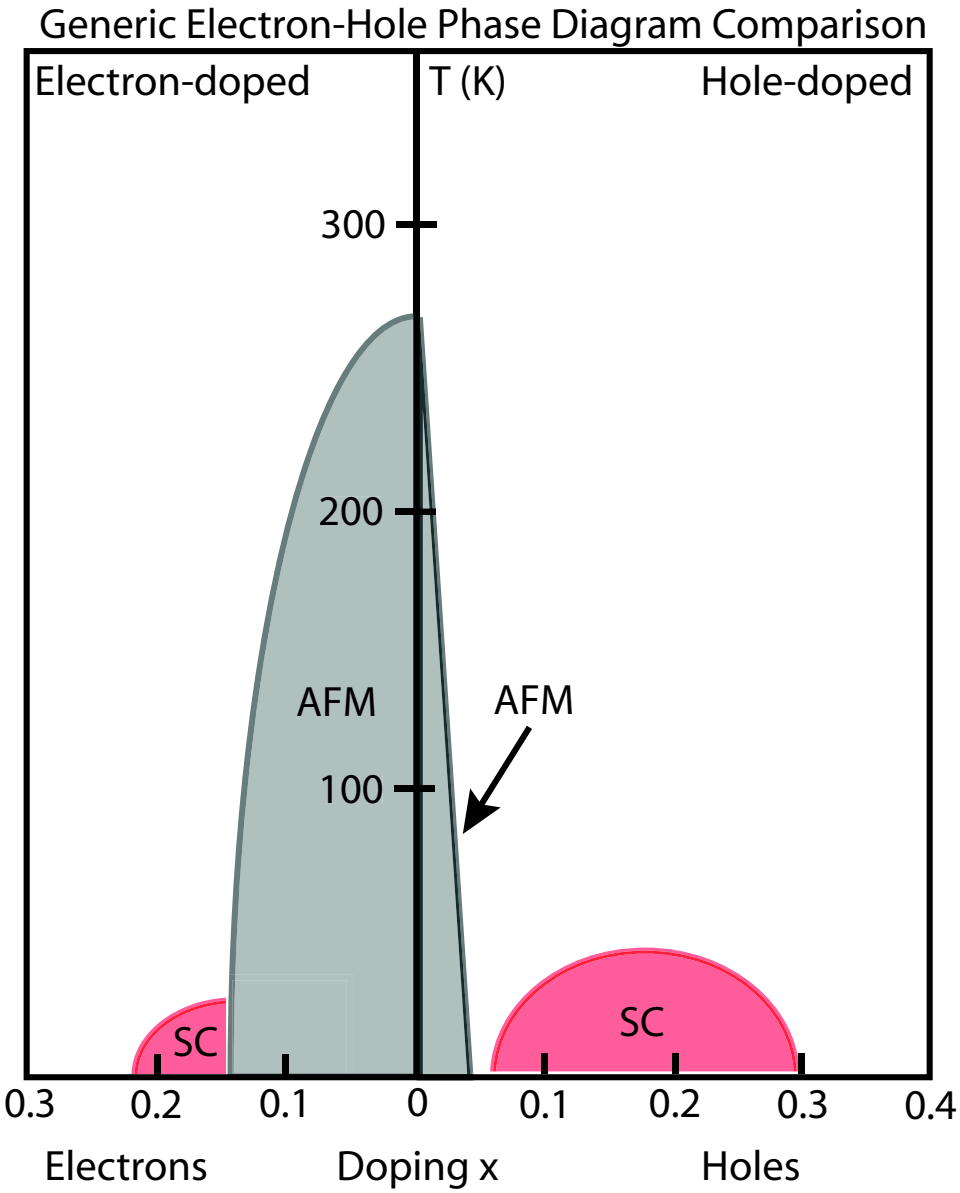

Figure I.8: Generic cartoon phase diagram for the electron and hole-doped superconductors emphasizing the similarities and differences [45].

compounds with no sharp features. However, beyond first glance, the phase diagram does have some dissimilarities. The obvious feature is the much larger region of antiferromagnetism on the electron-doped side, that leans against the superconducting region. It has been postulated that the asymmetry of the AFM region in the systems is due to a magnetic dilution effect versus magnetic frustration [37]. On the electron-doped side, the introduction of electrons tends to dilute the magnetic Cu as the Cu^{2+} turns to Cu^{1+} (which acts like a non-magnetic Zn ion) thus diluting the magnetic Cu in the compound [38]. On the hole-doped side, with the doped holes located near the oxygen atom, the introduction of the holes leads to a change in O^{2-} to magnetic O^{1-}. This unpaired spin could produce magnetic frustration from the magnetic O placed between two Cu ions providing an effective ferromagnetic interaction between the Cu moments and frustrates the antiferromagnetic ordering of the Cu [39]. It has been shown in $Rb_2(Mn_{1-x}Cr_x)Cl_4$ [40] and $Rb_2(Mn_{1-x}Zn_x)Cl_4$ [41], that magnetic dilution leads to a much slower suppression of AFM order than that of magnetic frustration, which destroys magnetic long range order. Finally, the superconducting region is rather asymmetric in the electron-doped materials with an abrupt increase in T_c from underdoping to optimally doped (defined as the concentration with maximum T_c) and then a more gradual decrease in T_c upon further doping (overdoping).

I.4.1 Electron-Doped Cuprate Superconductors

The electron-doped superconductors were discovered in 1989 by Tokura, Takagi, and Uchida [36]. The new and exciting feature of these compounds was that, unlike previous high T_c materials that had been doped with electron vacancies, or holes, these compounds were made superconducting by doping electrons. The trivalent (3^+) ions such as Nd, Pr, and Sm were replaced by tetravalent (4^+) Ce, presumably introducing mobile electrons to the system.

Soon after the discovery of these electron-doped compounds, an answer to the question of whether superconductivity could be attained with the substitution

of another tetravalent atom emerged. Several other electron-doped superconductors were discovered having the same general chemical formula but with Ln = Pr, Nd, and Sm and M = Th in the formula $Ln_{2-x}M_xCuO_{4-y}$ [42–44]. Grouped in with the discovery of these compounds was the addition of superconducting $Eu_{2-x}Ce_xCuO_{4-y}$ to the growing list of electron-doped compounds.

Table I.2 lists the Ln_2CuO_4 based electron-doped superconductors, taken from reference [45], and it is easy to see that there are not many electron-doped superconductors in comparison to the hole-doped compounds.

Let us turn our attention to the systems with the chemical formula $Ln_{2-x}M_xCuO_{4-y}$, in particular those with Ln = Pr, Nd, or Sm and M = Ce. These systems have been the most widely studied electron-doped superconductors thus far. The parent compounds (Ln_2CuO_4) are antiferromagnetic insulators with one electron per unit cell; however, with increased doping (in this case Ce) the carrier concentration is increased and the compound becomes more metallic and superconductivity is observed within a narrow region of concentration. The first superconducting phase diagrams for NCCO and PCCO [46] polycrystalline samples along with more recent work on PCCO [47] thin films, which we will see are nearly identical to SCCO, are shown in Fig. I.9. The antiferromagnetism associated with the Cu atoms is suppressed with increased doping. Luke et al. [37] found the Néel (T_N) temperature of the parent compounds Ln_2CuO_4 (Ln = Pr, Nd, Sm) to be $\sim$ 250 K. Additionally, the authors mapped the AFM region as a function of cerium doping by muon spin relaxation measurements. They showed the boundaries of the AFM region persist up to the superconducting region, which was added to the superconducting phase diagram, Fig. I.10.

In addition to the antiferromagnetism associated with the Cu atoms, the rare-earth atoms of Nd and Sm display antiferromagnetic order (AFM) at low temperatures that coexists with superconductivity [48–50]. Nd^{3+} orders at $T_N \sim 2$ K and Sm^{3+} orders at $T_N \sim 6$ K. However, the Sm spin configuration is different from that of Nd, and also any other high temperature superconductor.

Table I.2: Table of the electron-doped superconductors from [45].

$Ln_{2-x}M_xCuO_{4-y}$; x = 0.15; y = 0.02			
Ln	M		T_c onset (K)
Pr	Ce		22
Nd	Ce		24
Sm	Ce		19
Eu	Ce		13
Pr	Th		23
Nd	Th		19
Sm	Th		7
$Ln_2CuO_{4-x-y}X_x$			
Ln	X		T_c onset (K)
Nd	F		27
$Ln_{2-x}M_xCu_{1-z}M'_zO_{4-y}$; x + z = 0.15			
Ln	M	M'	T_c onset (K)
Nd	Ce	Ga	25
Nd	Ce	In	25

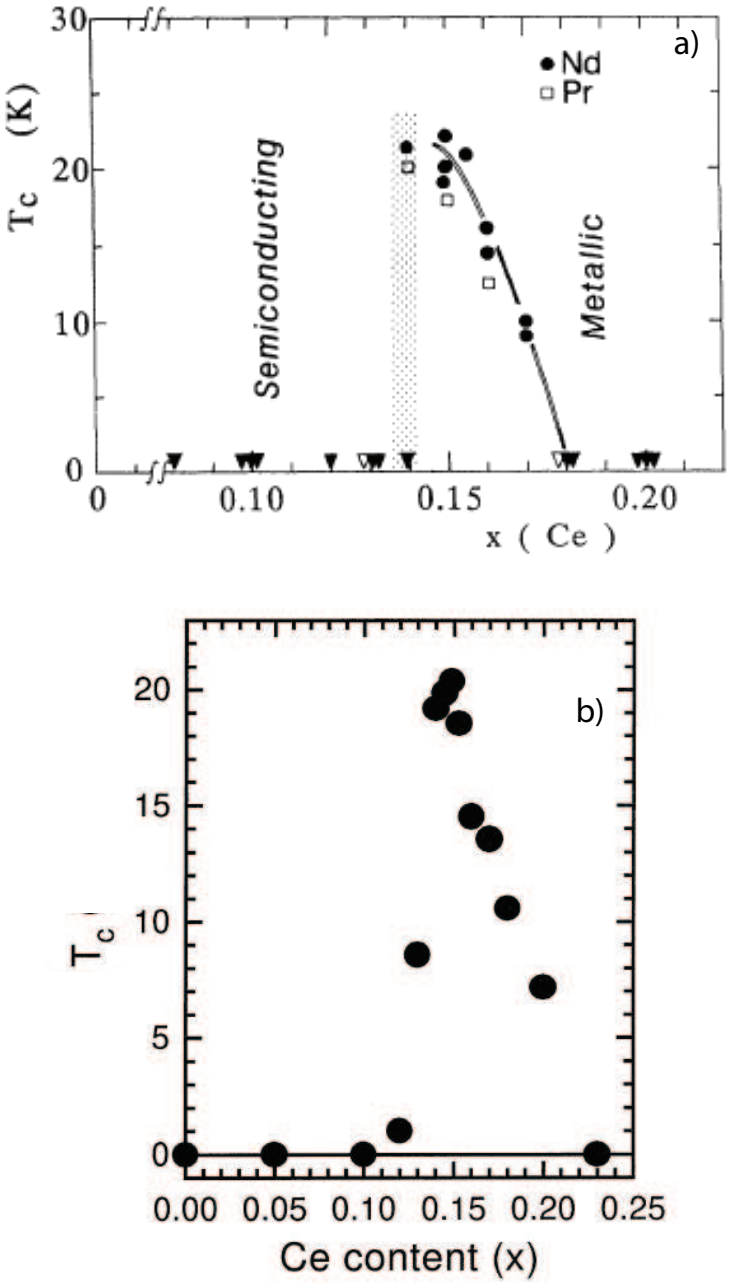

Figure I.9: a) Superconducting phase diagram for NCCO and PCCO polycrystalline samples as explored originally by Takagi et al. [46]. b) Recent work on PCCO thin films showing the superconducting region extends further than originally thought on the overdoped side [47].

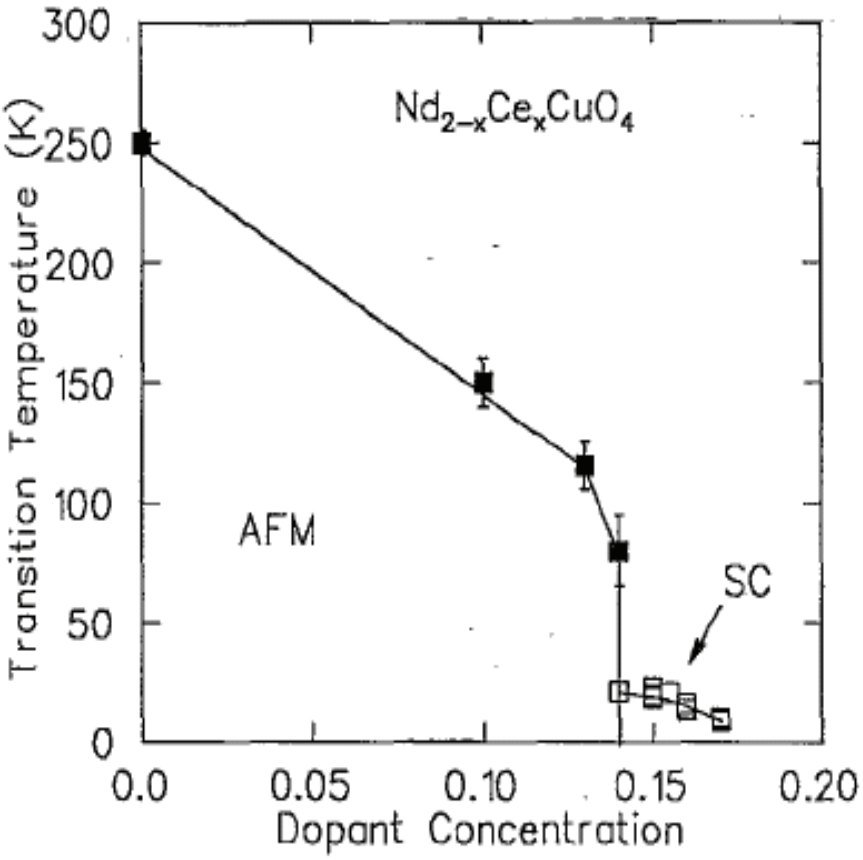

Figure I.10: Full phase diagram for NCCO as a function of cerium content displaying both the Cu AFM region and superconducting region, taken from ref. [37].

The Sm spins align themselves ferromagnetically within the a-b planes but align antiparallel in alternating layers. Fig. I.11 shows the magnetic structure of SCCO. The rare earth compounds $RERh_4B_4$ (RE = Gd, Tb, Dy, Ho, Sm, Nd, Er, Tm and Lu) [51–53] were studied in terms of the interaction between long range magnetic order and superconductivity. $SmRh_4B_4$, in particular, displayed the coexistence of superconductivity and antiferromagnetism and was shown to have an enhancement in the upper critical field H_{c2} associated with the onset of AFM [53–56]. Therefore, one might also expect some effect from the AFM order on the superconducting properties of SCCO. An example was the report of an enhancement of the vortex glass melting line [57], which will be discussed further in Chapter 3.

There has been considerable work performed on $Nd_{2-x}Ce_xCuO_{4-y}$ and more recently on $Pr_{2-x}Ce_xCuO_{4-y}$. NCCO has been studied in multiple forms including polycrystalline samples, single crystals [58–60], and thin films [33,61,62]. To date, there has not been nearly as much literature on $Sm_{2-x}Ce_xCuO_{4-y}$ and, in particular, no literature on thin films before this project was undertaken.

This dissertation contains the first report of the growth conditions for thin films of SCCO by PLD as well as the first systematic study of the phase diagram of SCCO in thin films, the magnetoresistance of the thin films across the doping range, and the vortex glass behavior of the system. Additionally, thermopower measurements were performed on selected dopings.

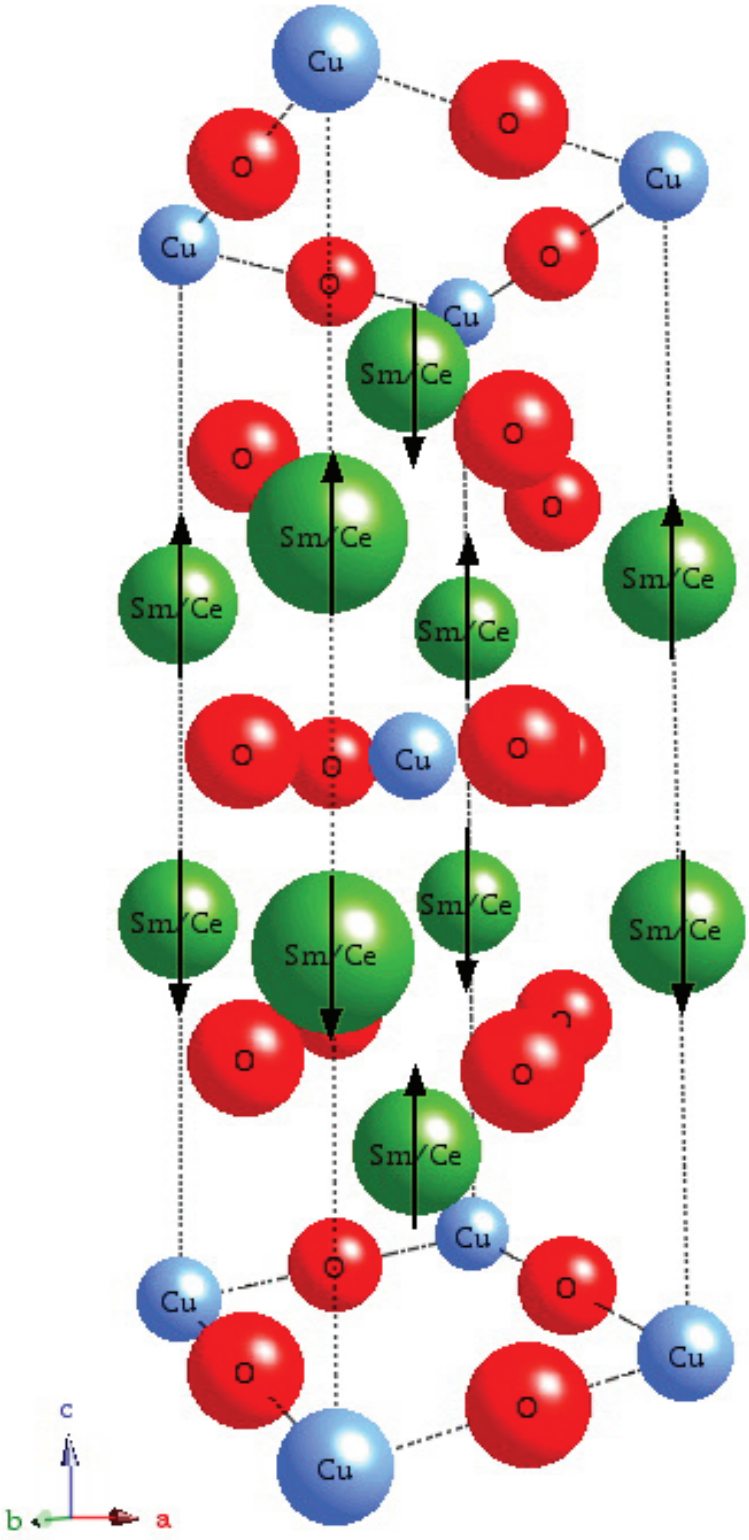

Figure I.11: Magnetic structure of SCCO showing Sm^{3+} spin configuration.

II

Materials and Methods

II.1 The Laser Ablation System

The samples presented in this thesis were prepared in the pulsed laser deposition, PLD, laboratory, part of which was designed and built over the course of this research specifically to synthesize films of high temperature cuprate superconductors. The film growth system consists of several basic parts: an excimer laser, optics for focusing the laser beam, vacuum deposition chamber, gas handling system, target rotator, and substrate heater block with temperature controller. These components will be discussed in further detail below. Fig. II.1 shows a schematic of the PLD setup and Fig. II.2 is a photograph of the facility.

The excimer laser is a Lambda Physik LPX305i UV laser with a wavelength of 248 nm utilizing a KrF gas mixture. The laser's maximum energy output is 1.8 J per pulse, the pulse duration is 25 ns, and the repetition rate can be varied from 1 to 50 Hz. The laser is operated via a handheld keypad controller in one of two modes: constant energy mode or constant voltage mode. All growths contained in this dissertation were done using the constant energy mode, in which the controller automatically adjusts the discharge voltage to maintain a constant energy over the entire growth period by monitoring the laser's internal energy meter. The internal energy meter was periodically checked and calibrated using a Scientech Vector S310 external power meter. These measurements ensure that the

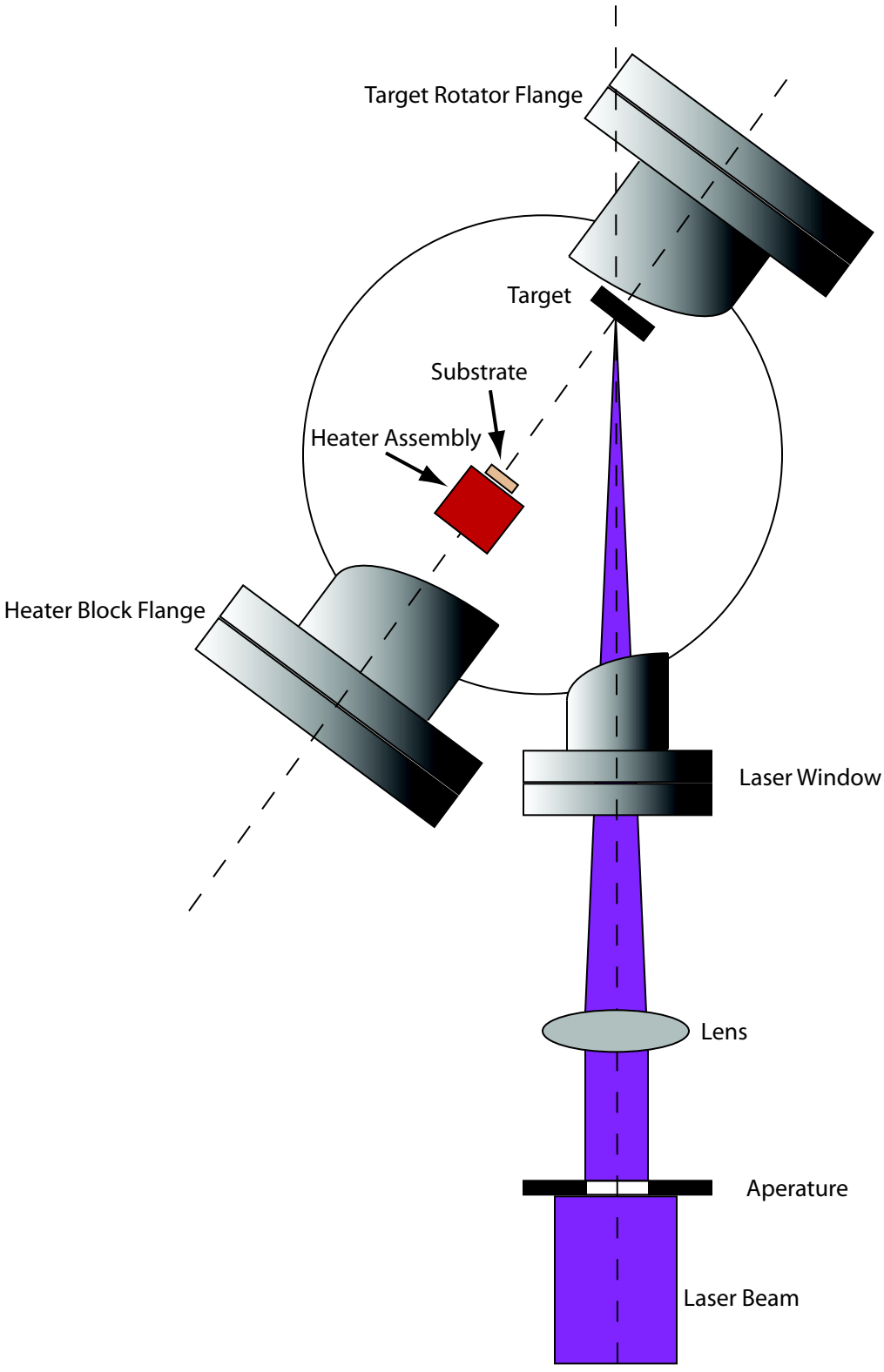

Figure II.1: Schematic of the laser ablation chamber setup.

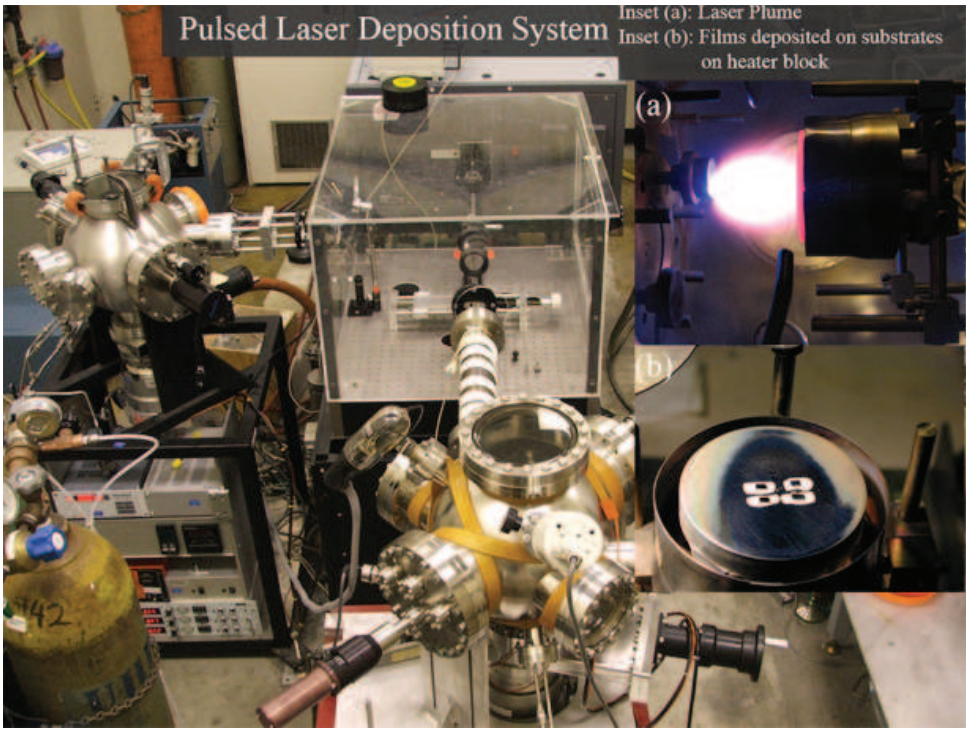

Figure II.2: Photograph of the pulsed laser deposition laboratory used in this study. a) Photograph of the ejected plume from the target material. b) Photograph of the substrate heater block with four films mounted at its surface.

energy density (E_d) of the laser beam at the target surface is constant over the gas lifetime. The energy density E_d is given by the following equation:

$$E_d = \frac{E}{A}. \tag{II.1}$$

where E_d is the energy density (J/cm^2), E is the energy of the incident laser beam (J), and A is the size of the laser spot (cm^2).

The laser beam exits the LPX305i with a rectangular shape and dimensions of 1 - 1.5 cm x 3 cm. After exiting the laser cavity, the beam passes through a 1 x 3 cm aperture to remove beam fringes on the beam. In the photograph of the PLD laboratory (Fig. 2.2), one can see two vacuum deposition chambers as well as the optics on the isolation table. The chamber at the bottom of the photo, and directly in front of the laser, is used for metallic thin films since a direct path minimizes optics needed and therefore minimizes energy losses. The cuprate oxide materials require a much smaller energy density and can therefore tolerate more losses through the optics. For this reason, the oxide growth chamber is located on the left hand side of the photograph and the beam must be reflected 90 degrees to enter the chamber. Regressing to the point after the laser beam has passed through the 1 x 3 cm aperture, the beam is reflected off the mirror and passes through a second aperture of dimensions 1 x 2 cm. Following this aperture the beam is focused with a lens before transmission through the deposition chamber window. The lens focuses the beam to a spot size of 1 x 3 mm on the target surface. Energy losses due to all optics except chamber window are roughly 60 percent.

The PLD laboratory has two stainless steel vacuum chambers custom designed and manufactured by Kurt J. Lesker in order to provide an isolated growth environment. The two chambers are identical in so far as they both have a spherical shape 12 inches in diameter with various ports for supplementary equipment. Beyond that, they have large differences owing to the fact that one is designed for high vacuum oxide material growth, and the other, ultra high vacuum metallic film growth. All depositions described in this thesis were performed in the ox-

ide chamber, so further description applies only to this chamber. There are four quartz windows on the chamber, three for viewing the interior and one for the laser beam to enter through. The laser window is made of a UV grade silica that allows minimal beam absorption. Attenuation of the beam by the window is roughly 30 percent.

The growth chamber is evacuated through the bottom most port utilizing a vertically mounted Leybold-Heraeus turbo molecular pump backed by a General Electric roughing pump that is used to evacuate the system. A gate valve separates the chamber from the turbo pump. Before growths, the system is rough pumped to approximately 50 mTorr, after which the turbo pump is engaged. Pump down time is approximately one and one half hours from atmosphere to $1x10^{-6}$ Torr.

Chamber pressure is monitored using three gauges and a BOC Edwards active gauge controller (AGC). The three gauges are as follows: BOC Edwards active strain gauge (ASG) (760 Torr (atmosphere) $\leq$ P $\leq$ 10 Torr), BOC Edwards capacitance manometer (10 Torr $\leq$ P $\leq$ 1 mTorr), and BOC Edwards ion gauge (AIGX) (P $< 10^{-3}$) Torr. All depositions in this work were done in the mTorr range and the capacitance manometer was used to monitor pressure during growths. The advantages of using this gauge over others is that it is gas independent, making it possible to switch gases without having to make any gas corrections or recalibrate the gauge, and it is also possible to use reactive gases during ablation.

During thin film growth, a gas handling system is utilized to introduce a background gas into the chamber. Any gas can be connected to the system and the gas passes through a needle valve, an MKS mass flow controller, and, finally, a three way switching valve that directs the flow either directly into or away from the plume. The background pressure is set by choosing a flow rate and adjusting the gate valve. An MKS Instruments mass flow controller with flow meter is used to monitor the flow rate and maintain a constant flow during the ablation period. The gas handling system plays a critical role in the synthesis of the films reported here because sample consistency heavily depends on the repeatability of the gas

flow during growth.

In order to uniformly ablate material from a target, the target is mounted on a target rotator and rotated during ablation. This creates a circular track around the target to avoid depleting material from a single point source on the target as well as superheating of the target, which can lead to large particulates on the film surface. Two Neocera target rotators are available for use: a single target rotator and a 6 target carousel. Fig. II.3 shows a picture and schematic of the 6 target carousel that is mounted on the oxide chamber allowing for more versatility in the growth of multilayers, buffer layers, or thick films. The target rotators can be switched easily from one chamber to the other. Once the targets are mounted on a target holder, they are attached to the carousel using a set screw and rotated at a constant 17 rpm during ablation.

During growth, material is ablated onto substrates that are attached to a Neocera substrate heater block. The heater block is controlled by a Eurotherm programmable temperature controller and is shown schematically in Fig. II.4. The circular heater block is 2 inches in diameter and can be heated to 950 °C with temperature stability better than ± 1 °C. A K-type thermocouple is used to monitor the temperature. There is a shutter on a rotatable feedthrough allowing the shutter to be closed during a one minute pre-ablation target cleaning and then re-opened for the deposition.

II.2 Thin Film Growth

The $Sm_{2-x}Ce_xCuO_{4-y}$ target was prepared according to the following prescription. Polycrystalline targets were formed by a solid state reaction technique with starting materials of 99.99% pure oxides of Sm_2O_3, the dopant CeO_2, and CuO. To insure the proper stoichiometry of the target, the procedure for calculation of the required starting materials and weighing of the materials was formulated according to the final desired weight of the target and the weight of the dopant and

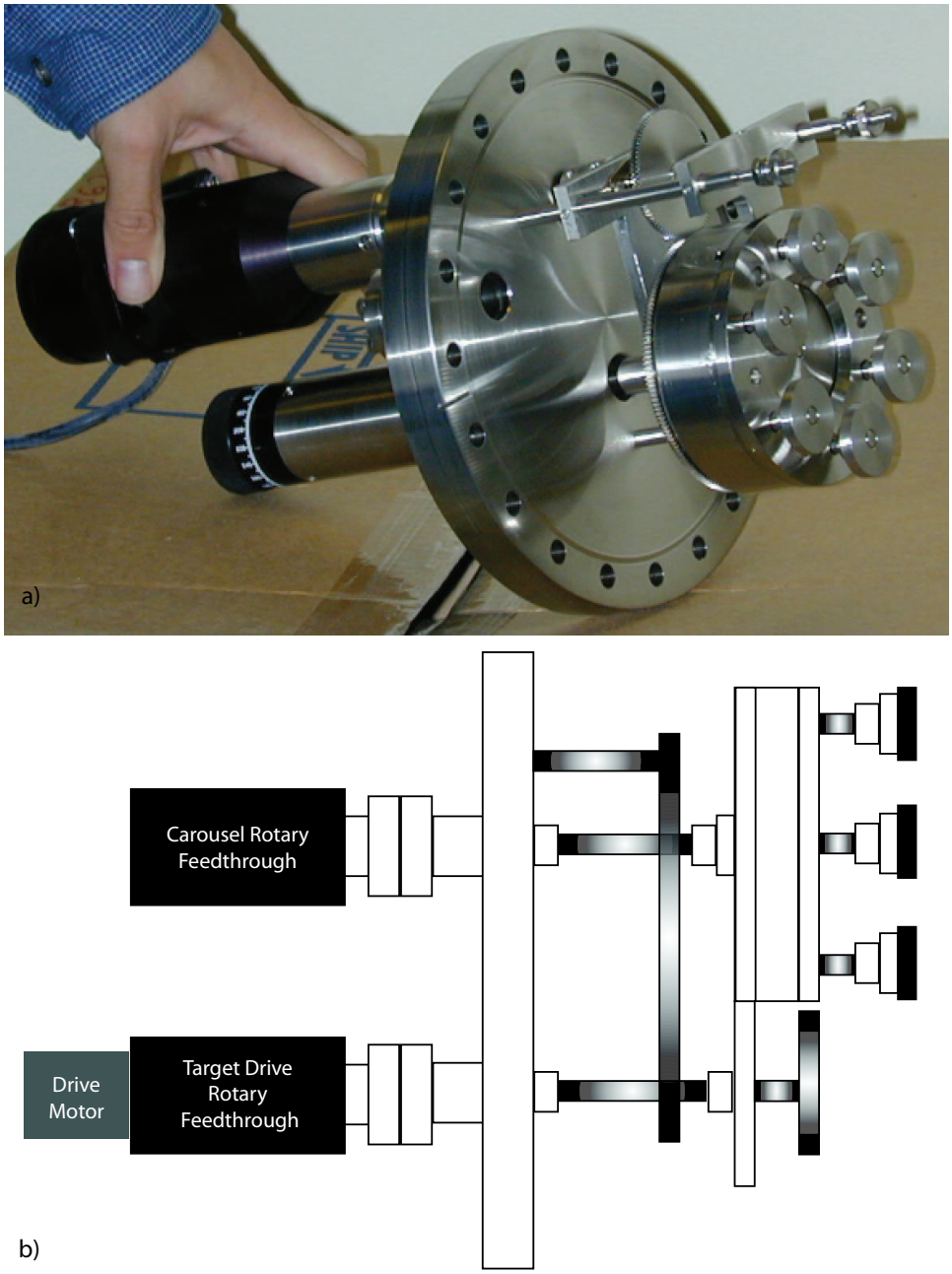

Figure II.3: Target carousel used for pulsed laser deposition. a) Photograph of actual carousel used in this study. b) Schematic diagram of target carousel.

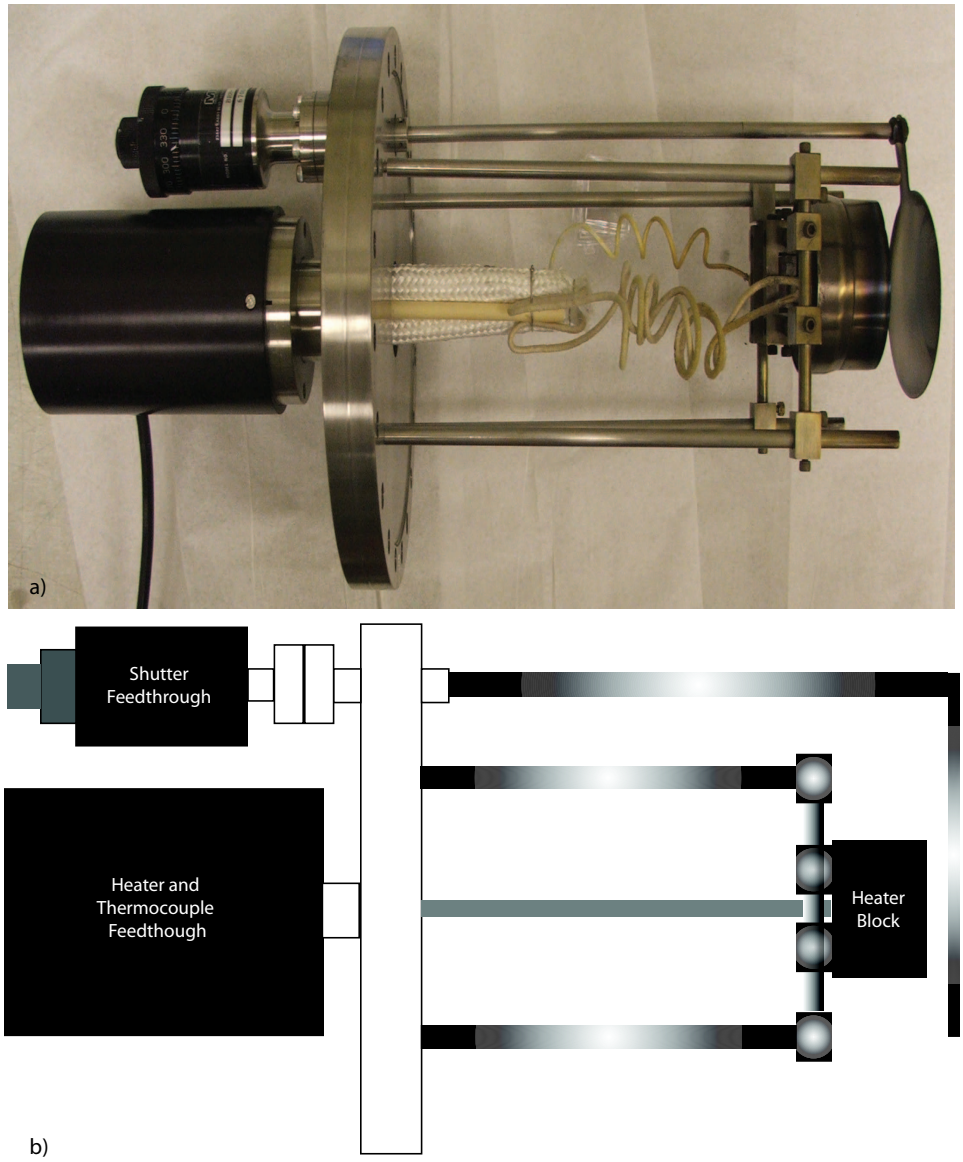

Figure II.4: Substrate heater block used for pulsed laser deposition. a) Photograph of the heater block used in this study. b) Schematic diagram of the heater block.

is detailed in Appendix A. Because Sm_2O_3 and CeO_2 absorb water readily [63], the powders were dried in air inside alumina crucibles at 900 °C for $\geq$ 12 hours. Once the powders were dry, a portable glove bag filled with ultra-high purity (UHP) Ar was utilized to weigh and mix the powders in a dry and inert atmosphere. The materials were weighed on an analytical balance with 0.1 mg resolution, and were weighed to within 0.1 mg of the calculated weight. Once all the materials were measured, they were combined in a glass jar inside the glove bag and hand tumbled until mixed. The mixture was then transferred to an alumina crucible and fired in air for $\geq$ 18 hours at 900 °C. The sample was then removed from the furnace and was clearly not homogeneous with large lanthanide oxide particles visible to the eye. The material was then ground by hand, using an agate mortar and pestle, until it was a dark grey homogeneous powder, plus an additional 5 minutes of grinding. The powder was placed back in the furnace and fired in air at 1000 °C for $\geq$ 24 hours. The resulting dark grey compacted material was then ground in a Retsch/Brinkmann centrifugal ball mill using a 50 mL agate jar, two 2 cm diameter agate balls, and three 1 cm diameter agate balls. The material was ground at $\sim$ 75 rpm for 90 minutes with the mill reversing direction every 30 seconds. This resulted in a very fine powder that tended to stick to the jar and balls. The powder was scraped off with some loss of material but it was assumed at this point that the powder was homogeneous so that any loss did not result in an alteration of the final stoichiometry. The powder was placed in a 0.75 inch diameter stainless steel die and pressed to 12,000 lbs to make a cylindrical pellet with a height of approximately 0.25 inches. The pellet was placed back in the furnace for the final firing in air at 1100 °C for $\geq$ 3 days. After the firing period, the furnace was cooled to 900 °C and the target was removed to cool in air.

A small disk of the target was cut using a South Bay Low Speed Diamond Wheel Saw. This disk was again cut into two pieces for sample characterization by x-ray diffraction and magnetic susceptibility. A small reduction in oxygen is needed in order to make the samples superconducting. Both pieces were annealed

in a tube furnace for 18 hours at 950 °C in flowing He. The superconducting critical temperature, T_c, was measured using a Quantum Design MPMS magnetometer. The crystallographic information was obtained by powder diffraction using a Rigaku DMAXB x-ray diffractometer.

To prepare the SCCO pellet for use as a PLD target, the pellet was attached to a cylindrical target mount using DuPont silver conductor paste. The target and holder were then baked at 200 °C for $\sim$ 20 minutes to cure the epoxy. The target was sanded to a smooth surface before each growth and the target was pre-ablated for 1 minute prior to each growth to remove any surface debris.

Commercially grown substrate materials were purchased with one side polished and specific crystallographic orientations. The $Sm_{2-x}Ce_xCuO_{4-y}$ films were grown on yttria-stabilized zirconia (YSZ) with a (100) orientation. The substrates were mounted on the heater block with SPI flash dry silver paint. The heater block was then placed under a heat lamp for several minutes to dry the paint. The heater block assembly was cleaned between each growth.

Every material grown via pulsed laser deposition requires a unique optimization. The optimized conditions for growth of the $Sm_{2-x}Ce_xCuO_{4-y}$ were determined experimentally from numerous trial growths while systematically varying the parameters including: incident laser energy density, substrate temperature, chamber pressure, and annealing conditions. A brief description of the optimization will be given here followed by the optimized recipe for growth. A more thorough description of the thin film characterization along with the data can be found in the next chapter.

With such a vast parameter space to work with, initial growth conditions for the chamber temperature and chamber pressure were taken from literature on the similar compounds $Nd_{2-x}Ce_xCuO_{4-y}$ [64–66] and $Pr_{2-x}Ce_xCuO_{4-y}$, described in detail in Chapter 1, and then adjusted during subsequent trial runs. These compounds form well at T $\approx 800^o$ C and under chamber pressures of $\approx$ 200 mTorr of flowing N_2O. The deposition time was 10 minutes in duration for all samples grown.

After each growth the chamber was evacuated and the heater switched off. Samples were cooled in the chamber to $\approx 100^o$ C, the chamber was vented, and the samples removed. The energy density of the laser was scanned from 5 J/cm^2 - 1.5 J/cm^2. The results of these growths were used to determine the optimal energy density. The films were grown and screened for superconductivity in a Quantum Design Magnetic Property Measurements System (MPMS). No superconductivity was found in the films grown with high energy density ($E_d > 3.5$ J/cm^2). Moreover, the films grown with $E_d > 3.5$ J/cm^2 were observed visually to have little deposited material on the substrates. X-ray diffraction showed the films to be highly oriented along the (001) direction with diffraction peaks from an impurity phase at $\sim 33^o$ and $\sim 69^o$. An example of an x-ray diffraction pattern is shown in Fig. II.5. The impurity phase was found to decrease with decreasing energy density as shown in Fig. II.6. Based on these data, the energy density was set to $\sim$ 1.5 J/cm^2 for subsequent runs. The energy density was verified before and after each growth using a Scientech Vector S310 external power meter.

Keeping the chamber pressure at 200mTorr and after having experimentally chosen the energy density, an in-situ anneal, again based on reports found in the literature, was performed on the films. Once again, original annealing conditions were taken from the literature. The films were grown at 800 ^{o}C in N_2O at an energy density of 1.5 J/cm^2. After growth the chamber was evacuated and the samples were cooled to 600 ^{o}C at a rate of 20 ^{o}C/min. The samples dwelled at 600 ^{o}C for a duration of X minutes ($0 \geq X \geq 10$), cooled again to 400 ^{o}C at a rate of 25 ^{o}C/min, dwelled for 8 minutes, and then the heater was shut off and the samples cooled to $\sim$ 100 ^{o}C before venting the chamber and removing the films. A diagram of the annealing schedule is shown in Fig. II.7. The annealing time at 600 ^{o}C was varied from 0 minutes to 10 minutes. A plot of the superconducting critical temperature, T_c, versus anneal time and impurity phase versus anneal time are shown in Figs. II.8 and II.9, respectively. The T_c is shown to increase with dwell time to a maximum at about 4 minutes, while the impurity phase is seen to

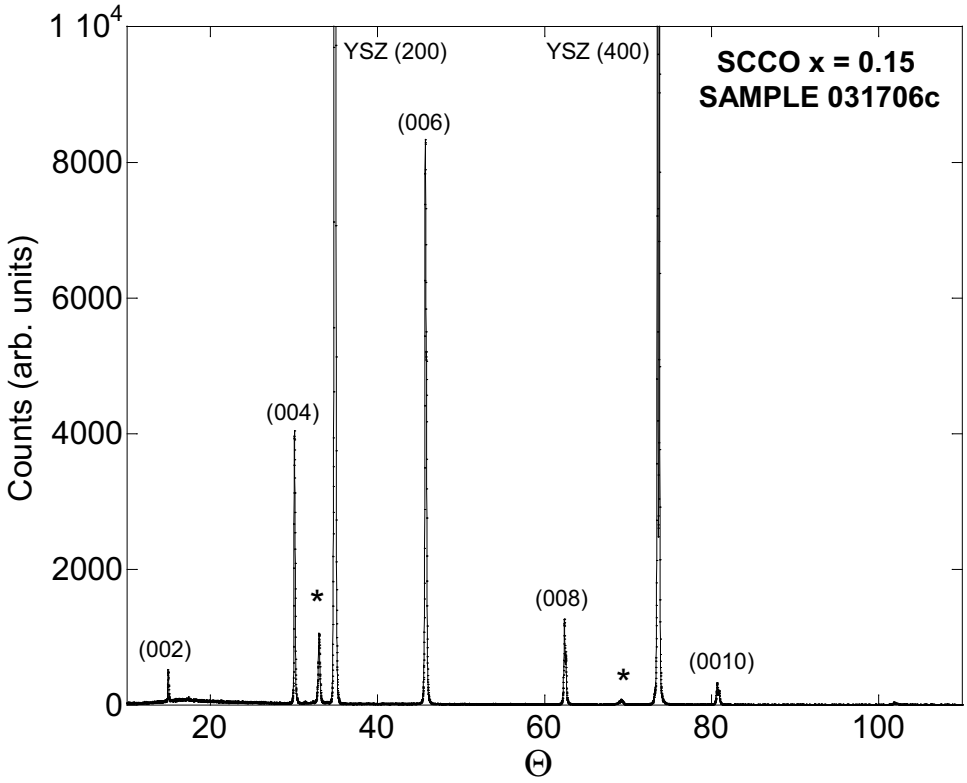

Figure II.5: X-ray diffraction pattern for a $Sm_{1.85}Ce_{0.15}CuO_{4-y}$ film with labelled peaks displaying the highly c-axis oriented nature of the films. Two impurity peaks (labelled with a *) can be seen at $\sim 33\ ^o$ and $\sim 69^o$ as well as the two substrate peaks at $\sim 35\ ^o$ and $\sim 73\ ^o$.

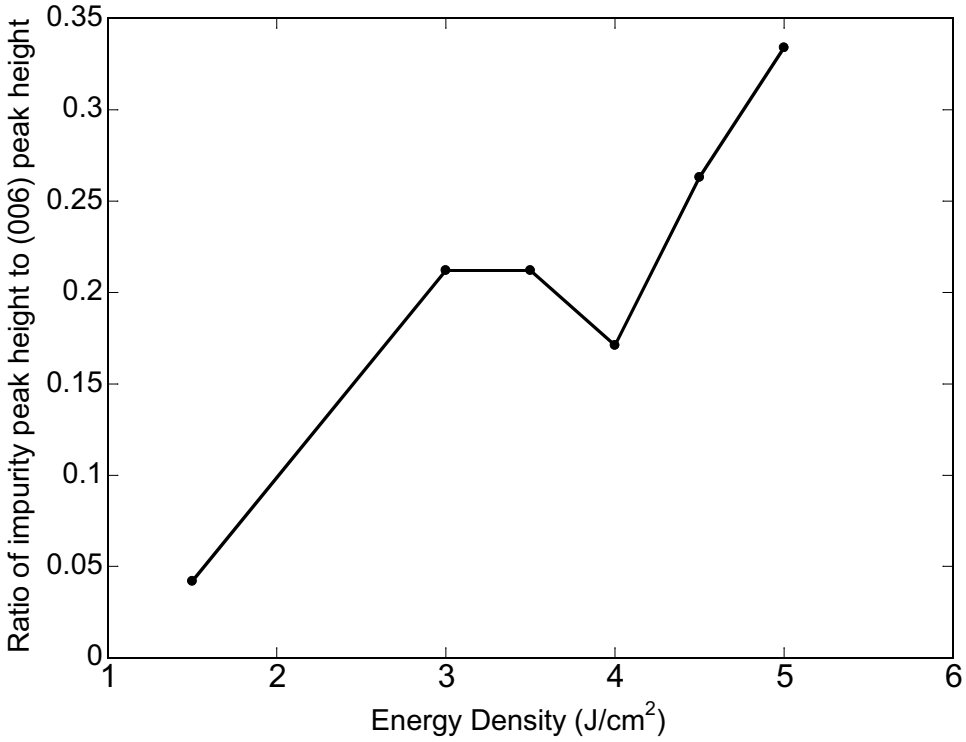

Figure II.6: Normalized impurity peak height (impurity peak height divided by (006) peak height) versus the energy density used for the thin film deposition showing decrease in impurity peak with decreased energy density.

be fairly constant versus dwell time. Hence, an anneal time of 4 minutes at 600 ^{o}C was used for subsequent growths.

The final recipe for growth of the SCCO thin films was determined from the data gathered and a graphical representation is shown in Fig. II.10. The film was grown at 800 ^{o}C in 200 mTorr of flowing N_2O. After growth, the chamber was evacuated and the film was cool to 600 ^{o}C at a rate of 20 ^{o}C/min, where it was then held for 4 minutes to anneal. Following the anneal, the film was cooled again to 400 ^{o}C at a rate of 25 ^{o}C/min, dwelled for 8 minutes, and then the heater was shut off and the film cooled to $\sim$ 100 ^{o}C before the chamber was vented and film was removed.

After growth the films were characterized by x-ray diffraction, magnetization, and electrical transport measurements. There was no further preparation required for x-ray or magnetization measurements. Additional preparation was necessary for electrical transport measurements. The films were prepared in one of two ways. All the ρ(H, T, Θ) data was taken on films in which gold pads were sputtered on the films using an Anatech Hummer 6.2 sputtering machine. The films were annealed for 10 minutes in air at 500 ^{o}C to allow the gold to diffuse into the films. Gold leads were then attached using a two part silver epoxy and cured for 3 minutes at 200 ^{o}C. Hall effect experiments were to be performed on films which had been patterned into Hall bars using optical photolithography. A mask was designed specifically for these films and experiments. The patterns were drawn using AutoCAD and the mask was produced by Advance Reproductions Corporation. S1818 photoresist was spun onto the films for 1 minute at 5000 rpm and then baked for 1 minute at 115 ^{o}C on a hot plate. The mask was aligned on the film, the masked film was exposed, and the film was then placed in a developer solution of 1:2, MP developer:water, for about 1 minute. The film was baked again for 1 minute at 115 ^{o}C and chemical etching was done using HCl. Once the films were patterned, gold pads and leads were attached as described above. An example of a patterned films is shown in Fig. II.11.

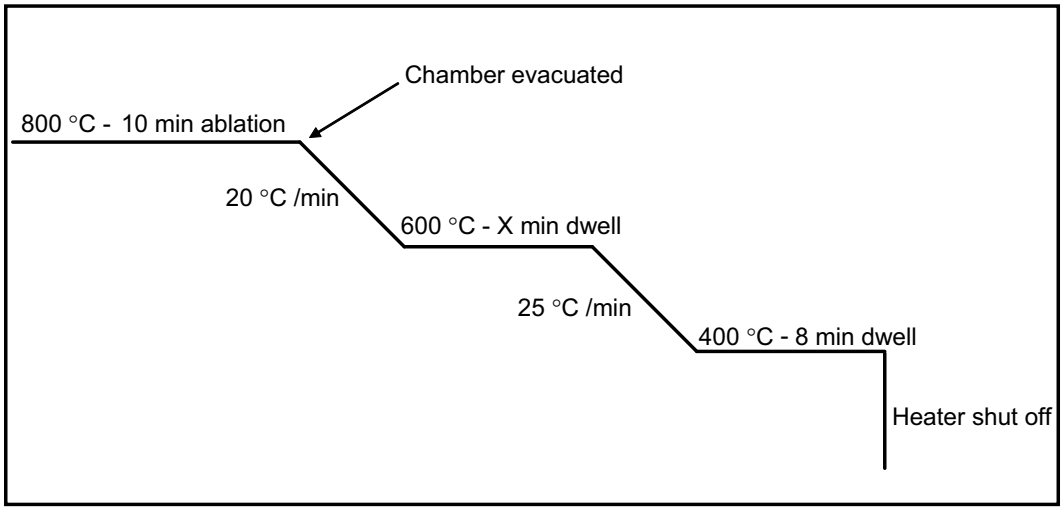

Figure II.7: Generic in-situ annealing schedule, where the dwell time at 600^o C was varied.

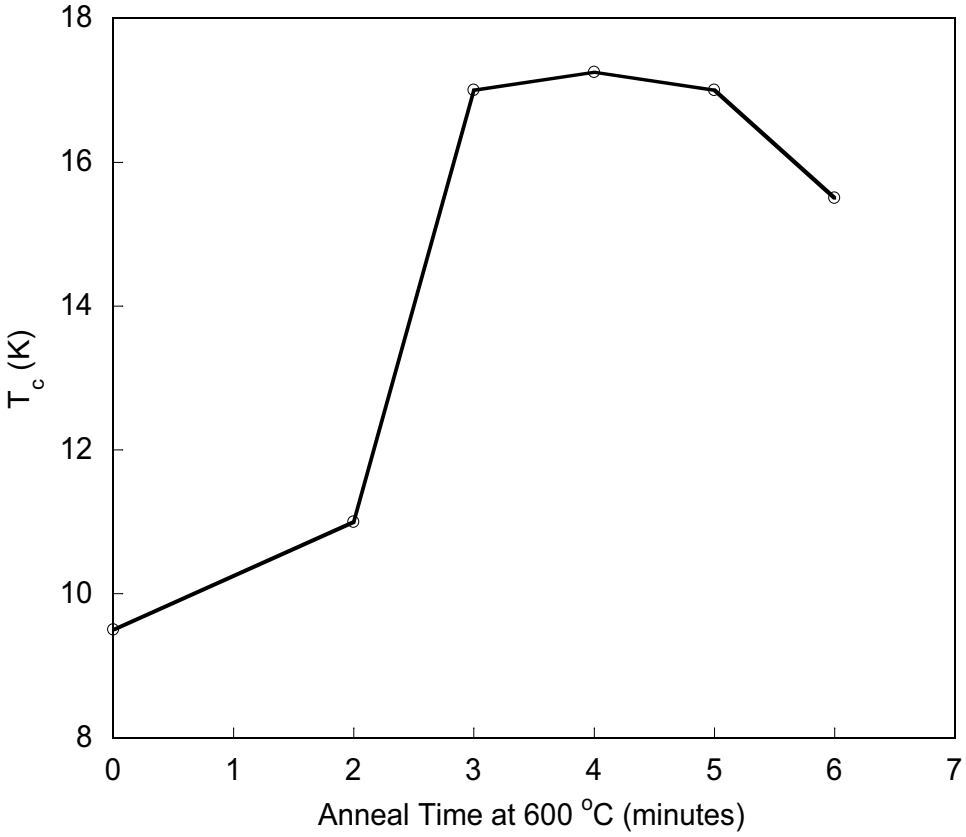

Figure II.8: Superconducting critical temperature T_c versus anneal (dwell) time at 600^o C.

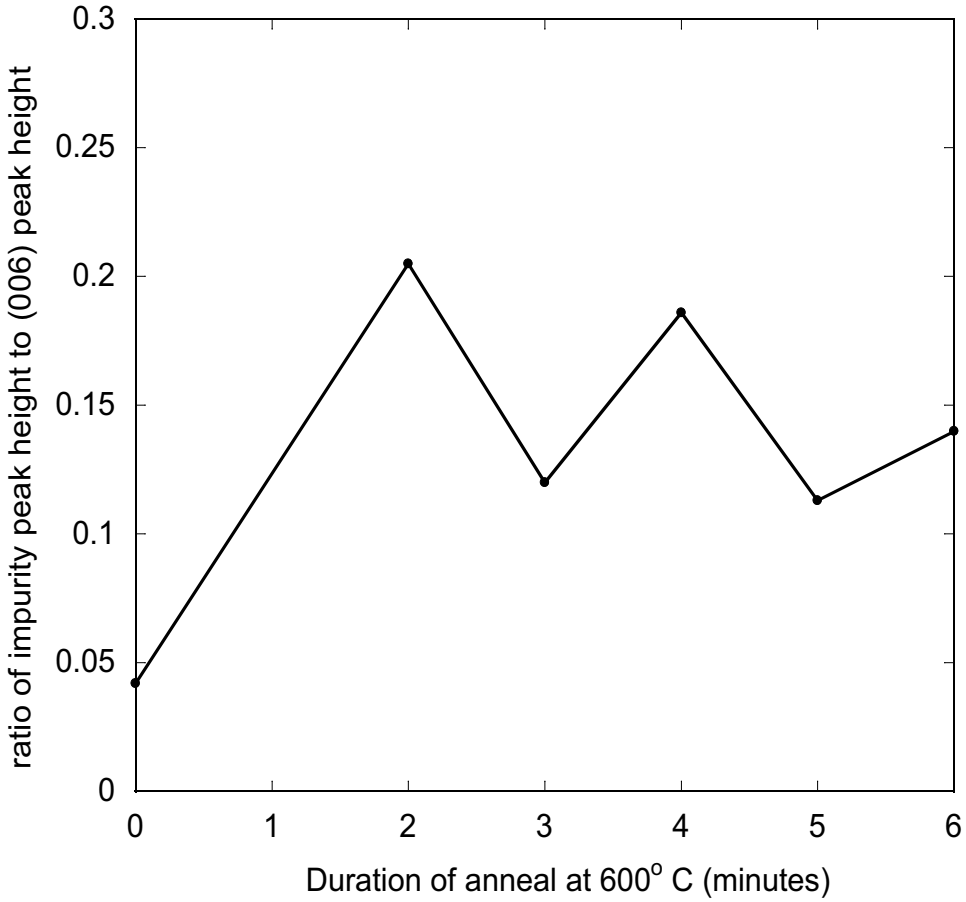

Figure II.9: Ratio of impurity phase peak height to (006) peak height versus anneal time showing minimal change over the duration of anneal.

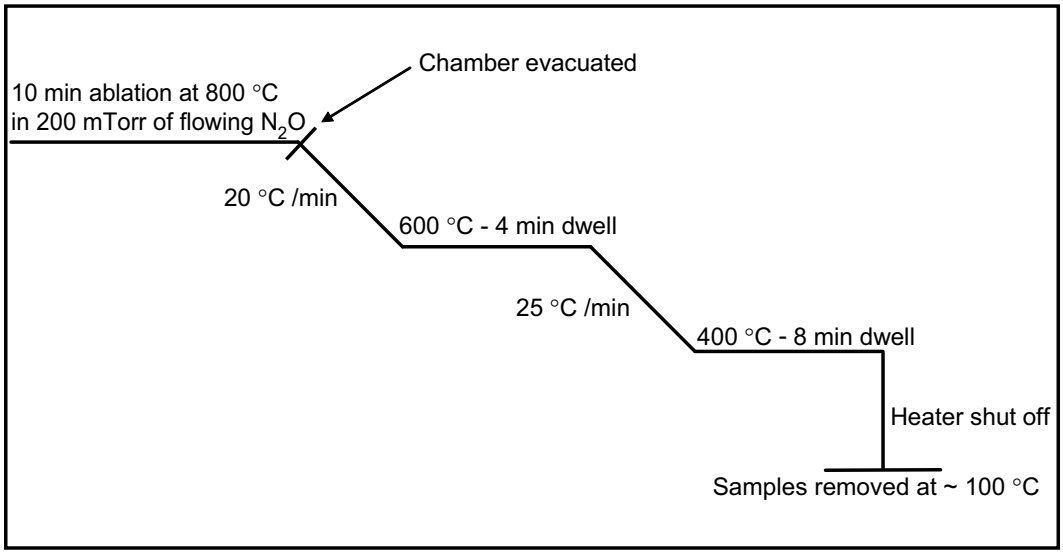

Figure II.10: Graphical of the growth conditions used for all of the film growths.

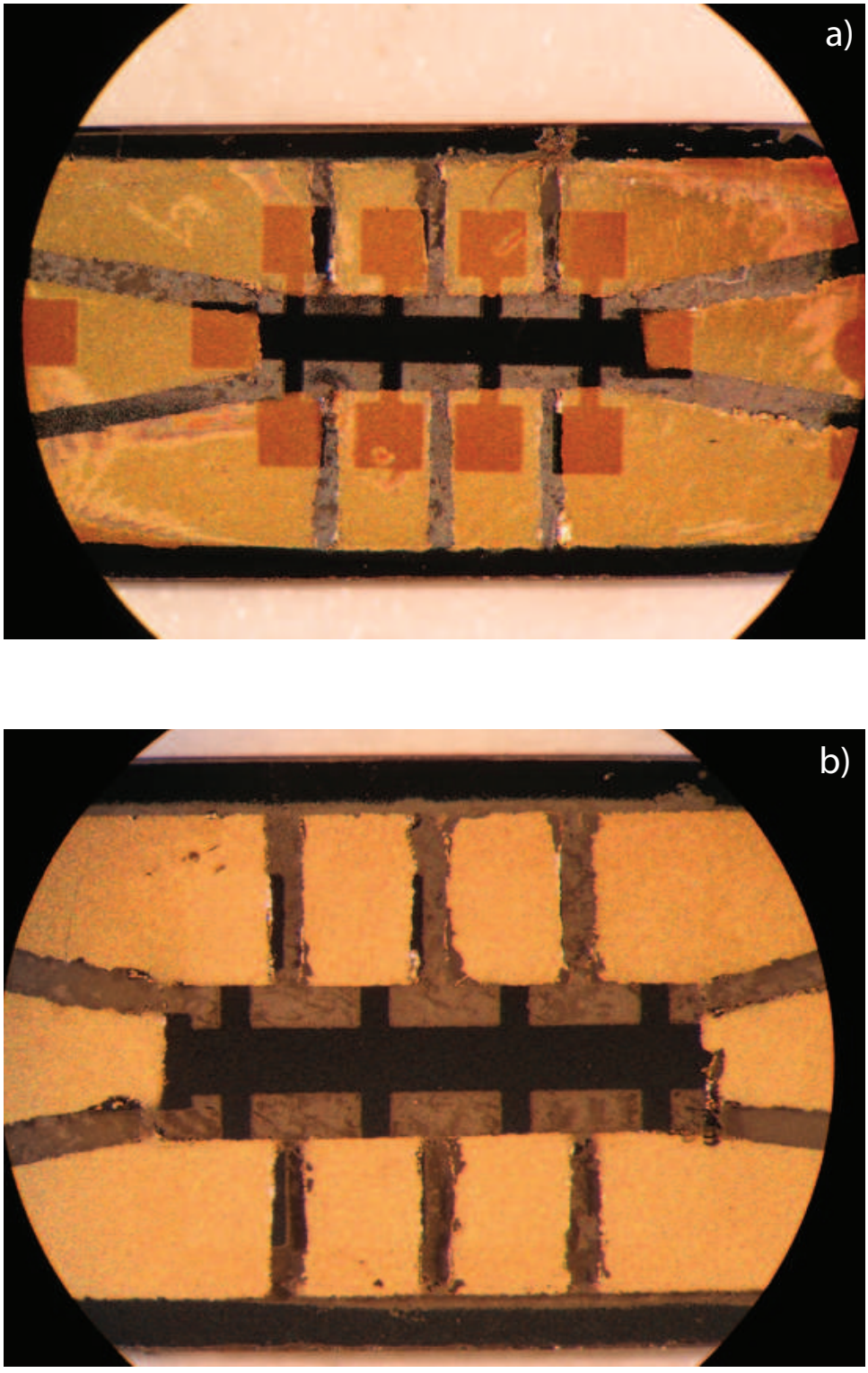

Figure II.11: a) Example of patterned film in the Hall bar geometry. b) Magnified view.

II.3 Electrical Transport Measurements

The majority of the electrical transport measurements were performed using a Quantum Design Physical Property Measurement System (PPMS) with temperature range 1.85 K $\leq$ T $\leq$ 310 K and magnetic field H range up to 9 T. The PPMS has a puck insert, Fig. II.12, capable of measuring two samples and also a horizontal sample rotator insert capable of measuring two samples through 360^o. Although the PPMS has its own software, custom LabView software was used for transport measurements utilizing a Keithley 220 programmable current source, a Keithley 2182 nanovolt meter, and a Keithley 706 scanner.

Additional experiments were carried out at the National High Magnetic Field Laboratory (NHMFL) in Tallahassee, Florida using the same instrumentation mentioned above. These experiments were carried out at low temperature and high magnetic field using either their 17.5 T superconducting magnet with portable ^{3}He-^{4}He insert capable of temperature as low as 250 mK or their 18 T superconducting magnet with top loading dilution refrigerator capable of temperature as low as 25 mK. The 18 T magnet also had a 16 pin sample rotator probe capable of rotating the sample 360^o.

II.4 Thermopower

The PPMS was used as the cryostat for these experiments. The original PPMS electrical transport puck was modified to carry out thermopower measurements. Fig. II.13 is a picture of the puck, with the modifications described below.

A piece of copper was machined and attached to the puck to hold three bracket shaped posts. These posts were bound together using Kapton tape and press fit into the copper holder. Two Cernox CX-1050 resistive chip thermometers were used to measure the temperature gradient across the sample, i.e. T^+ and T^-. The thermometers were suspended from the bracket posts using Evanohm wire and connected to the sample via a platinum wire. A Vishay N3K-XX-S022H-50C

Figure II.12: Photograph of the PPMS sample puck with two samples mounted for a four-wire resistivity measurement.

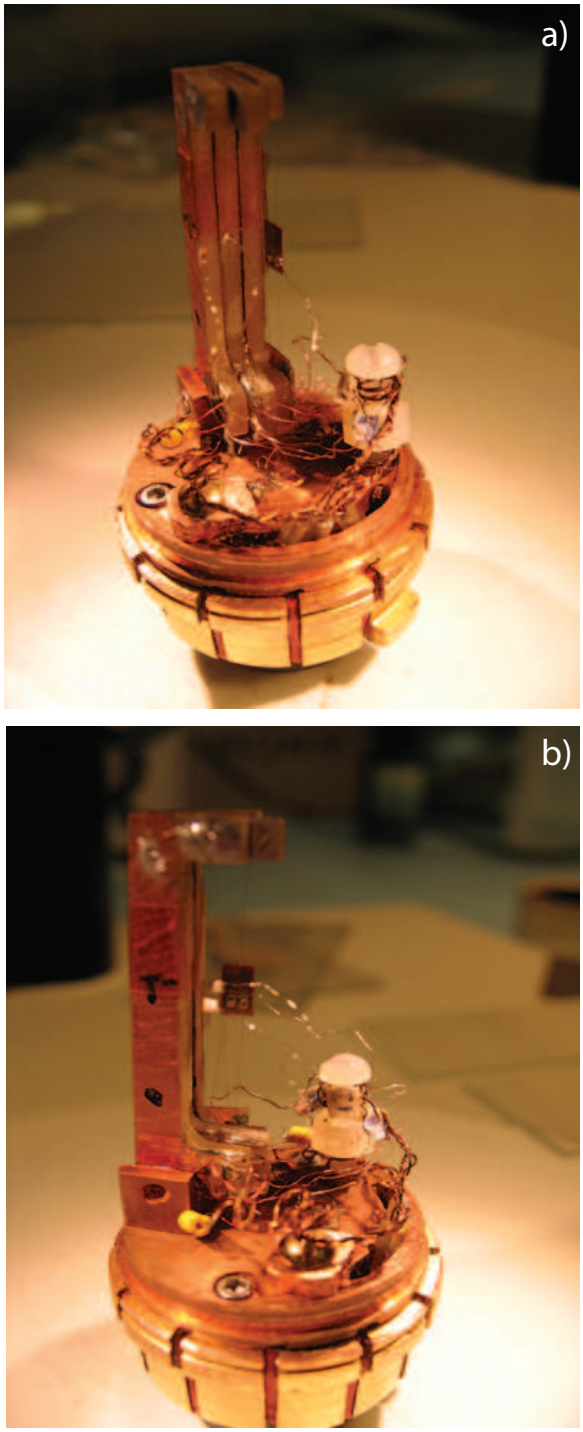

Figure II.13: Photograph of the modified PPMS puck used for thermopower measurements. a) Side view. b) Front view.

strain gauge was used as the heater. The heater was connected to the sample on the "hot" side via a silver wire, while the other "cold" side was connected to the copper block (thermal ground) thus establishing a temperature gradient across the sample. All wire leads were attached using DuPont brand silver paint.

The temperature was inferred (calibration described below) from the resistance of the thermometers read from two Stanford Research Systems SR830 lock-in amplifiers, each with a $\sim$ 1 MΩ current limiting resistor to provide a 1 μA excitation current to the Cernox thermometers. A Keithley 220 programmable current source was used to source current to the strain gauge heater, and a Keithley 2182 nanovolt meter was used to read the thermoelectric voltage. This was all controlled with a LabView program. Additionally, an external vacuum pumping station (mechanical pump and turbo pump) was attached via a bellows assembly in order to continuously pump on the sample space with typical pressures of $\sim$ 7 x 10^{-7} Torr.

Once the sample was secured to the mount on the puck, the puck was inserted into the PPMS and the system was cooled and pumped to a high vacuum overnight. A sequence typically began with the setting of a temperature on the PPMS, the stability of the two attached thermometers was logged to ensure they came to thermal equilibrium, and then the measurement was performed. An in-situ temperature calibration was done for all the measurements. This was done by taking a preliminary measurement of the thermometers with no heat applied to the sample, "heat off". When combined with the PPMS platform temperature, the "heat off" data yields a "calibration curve" of resistance (of the thermometers) versus temperature T. Then, applying current to the heater, a thermal gradient is created across the sample, and the temperatures T^+ and T^- can be recorded. The data points from the "heat on" measurements will also yield a curve whose temperature can be found from comparison to the "heat off" resistance versus temperature "calibration curve". The voltage across the sample was also measured using the 2182 nanovoltmeter and this process was done at each temperature data

point.

III

Results and Analysis

III.1 Characterization of $Sm_{2-x}Ce_xCuO_{4-y}$ Thin Films

The thin film $Sm_{2-x}Ce_xCuO_{4-y}$ samples fabricated for this body of work were characterized using various equipment and techniques. The results from x-ray diffraction measurements are described in section III.1.1 and emphasize the c-axis orientation of the films. Sections III.1.2 and III.1.3 discuss the results of electrical transport measurements and thermopower measurements, respectively. Finally, sections III.2 and III.2.1 present analysis of the magnetoresistance data in terms of the vortex glass model.

III.1.1 X-Ray analysis

Standard Θ-2Θ measurements were made using a Rigaku DMAXB x-ray diffractometer. The x-ray spectra were compared to standard peaks from powder diffraction files. Plots of the x-ray spectra are shown in Figs. III.1 and III.2.

The diffraction patterns are consistent for all samples and, in addition to the substrate peaks, the major peaks are associated with the (001) reflections, indicating excellent c-axis orientation. There are two minor peaks associated with an "impurity phase" and these peaks were minimized during growth optimization; however, they could never be completely removed and are discussed further in the next paragraph.

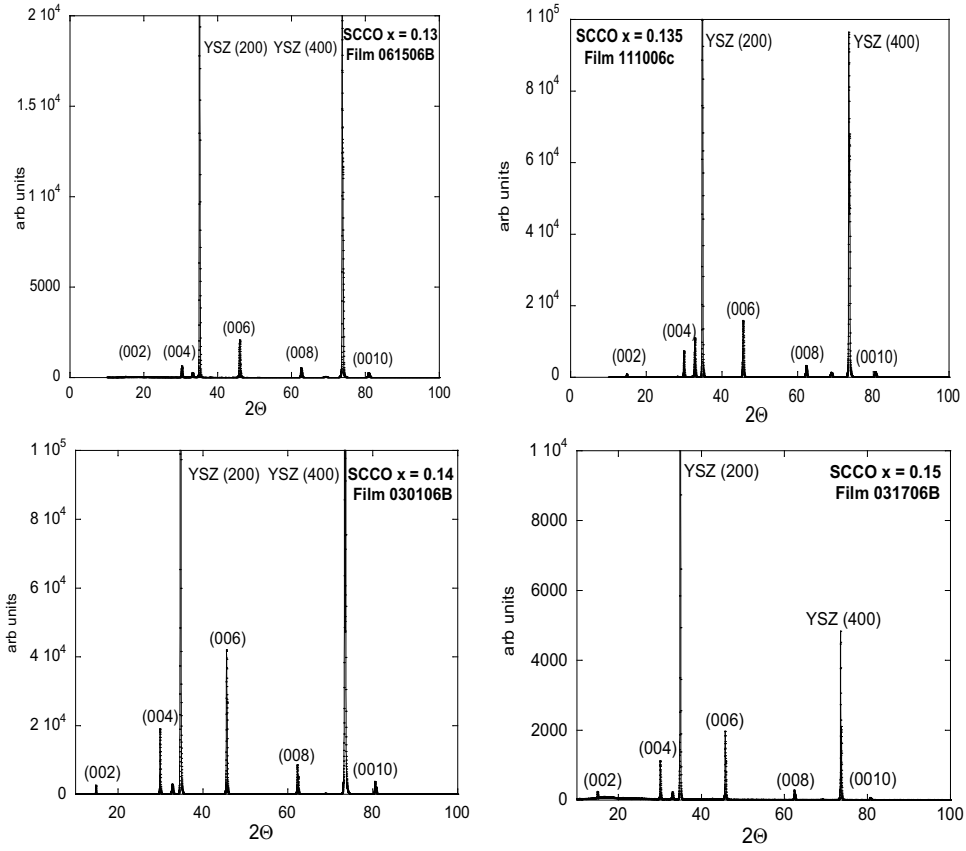

Figure III.1: X-ray diffraction patterns for thin film samples of $Sm_{2-x}Ce_xCuO_{4-y}$, with cerium concentrations x = 0.13 to x = 0.15. Along with the large substrate peaks, the spectra show orientation along the c-axis with their major reflections.

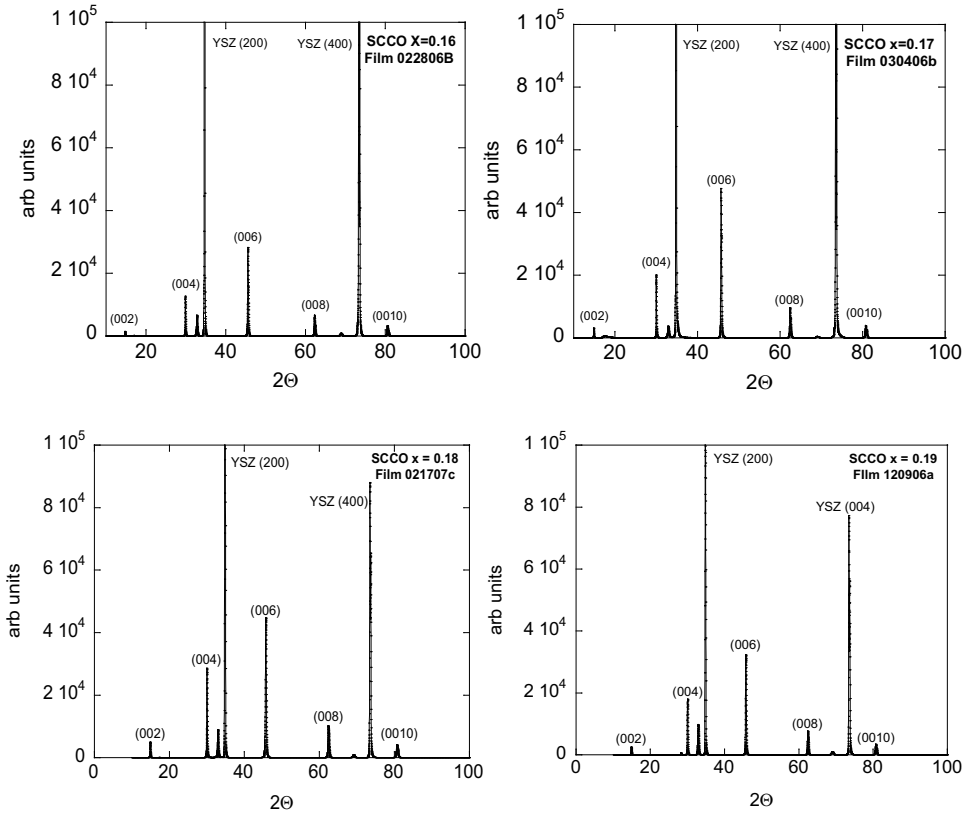

Figure III.2: X-ray diffraction patterns for thin film samples of $Sm_{2-x}Ce_xCuO_{4-y}$, with cerium concentrations x = 0.16 to x = 0.19.

The "impurity peaks" are analogous to those seen in NCCO samples and there is speculation to the origin of the peaks, but the issue is controversial and currently unresolved. In the first growth of thin films of NCCO [67], it was reported that there was an appearance of two diffraction peaks in addition to the substrate peaks and the (00l) reflections of NCCO. The authors of this work associated the two peaks with the (110) orientation. Subsequent work on NCCO thin films grown by PLD [68] and sputtering [61] both showed the presence of these peaks, and also associated them with the (110) orientation. However, in work done by Beesabathina et al. [69], the authors again found these same peaks, but performed a very detailed structural analysis on the films using TEM. They then associated these peaks not with the (110) orientation, but with an impurity phase of cubic $Ce_{0.5}Nd_{0.5}O_{1.75}$ (CNO). EDX measurements were performed on these films and confirmed the lack of Cu in these grains. They also found that the CNO content varied depending on the growth gas used and was 5 - 6 volume % for growth in O_2 but decreased to a mere 1 - 2 volume % using N_2O. Later work proposed that during the oxygen reduction annealing process, apical oxygen atoms were being removed [70]. This picture was challenged by Raman spectroscopy, infrared transmission, and ultrasound measurements [71–73] and suggested that oxygen was removed from the CuO_2 plane. However, the most recent study [74] found on this so-called "materials problem" proposes that this "impurity phase" is actually responsible for superconductivity in the electron-doped compounds. During the high temperature oxygen reducing anneal, the authors claim the compound phase separates into this small Cu free "impurity phase" and a "Cu-perfect" $Ln_{2-x}Ce_xCuO_{4-y}$ phase. Effectively, this allows any Cu vacancies in the $Ln_{2-x}Ce_xCuO_{4-y}$ phase to be filled by the Cu atoms freed in the phase separation and creation of the Cu free Ln_2O_3 phase. The model proposed can be summarized as:

I) Cu deficiencies in as grown (not annealed) materials leads to more O per Cu and increases the number of holes and thus negates effects of electron-doping with Ce atoms

II) Annealing the materials minimizes Cu deficiencies and encourages the effect of electron-doping with Ce atoms.

In any case, this is an important issue that needs to be explored further. It would be interesting to fabricate SCCO samples without annealing and see how both the "impurity phase" and electronic properties evolve with annealing and then re-oxygenation.

Scanning electron microscope (SEM) images were taken on several of the SCCO samples and a few are shown in Fig. III.3. These images show the smooth nature of the films and lack or large particulates.

III.1.2 Electrical Transport

Standard four wire electrical transport measurements were performed on all concentrations of the films produced. Plots of the resistivity, ρ(T), as a function of temperature with zero applied magnetic field are shown in Figs. III.4 and III.5.

The superconducting transition temperature, T_c, was determined for each of the films as the temperature at which the resistivity drops to 50% of its normal state value, just above T_c. The transition width, ΔT_c, is taken as the difference in temperature between the 10% - 90% drop in the normal state resistivity values. Table III.1 shows the values extracted for each of the concentrations measured.

From these data, we can construct a temperature T versus Ce concentration x phase diagram displaying T_c for each of the concentrations measured, similar to the ones presented in Chapter I for NCCO and PCCO. The phase diagram of SCCO, shown in Fig. III.6, is quite similar to the other electron-doped compounds with optimal doping at x = 0.15. There is a very rapid increase in T_c from the underdoped samples to the optimally doped sample and then a slower suppression of T_c with further doping beyond x = 0.15.

As discussed previously, the resistivity of the electron-doped compounds displays a T^2 behavior above T_c up to $\sim$ 200 K [75]. This is found in all the samples presented here. Fig. III.7 shows an example for two samples, one underdoped

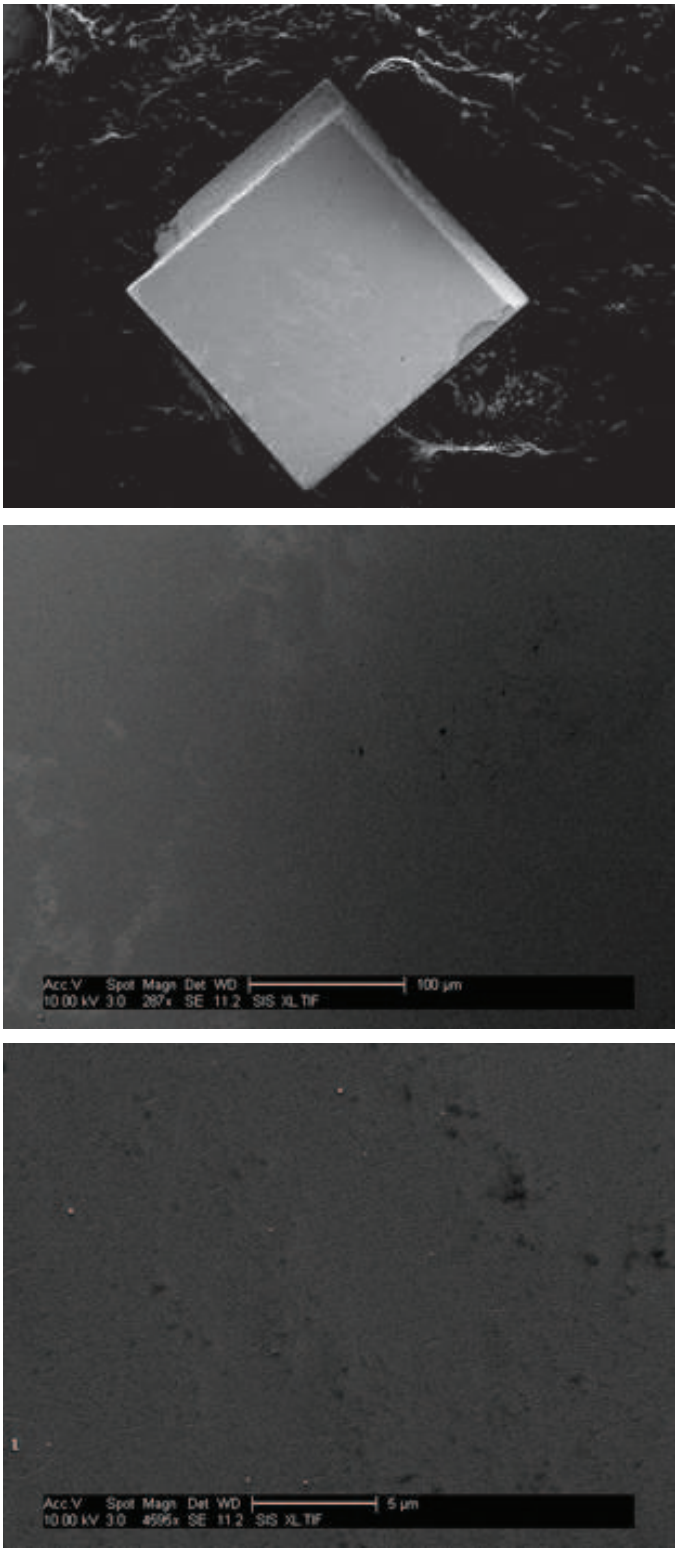

Figure III.3: SEM images of an SCCO film at various magnifications.

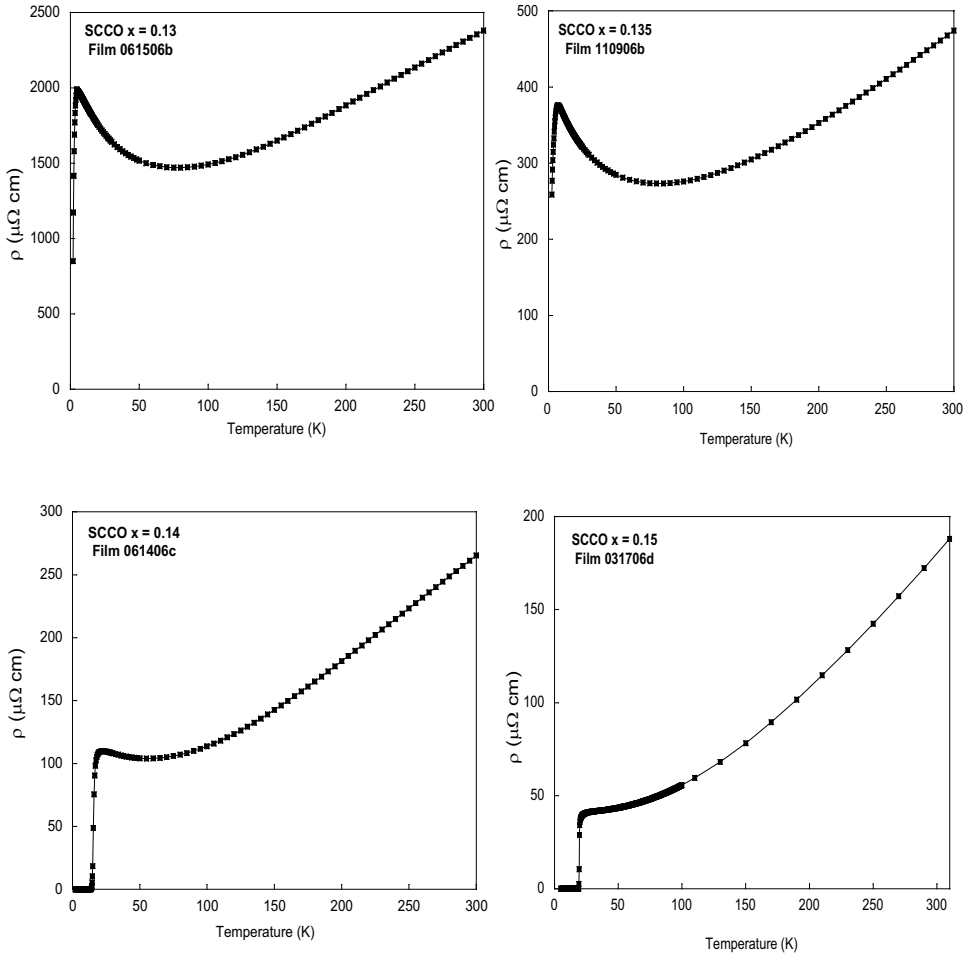

Figure III.4: Plots of resistivity ρ(T) versus temperature T for thin film samples of $Sm_{2-x}Ce_xCuO_{4-y}$ with x = 0.13 - 0.15.

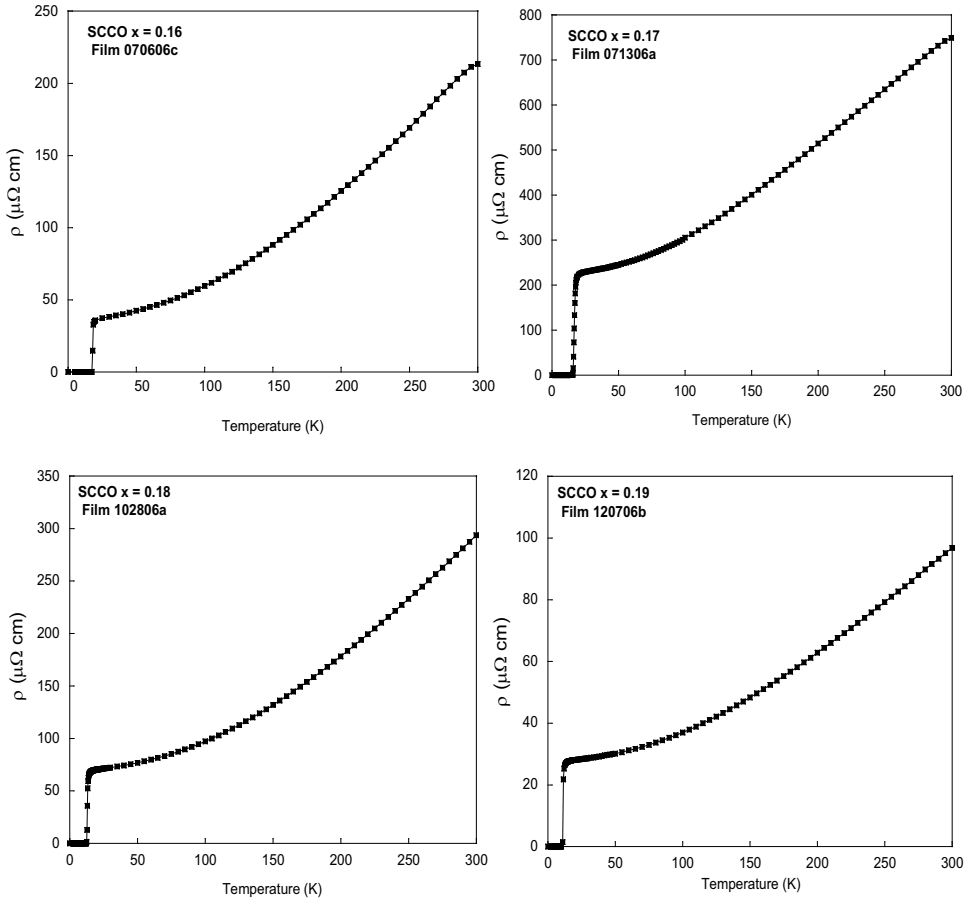

Figure III.5: Plots of resistivity ρ(T) versus temperature T for thin film samples of $Sm_{2-x}Ce_xCuO_{4-y}$ with x = 0.16 - 0.19.

Table III.1: Table of the superconducting critical temperature, T_c, and superconducting transition width, ΔT_c, for each Ce concentration, x.

Ce content x	T_c	ΔT_c
0.13	~ 2	NA
0.135	~ 2	NA
0.14	15.4	2.5
0.15	19.5	0.6
0.16	18.0	0.9
0.17	16.7	1.9
0.18	12.9	1.1
0.19	11.2	0.9

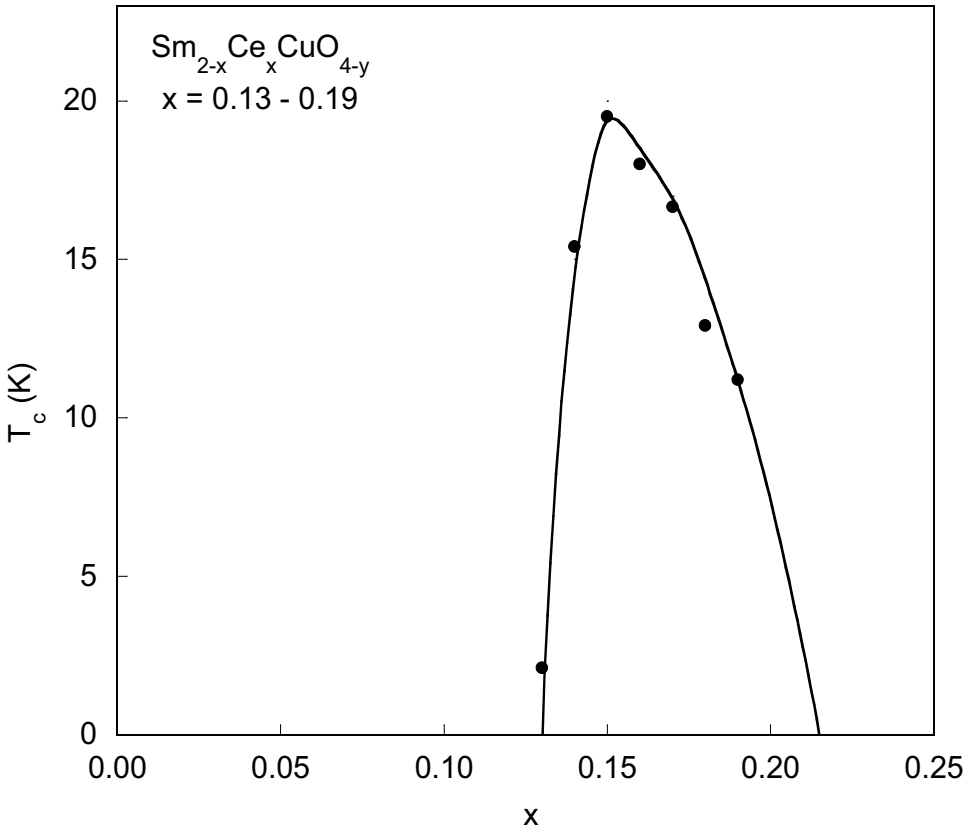

Figure III.6: Superconducting transition temperature, T_c, versus cerium concentration, x, for $Sm_{2-x}Ce_xCuO_{4-y}$ thin film samples with x = 0.13 to x = 0.19. The solid line is a guide to the eye.

sampled with x = 0.14, and one very overdoped sample with x = 0.19. Both are plotted as ρ versus T^2 since plotting in this manner will display T^2 behavior as a straight line. Since the underdoped samples, x = 0.13 to x = 0.14, had an insulator-like upturn in the resistivity above T_c this made the fitting window slightly smaller such that T^2 behavior was only observed from the minimum in the resistivity up to T $\sim$ 200 K. For concentrations, x = 0.15 to x = 0.19, T^2 behavior appears just above T_c to $\sim$ 200 K.

Magnetoresistance ρ(H, T) data was taken for $Sm_{2-x}Ce_xCuO_{4-y}$ films with cerium concentrations x $\geq$ 0.14. Measurements of ρ(H, T) for the x = 0.13 and x = 0.135 samples were not performed due to the very low temperatures needed for these measurements. Resistivity was taken as a function of temperature T and magnetic field H, always sweeping the temperature at fixed field. The data in Fig. III.8 are representative of that for all the samples measured. The superconducting transition temperature is suppressed with increased magnetic field down to the lowest temperature we were able to measure, T $\sim$ 2 K. The data were also used for scaling analysis of the resistivity data that is discussed in section III.2.

III.1.3 Thermopower

The thermoelectric power S of a material, also called the "Seebeck coefficient", is defined as the change in voltage across the sample divided by the change in temperature, or temperature gradient, across the sample:

$$S = \frac{\Delta V}{\Delta T}. \tag{III.1}$$

The thermoelectric current arises due to electron migration, or diffusion, from the hot side of the sample to the cold side. The electrons on the hot side of the sample will have more thermal energy and diffuse to the cold side leading to a thermoelectric current. This current will eventually be balanced by the electric field established from the buildup of electrons on the cold, thermally grounded

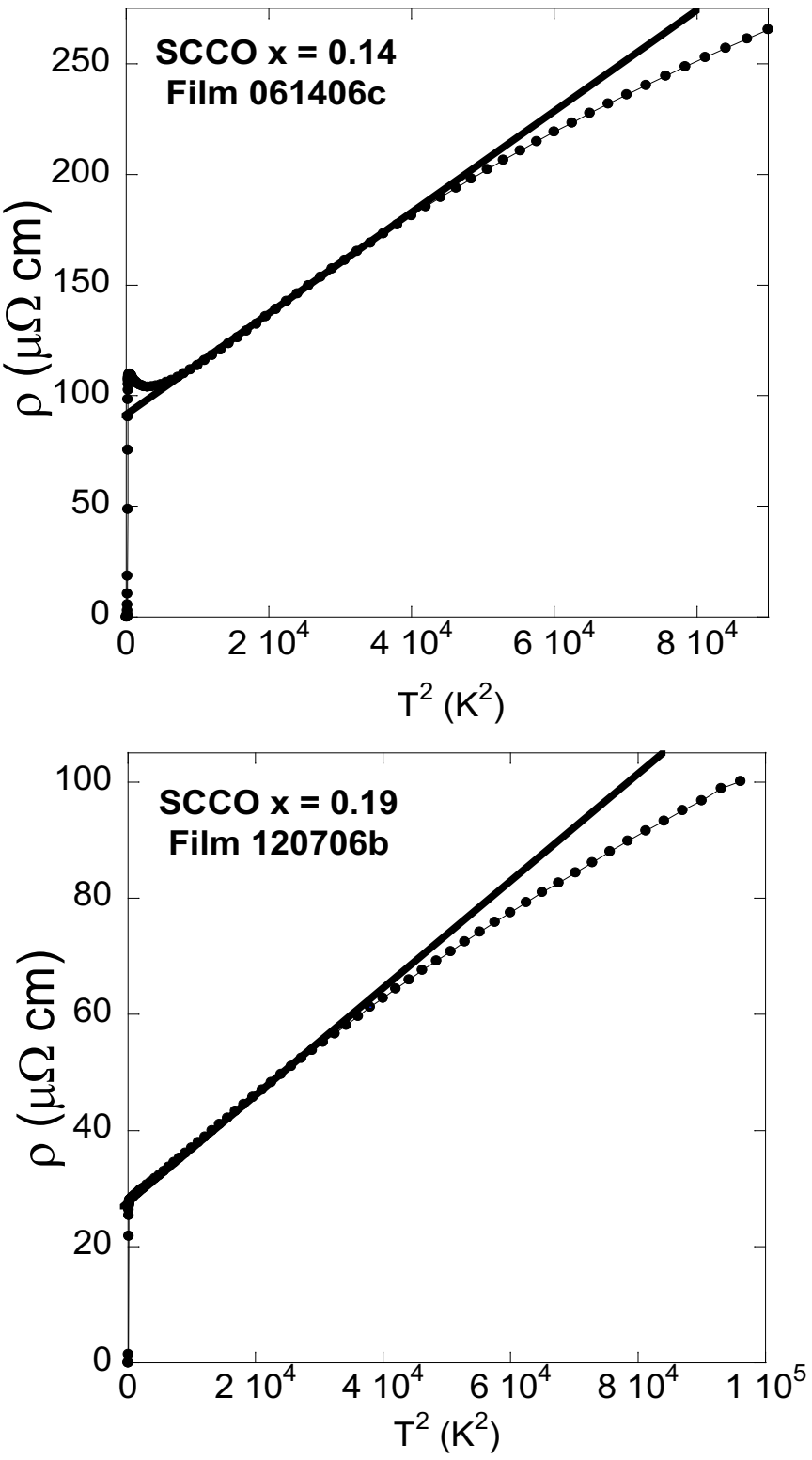

Figure III.7: Resistivity ρ versus T^2 for two samples with x = 0.14 and x = 0.19. The linear behavior shows the samples follow T^2 behavior over part of the region fit, indicated by the dark solid line that is a guide to the eye.

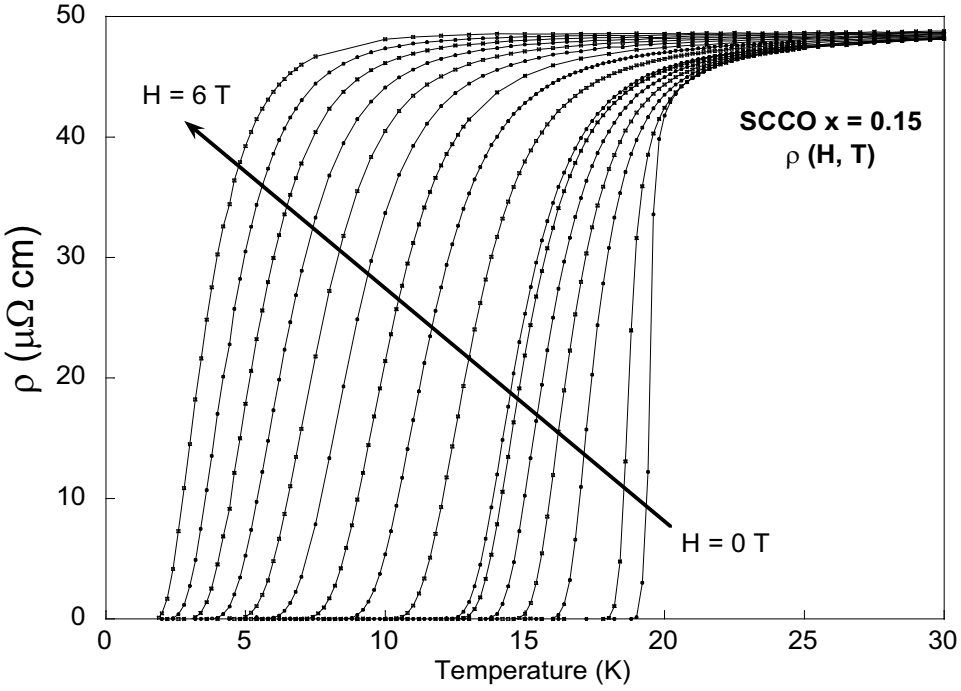

Figure III.8: Magnetoresistance, ρ(H,T), data for a $Sm_{1.85}Ce_{0.15}CuO_{4-y}$ sample, with 0 T $\leq$ H $\leq$ 6 T.

side of the sample. Similar to the Hall effect (discussed in section IV.2.3), the thermopower can be related to the carrier concentration and charge carriers in a material with S $\propto 1/ne$, where n is the carrier concentration and e is the charge of the carrier (i.e., negative for electrons and positive for holes). The thermopower of a material is a useful measurement in the high T_c materials since it can be related to the properties of the charge carriers, which is of interest with regard to the hole-doped and electron-doped compounds.

Thermopower data were taken on several of the SCCO thin film samples with varying cerium concentration. The thermopower S versus temperature T for all the concentrations measured is presented in Fig. III.9. It can be seen that there is a dramatic change in the thermopower from the underdoped concentrations to the overdoped. The underdoped samples have a large magnitude, negative thermopower that shifts with increasing Ce doping to a large positive thermopower voltage. Additionally, it can be seen that the thermopower for the optimally doped (x = 0.15) sample is very small in magnitude and negative at low temperatures and has a sign change at approximately 35 K. This data are compared to thermopower measurements on polycrystalline SCCO and thin films of PCCO and discussed below.

Yang et al. performed some early work on the thermopower of polycrystalline SCCO samples across the doping spectrum [76]. In the underdoped limit, the SCCO samples were found to have a large negative thermopower voltage, implying n-type carriers. The magnitude of the thermopower voltage decreased as the Ce content was increased until optimal doping at x = 0.15 where there was a sign change and a small positive signal (on the order of 1 μV/K) was observed. This small positive signal peaked and then hovered at ≈ 0.5 μV/K up to room temperature. Moving beyond optimal doping (x > 0.15), the thermopower voltage retained the same shape as that of the x = 0.15 sample; however, there was a sign change at higher temperature with a small magnitude (S ≤ 1 μV/K) negative voltage.

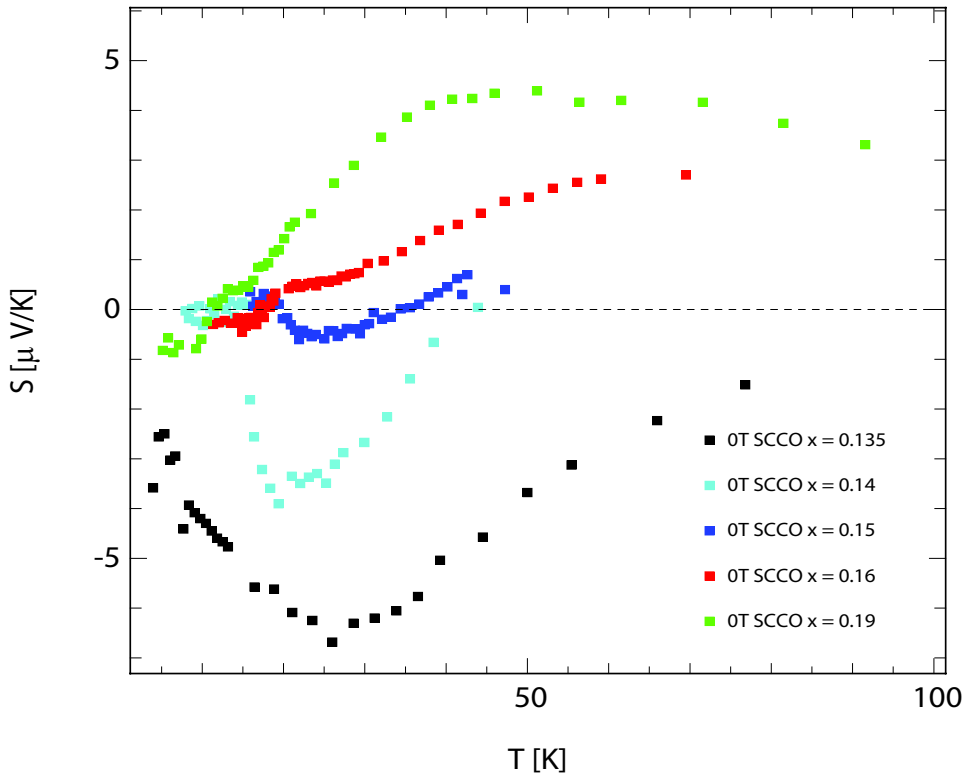

Figure III.9: Thermopower data of $Sm_{2-x}Ce_xCuO_{4-y}$ films with varying Ce content.

Recent thermopower measurements were performed on thin films of PCCO and were consistent with Hall effect measurements on the same samples [77]. The authors showed that the sign change in the thermopower was at the same temperature as that of Hall effect measurements. Their data are shown in Fig. III.10. Here it can be seen that the thermopower has a large negative value for underdoped films, decreasing in magnitude until the x = 0.16 overdoped sample, where the thermopower is positive above T_c until $\approx$ 25 K where it changes sign. Samples with x > 0.16 show a small magnitude positive value of S for all temperatures above T_c.

The results found in this study are similar to some of the results from the polycrystalline SCCO study, but are more consistent with those seen in the PCCO thin films. One possible reason for the difference is in the nature of the samples themselves, since both thin film studies produced c-axis oriented films and measurements were performed in the ab-plane. The differences in the polycrystalline SCCO study could be attributed to the many grains of different orientation and possible oxygen inhomogeneities in the grains. Therefore, we compare our data with the PCCO thin films and find the only significant difference is the cerium concentration at which there is a sign change in the thermopower. This is observed at optimal doping (x = 0.15) for SCCO as opposed to that observed in the overdoped (x = 0.16) PCCO. Qualitatively, the data behave as one would expect up to about optimal doping. Increasing the cerium content in the samples implies an increase in the carrier concentration. The thermopower is inversely proportional to the carrier concentration so the magnitude of the thermopower is expected to decrease with increased doping. In all of the samples mentioned above, there is a sign change in the measured thermopower voltage as a function of cerium concentration. In both cases mentioned above, this was explained in terms of a two-band model with a compensation at some critical doping level (x_c), above which the hole contribution dominates. Again, the data presented here appear to be consistent with the data on PCCO and also seems to invoke a two-band model. Hall effect

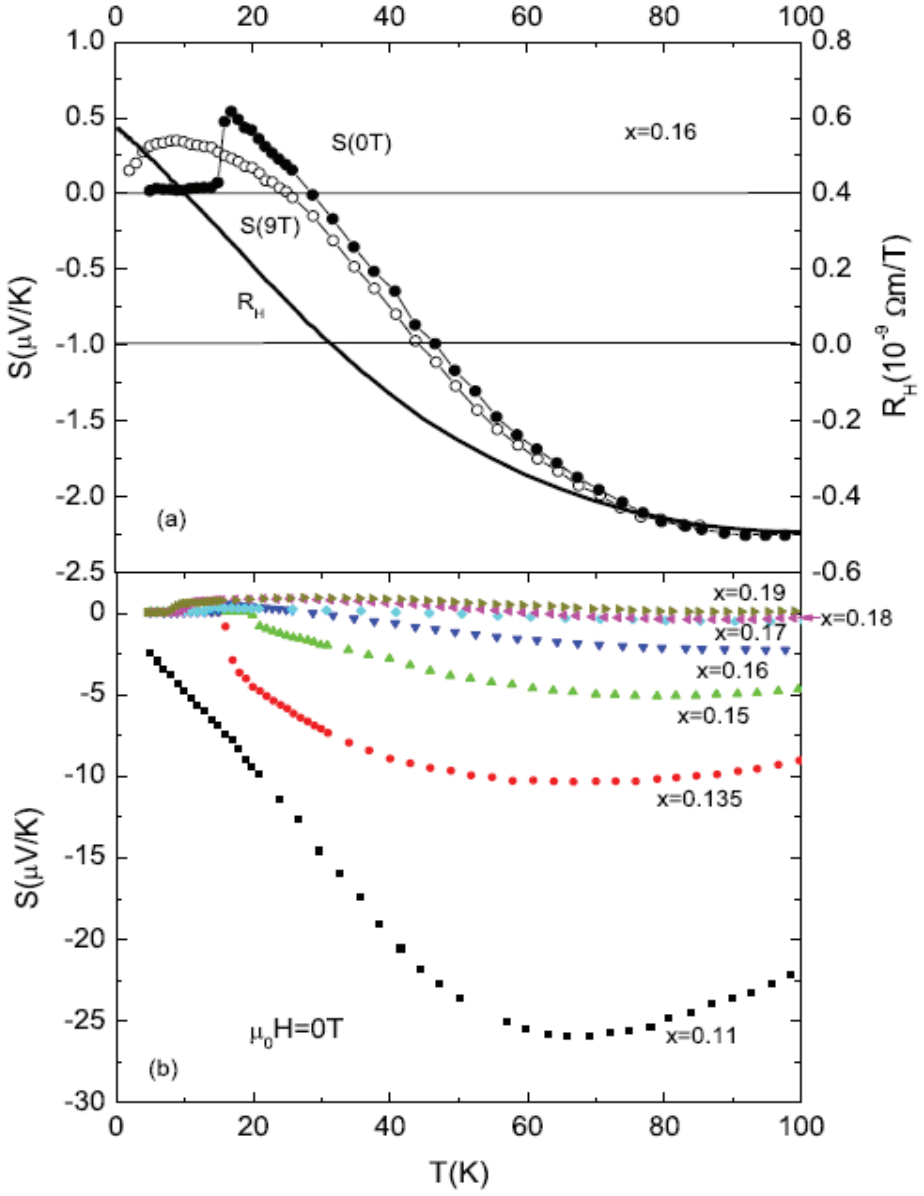

Figure III.10: Thermopower of thin films of $Pr_{2-x}Ce_xCuO_{4-y}$ from Ref. [77]. a) Thermopower and Hall coefficient for PCCO film with x = 0.16. b) Thermopower of several PCCO thin films with varying Ce concentration.

measurements could confirm the thermopower data and sign of the charge carrier in this system.

III.2 Vortex-glass Scaling Analysis

The magnetoresistance data were analyzed in the context of the Fisher-Fisher-Huse (FFH) vortex glass scaling model that was discussed in the introduction. Early work on SCCO seemed to indicate that there is an enhancement in the vortex glass melting line around the Sm^{3+} antiferromagnetic transition, $T_N \sim 6$ K [57]. Not only were these effects studied in an optimally doped sample, with x = 0.15, but also in the underdoped and overdoped regions to explore any effects of cerium doping on the vortex glass state.

In the critical region, at temperatures above the vortex glass melting temperature T_g, the resistivity conforms to the form:

$$\rho = \rho_o \left| \frac{T}{T_g} - 1 \right|^{\nu(z+2-d)} . \tag{III.2}$$

However, assuming the dimensionality of the system, d, is equal to 3, Eqn.(III.2) can be rewritten as:

$$\rho = \rho_o \left| \frac{T}{T_g} - 1 \right|^{\nu(z-1)} . \tag{III.3}$$

Upon taking the derivative of ρ with respect to T, the following expression is obtained:

$$\left(\frac{dln\rho}{dT} \right)^{-1} = \frac{T - T_g}{\nu(z-1)} \tag{III.4}$$

and by plotting (dln ρ/dT)$^{-1}$ vs T, we expect to find a region of linear behavior from which the values of T_g and ν(z-1) can be extracted. The x-axis intercept is T_g and the slope of the line is the critical exponent ν(z-1). A plot of (dln ρ/dT)$^{-1}$ vs T for an SCCO sample with x = 0.15 is shown in Fig. III.11.

This scaling was performed on the data for each magnetic field applied to the samples with cerium concentration x $\geq$ 0.14. The data shown in Fig.(III.11) represents some of the best data. However, Fig. III.12 depicts more typical data.

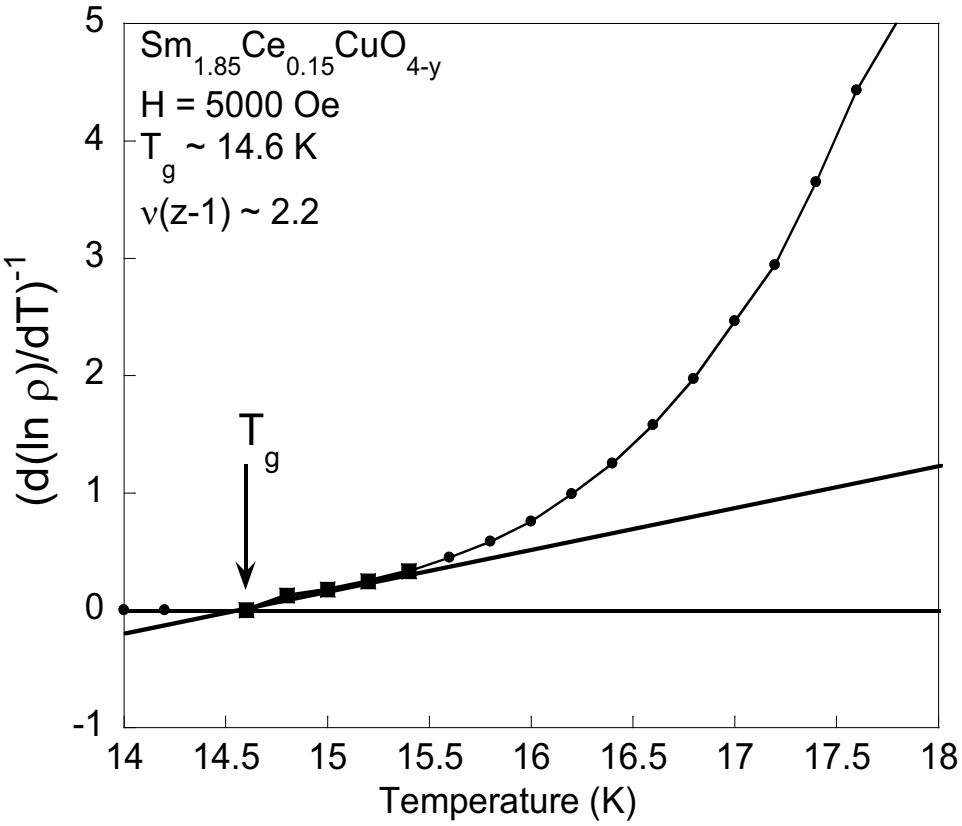

Figure III.11: Scaled resistivity $(\mathrm{dln}\ \rho/\mathrm{dT})^{-1}$ vs T for the optimally doped $Sm_{1.85}Ce_{0.15}CuO_{4-y}$ sample. The dark line is a guide to the eye through the region of interest. The intercept corresponds to T_g and the slope of the line yields ν(z-1).

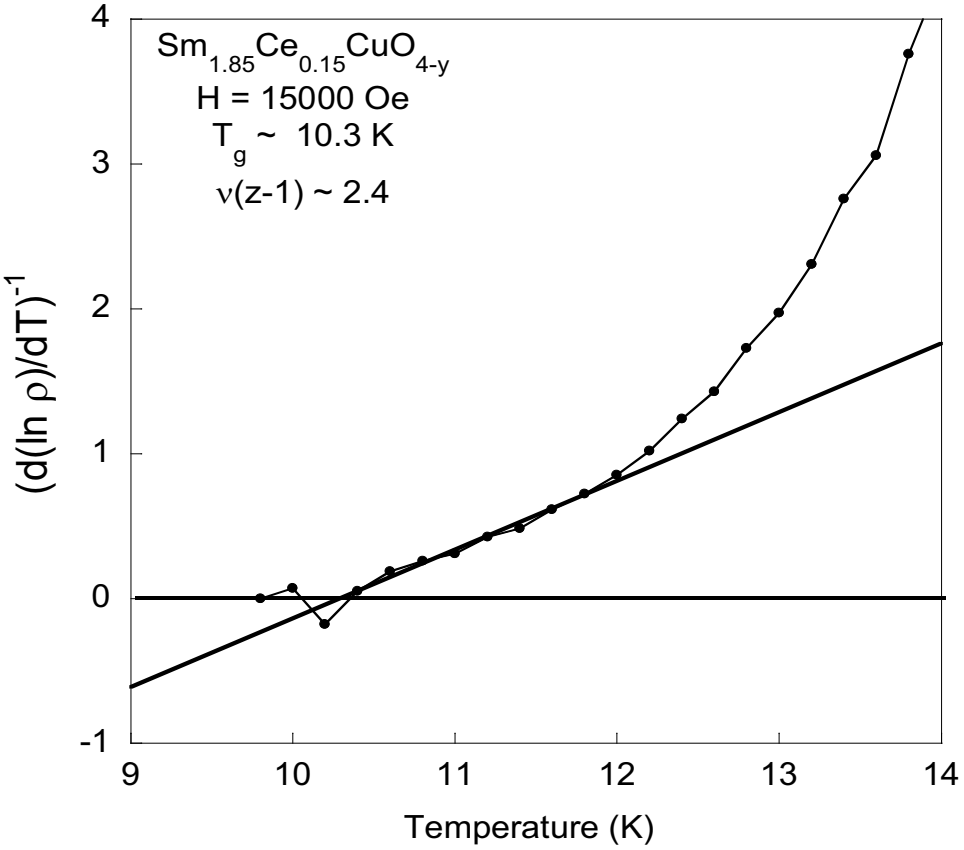

Figure III.12: Scaled resistivity dln ρ/dT vs T for the optimally doped $Sm_{1.85}Ce_{0.15}CuO_{4-y}$ sample. Again, the dark line is a guide to the eye through the region of interest; however, the data are not as smooth as those shown in Fig.(III.11)

It can be seen that the region of vanishing linear resistivity is not readily apparent. This made an accurate analysis more challenging, resulting in a larger uncertainty in the values obtained for T_g and ν(z-1).

In addition to the Fisher-Fisher-Huse (FFH) model, a modified vortex glass theory proposed by Rydh, Rapp, and Andersson (RRA) [78] was also used to analyze the data. The RRA model produces a modified scaling expression for the resistivity in the critical region and is given below. The modified scaling expression was very successful in accurately describing the data. The RRA model differs from the FFH model in that the authors claim the energy scale changes with both temperature and magnetic field such that the vortex glass transition is dependent on the energy difference k_BT - U_o(H, T), where U_o is the current independent mean pinning energy. Qualitatively speaking, this can be thought of in terms of using the two dimensional distance in the H-T plane to traverse to T_g, instead of taking the usual one dimensional distance in temperature to T_g at a constant H. This is shown pictorially in Fig. III.13. Physically, this implies that the vortex glass transition is strongly influenced by the effects of the magnetic field on the pinning landscape. The addition of U_o leads to modifications of the vortex glass scaling equations beginning with the introduction of a modified expression for the vortex glass correlation length ξ_g(T). Recalling the expression for the vortex glass correlation length from FFH:

$$\xi_g(T) \propto \mid T - T_g \mid^{-\nu} \tag{III.5}$$

RRA propose that this is replaced by the following expression for ξ_g:

$$\xi_g = \xi_g(0) \left| \frac{k_B T}{U_o} - 1 \right|^{-\nu} \tag{III.6}$$

where the mean pinning energy U_o(H,T) = k_BT_g. Continuing on, recall that near the vortex glass melting temperature the linear resistivity in the FFH model takes the form

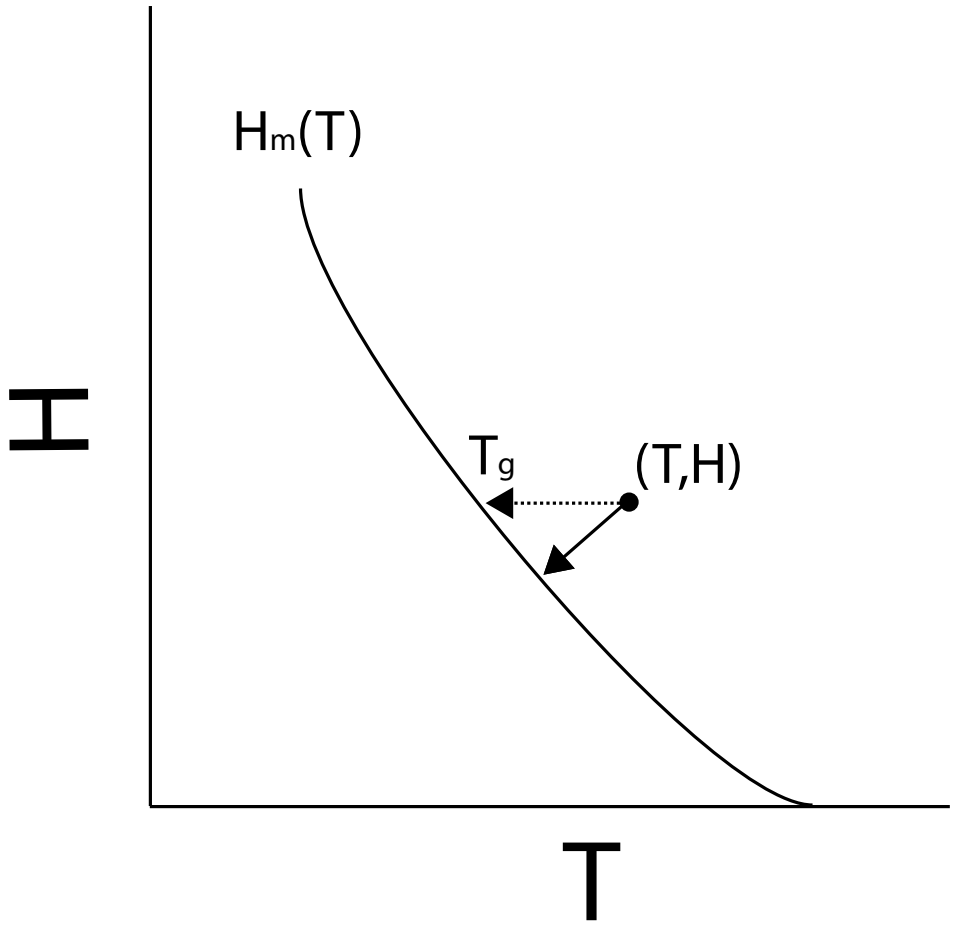

Figure III.13: Cartoon diagram explaining the physical principle behind the RRA model. At a specific point (T,H), the energy scale U_o(H, T) is given by the distance to the vortex glass transition line H_m(T) in the H-T diagram rather than just the distance given by the temperature at constant H.

$$\rho = \rho_o \left| \frac{T}{T_g} - 1 \right|^{\nu(z-1)}. \tag{III.7}$$

Rewriting this, taking into account the field dependence of the pinning energy, RRA find instead,

$$\rho = \rho_o \left| \frac{k_B T}{U_o(H,T)} - 1 \right|^{\nu(z-1)}. \tag{III.8}$$

The effective mean pinning energy was empirically found to follow

$$U_o = k_B T_g \frac{T_c - T}{T_c - T_g}. \tag{III.9}$$

Finally, using the expression for U_o from Eqn. (III.9), Eqn. (III.8) can be re-written as

$$\rho = \rho_o \left| \frac{T(T_c - T_g)}{T_g(T_c - T)} - 1 \right|^{\nu(z-1)}, \tag{III.10}$$

where ρ_o is taken as the normal state resistivity just above T_c. Therefore, by plotting ρ/ρ_n vs $[T(T_c\text{-}T_g)/T_g(T_c\text{-}T)$ - 1] on a log-log plot, the resistivity data taken in various fixed fields should collapse onto a single curve, from which a value for T_g and ν(z-1) can be obtained. An example of this is shown in Fig. III.14 for an optimally doped single crystal of YBCO containing minimal disorder [79]. The dark line drawn through the data points is a guide to the eye. The slope of the line yields the critical exponent ν(z-1). The data for all the concentrations in this study also scale according to this relation and this is shown in the plots in Figs. III.15 and III.16.

A computer program was written in LabView in order to scale the data by this method, simultaneously, allowing all data to fall on the single curve. The raw data were imported into LabView and then the resistivity and temperature data were scaled as ρ/ρ_n and $T(T_c$ - $T_g)/T_g(T_c$ - T) - 1, respectively. The fitting parameter was the vortex glass scaling temperature, T_g, and could be adjusted such that each of the scaled curves would collapse on one another. The initial value of T_g

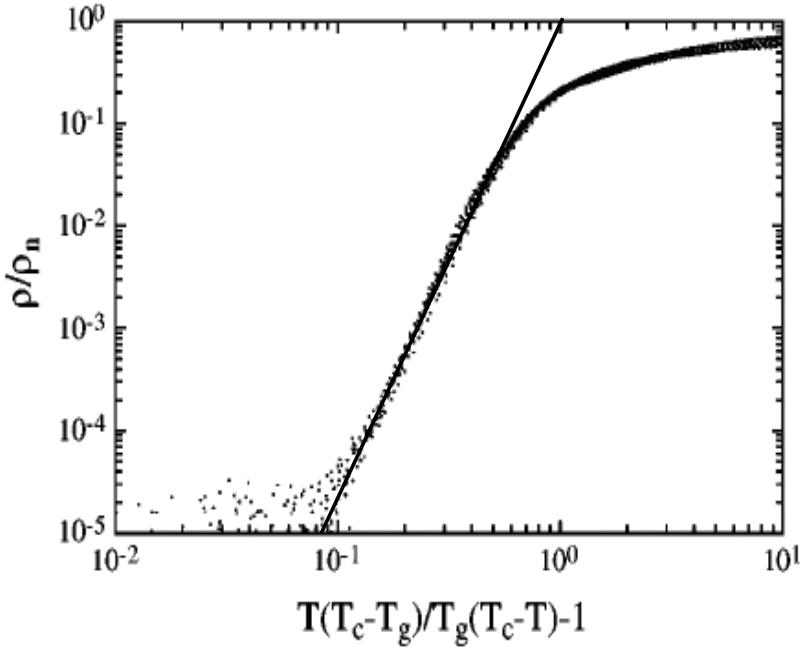

Figure III.14: Normalized resistivity versus scaled temperature as an example of the application of the RRA scaling model to an optimally doped single crystal of YBCO [79]. The solid line drawn through the points is a guide to the eye, with the slope of this line equal to the critical exponent, ν(z-1).

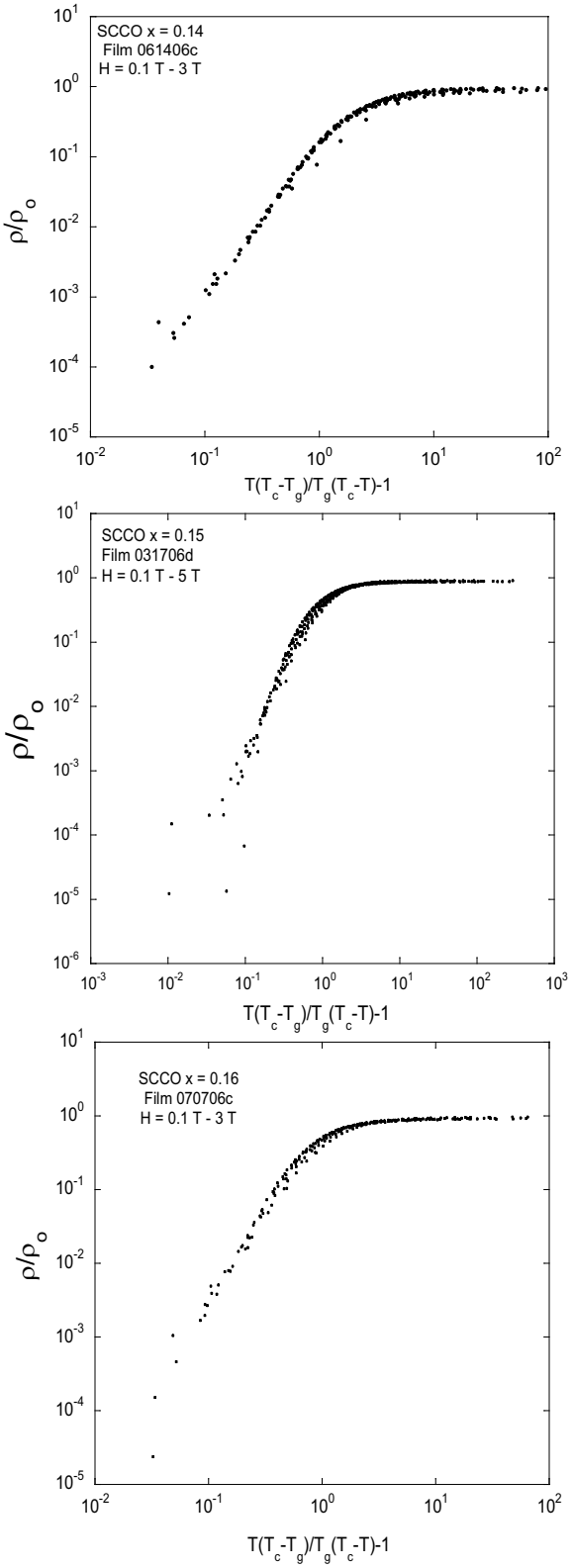

Figure III.15: Resistivity data scaled according to the expression ρ/ρ_n vs $T(T_c\text{-}T_g)/T_g(T_c\text{-}T)$ - 1 from the modified vortex glass model of RRA for samples with cerium concentrations x = 0.14 to x = 0.16.

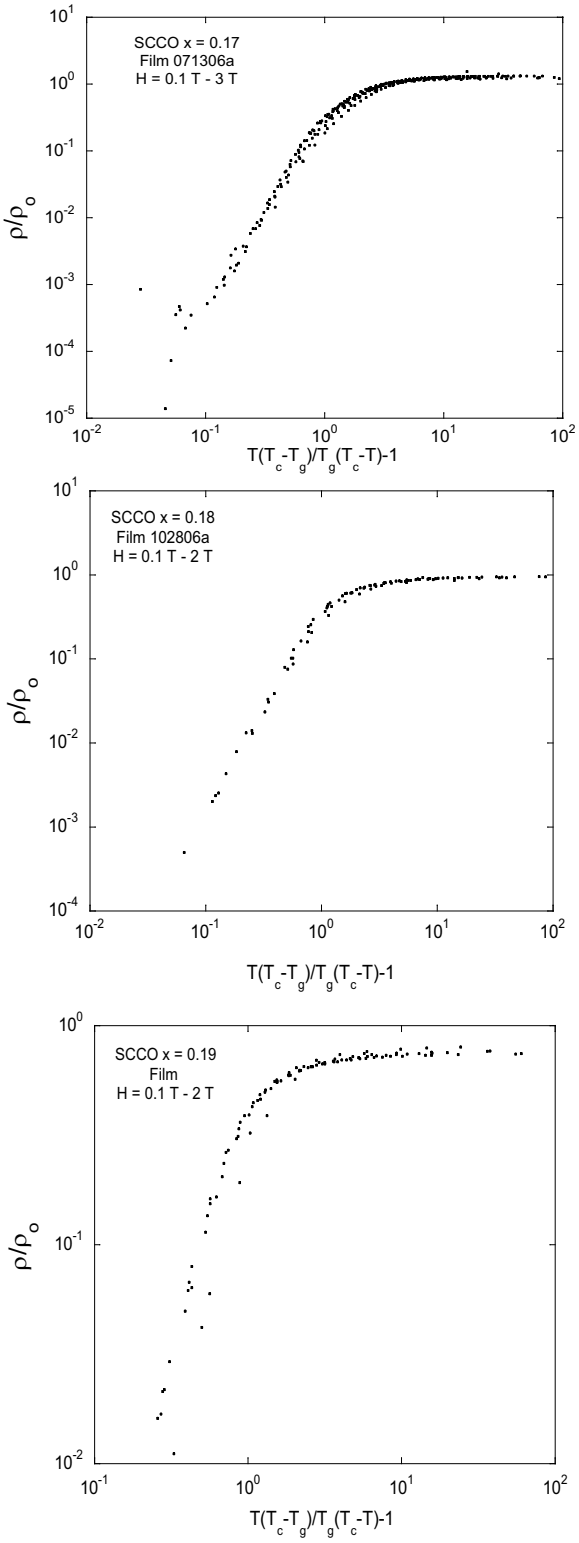

Figure III.16: Resistivity data scaled according to the expression ρ/ρ_n vs $T(T_c\text{-}T_g)/T_g(T_c\text{-}T)$ - 1 from the modified vortex glass model of RRA for samples with cerium concentrations between x = 0.17 and x = 0.19.

used was the one obtained from the FFH scaling analysis. This proved to be a good starting point and the vortex glass melting temperature was reasonably consistent between both methods. Thus, T_g could be extracted for each concentration at each magnetic field from the fit and the slope of the curve yielded the critical exponent, ν(z-1). The results can be summarize with a plot of the vortex glass melting lines in the H-T plane at differing cerium concentrations. This is shown in Fig. III.17.

Additionally, Fig. III.18 plots the average value of the critical exponent as a function of concentration. The underdoped x = 0.14 sample was found to have a noticeably lower value of the critical exponent, ν(z-1), while for dopings with $x \geq 0.15$, the critical exponent appears to be rather constant, within the estimated error.

Although both scaling models give results that are reasonably consistent, the data range for the fit of the expression from the RRA scaling model was much greater than that of the expression from the FFH model. Therefore, there was much less uncertainty in the extracted values obtained from the RRA model.

Work on SCCO single crystals performed by Dalichaouch et al. [57] revealed a kink in the log-log plot of the resistively measured H_{c2} vs reduced temperature (1-T/T_c). It was initially presumed by Dalichaouch et al. that this enhancement of H_g was due to the antiferromagnetic ordering of the Sm^{3+} ions, since the enhancement in H_{c2}(T) occurred at the Néel temperature and had been observed in the Sm-based antiferromagnetic superconductor $SmRh_4B_4$ at the Néel temperature [53, 54]. The superconducting critical temperature, T_c, of the sample in this study was $\sim$ 11 K; therefore, a value of $T/T_c \sim 0.5$ corresponded to the approximate temperature of the antiferromagnetic transition, T_N. However, de Andrade et al. [80] showed in their data that this kink does not correspond to the Néel temperature and concluded that there was no observable effect of the antiferromagnetism on the vortex glass melting curve. The kink in the data corresponded to $T/T_c \simeq 0.5$ and H $\simeq$ 10 kOe and was independent of sample, single crystal or magnetically aligned single crystal grains, and T_c.

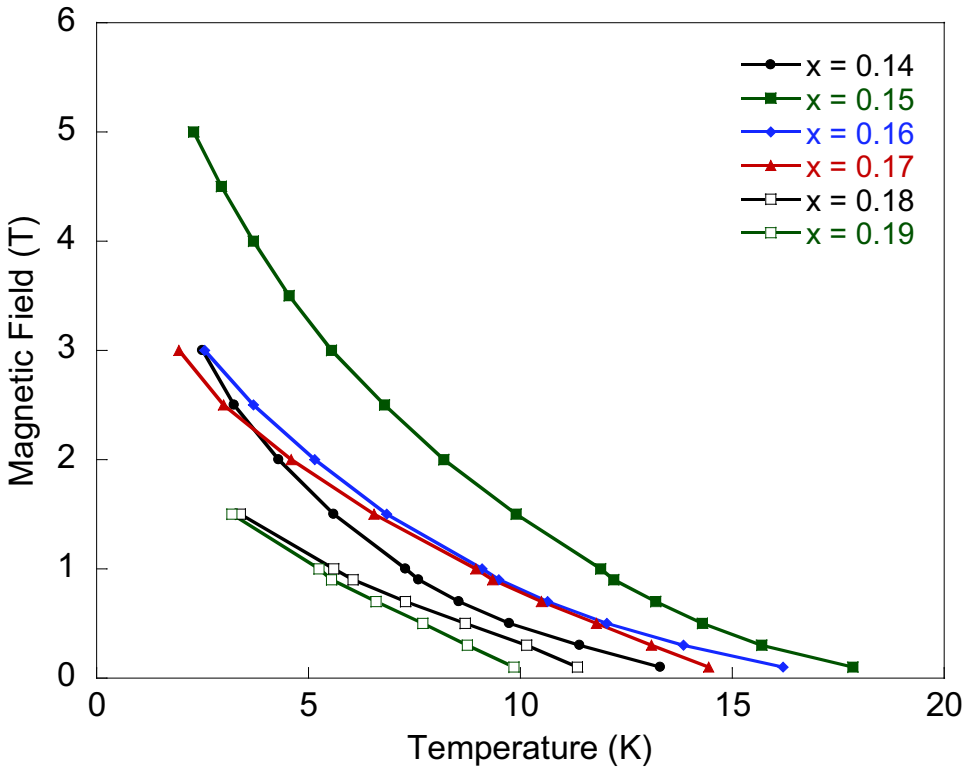

Figure III.17: Vortex glass melting lines, $H_g(T)$, determined via analysis in the context of the RRA model, for each cerium concentration x, with x = 0.14 to x = 0.19.

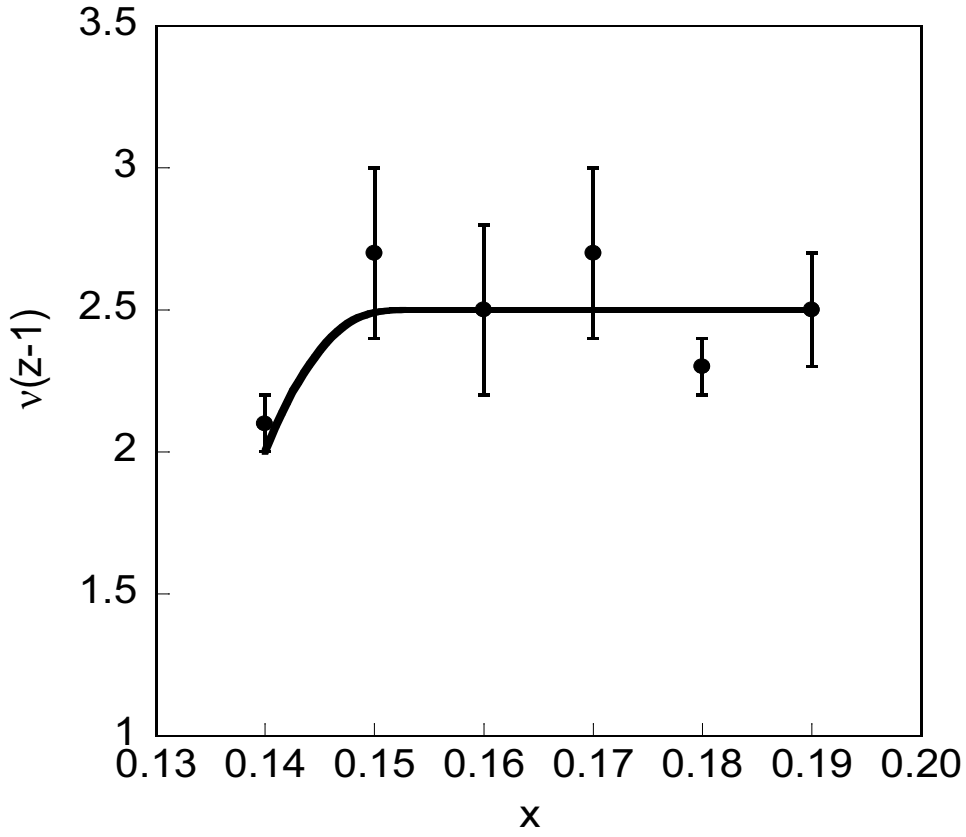

Figure III.18: Critical exponent ν(z-1) extracted from the RRA scaling analysis of the resistivity data plotted as a function of cerium concentration x.

Several studies of the vortex-glass scaling behavior of NCCO have also been performed [33, 81–83]. However, with the Néel temperature of NCCO of $T_N \approx 1.2$ K, only Hermann et al. have reported measurements on NCCO below T $\sim$ 4 K. Their results yielded a critical exponent, ν(z - 1), that ranged from 4.2 to 9.3, with no systematic variation. These values of ν(z - 1) are considerably higher than those found in our experiments on SCCO, where ν(z - 1) ranged from $\sim$ 2.1 to 2.7, over the entire temperature and magnetic field range studied. A more recent experiment on NCCO thin films [83] yielded an exponent $\nu(z - 1)_{avg} \sim 3.0$, which is more consistent with our data, but was taken at temperatures above the Néel temperature. In these bodies of work, no effect of the ordering of the Nd^{3+} could be established. It would also appear that in SCCO, there is no obvious change in the vortex glass scaling behavior indicative of antiferromagnetic ordering playing a role in the vortex glass state.

III.2.1 Angle Dependent Transport Measurements

The electrical resistivity of several $Sm_{2-x}Ce_xCuO_{4-y}$ samples with varying cerium concentration x was measured as a function of not only magnetic field, H, and temperature, T, but also angle, Θ, with respect to the c-axis. These measurements were also analyzed in the context of the FFH vortex glass model, looking at the evolution of flux pinning effects with angle, Θ. Electrical resistivity ρ(H, T, Θ) data were taken for samples with x = 0.14, 0.15, 0.16, and 0.17 at temperatures ranging from 2 K $\leq$ T $\leq$ T_c and in magnetic fields up to 9 T. Similar results were obtained for each concentration with no variation with respect to the critical exponent ν(z-1) from underdoped to overdoped. The x = 0.15 data will be presented, as behavior it displays is representative of samples over the doping range x = 0.14 to x = 0.17. Additional data were taken at the National High Magnetic Field Laboratory (NHMFL) in Tallahassee for an x = 0.15 sample using a top loading dilution refrigerator with a base temperature of 25 mK and a superconducting magnet capable of magnetic fields up to 20 T. Resistivity

measurements were performed at fixed temperature and angle while the magnetic field was swept continuously. These measurements were performed on two different x = 0.15 SCCO samples, the high temperature data performed on the sample used throughout this thesis and the low temperature data on a sample that had a slightly reduced T_c ($\sim$ 17.8 K). Instead of the temperature dependent scaling relation,

$$\rho(T) \propto \mid T - T_g \mid^{\nu(z-1)} \tag{III.11}$$

an analogous expression

$$\rho(H) \propto \mid H - H_m \mid^{\nu(z-1)} \tag{III.12}$$

was used to determine the melting field H_m (also called H_g in the previous section). The melting field, H_m, and critical exponent, ν(z-1), can then be obtained from the linear extrapolation of the data using the equation:

$$\left(\frac{dln\rho}{dH}\right)^{-1} = \frac{H - H_m}{\nu(z-1)} \tag{III.13}$$

and plotting (dln ρ/dH)$^{-1}$ vs H. The data obtained can be summarized in a plot of the vortex glass melting field H_m(T) as a function of angle, Θ, shown in Fig. III.19.

The critical exponent ν(z-1) appears to be independent of angle. However, it was found that $H_m(\Theta)$ follows the form

$$H_m(\Theta) = \frac{H_m(0)}{\varepsilon^2(\Theta)}, \tag{III.14}$$

where

$$\varepsilon^2(\Theta) = cos^2(\Theta) + \gamma^{-2} sin^2(\Theta) \tag{III.15}$$

for each temperature T, instead of the predicted form [84]

$$H_m(\Theta) = \frac{H_m(0)}{\varepsilon}. \tag{III.16}$$

The coefficient γ^2 is defined as the mass anisotropy ratio

$$\gamma^2 = \left(\frac{m_c}{m_{ab}}\right). \tag{III.17}$$

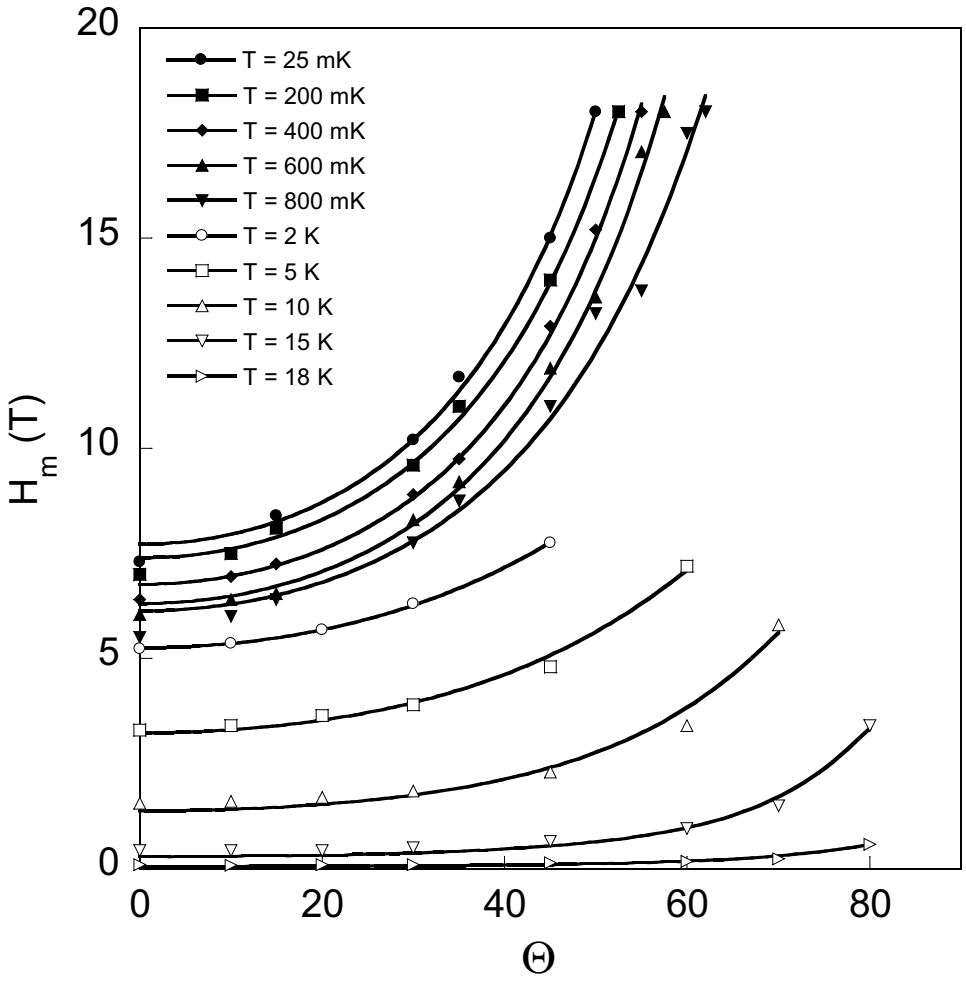

Figure III.19: Angle dependence of the vortex glass melting field, $H_m(T)$, versus Θ at several isotherms for an optimally doped (x = 0.15) film. Solid lines are fits to the expression $H_m(\Theta) = H_m(0)/\varepsilon^2$, where $\varepsilon^2 = \cos^2(\Theta) + \gamma^{-2}\sin^2(\Theta)$.

From the data, a value for the mass anisotropy ratio, $\gamma \approx 3$ was obtained. This compares quite well to the value obtained in a previous study on magnetically aligned single crystal grains of SCCO where γ was determined from analysis of reversible dc magnetization measurements, M(H,T), and was found to be ≈ 3.7 [85].

The angular dependence of the vortex glass melting temperature H_m of the high temperature superconductor YBCO was shown to follow Eqn.(III.16) [86, 87]. However, there have been reports of anomalous behavior for the highly anisotropic high-T_c compound $Bi_2Sr_2CaCu_2O_{8+y}$ (BSCCO) [88]. The authors found that their data can be fit by the expression

$$H_m(\Theta) \propto \frac{H_m(0)}{cos(\Theta) + \gamma^{-2} sin(\Theta)}. \qquad \text{(III.18)}$$

Both SCCO and BSCCO appear to have anomalous behavior and do not follow Eqn.(III.16); therefore, it seems that the physics behind the behavior of these compounds needs to be addressed through new theory for the angular dependence of the vortex glass melting line.

A portion of the text and data in this chapter is a reprint of the material as it appears in "Growth via Pulsed Laser Deposition and Characterization of Thin Films of the Electron-Doped Superconductor $Sm_{2-x}Ce_xCuO_{4-y}$," D. J. Scanderbeg, B. J. Taylor, and M. B. Maple, Physica C **443**, 38 (2006). The dissertation author was the primary investigator and author of this article.

IV

Summary and Conclusions

IV.1 Summary and Conclusions

High quality c-axis oriented thin films of the electron-doped superconductor $Sm_{2-x}Ce_xCuO_{4-y}$ have been grown by pulsed laser deposition over a range of cerium dopings, $0.13 \leq x \leq 0.19$. The growth conditions for these films have been established and are reported along with the superconducting critical temperature, T_c, for each doping. A transition temperature-concentration, T_c-x, phase diagram has also been established from the data for each film. The T_c-x diagram is nearly identical to the related electron-doped compounds NCCO and PCCO and displays an asymmetric superconducting dome. There is a rapid increase in T_c from the underdoped to optimally doped ($x = 0.15$) film and then a slower suppression of T_c with increased doping ($x > 0.15$).

X-ray data has shown the quality and c-axis orientation of the films and SEM images have also emphasized the quality and smoothness of the films. Magnetoresistance measurements were carried out as a function of doping as well as thermopower measurements. Thermopower measurements show a change in sign of the charge carrier from the underdoped region to the overdoped region consistent with PCCO [77] thin films, impling that a two-band model applies to the SCCO system.

The FFH vortex glass scaling model was applied to the magnetoresistance

data but was found to not fit the data as well as the RRA modified vortex glass scaling model. The fits to the data yielded a vortex glass melting transition line for all the $Sm_{2-x}Ce_xCuO_{4-y}$ films that could be measured (x $\geq$ 0.14). These results are similar to the results obtained from analysis of NCCO samples [**?**,81–83]. The critical exponent associated with the vortex glass transition, ν(z-1), is seen to have a lower value for the underdoped x = 0.14 film. This leads to the possibility of the critical exponent having a dependence on the cerium content. Additional measurements on underdoped films are needed to confirm a consistently lower critical exponent for the underdoped films. Finally, an anomalous angular dependence of the vortex glass melting transition has been found that does not conform to the expression given by Blatter et. al. [84]. This is the second compound found to not follow this expression, the other being $Bi_2Sr_2CaCu_2O_{8+y}$ (BSCCO) [88], and new theory is needed to taken into account the behavior of these compounds.

Throughout this body of work, it is found that the effects of antiferromagnetism, associated with the Sm^{3+} ions, on the vortex glass melting transition are not readily apparent in this system. There was not any significant change in the vortex glass melting temperature, T_g, or the critical exponent, ν(z-1), above or below the Néel temperature, $T_N \sim 6$ K. Measurements of the angular dependence of the vortex glass melting line also showed no significant change in T_g or ν(z-1) above or below the Néel temperature.

IV.2 Opportunities for Future Work

There are still many opportunities for future work on $Sm_{2-x}Ce_xCuO_{4-y}$ and are discussed below.

IV.2.1 Dilution refrigerator experiments

The very underdoped region, x < 0.14, with low critical temperatures $T_c \lessapprox 2$ K, can only be accessed and reasonably studied with low temperature

apparatus such as a ^{3}He - ^{4}He dilution refrigerator. With such equipment, the low temperature limits of measurement could be pushed close to 25 mK. Likewise, delving further into the overdoped region would also decrease T_c and also lead to the need for very low temperature measurements.

Low temperatures and high magnetic fields could also extend the vortex glass melting lines near the vicinity of the upper critical field H_{c2}. This would be interesting as it is unclear what happens to the vortex glass melting lines near the upper critical field. SCCO is also a good material candidate for this work since it has an upper critical field $H_{c2} \leq 20$ T. Therefore, the high magnetic fields needed would be $H \lesssim 20$ T, which is easily attainable at certain facilities, such as Los Alamos National Laboratory (LANL) or the National High Magnetic Field Laboratory at Tallahassee (NHMFL). This is contrasted to the example of YBCO where H_{c2} is estimated to be much larger than 100 T.

Extending the vortex glass melting lines would also help confirm if there is a consistently smaller value of the critical exponent at low cerium doping levels ($x < 0.15$).

IV.2.2 Hall effect

The Hall effect is a key measurement useful in identifying both the sign of the charge carrier in a material as well as the carrier concentration. There have been numerous studies of the Hall effect on some of the electron-doped compounds [46,70,76,89,90]. Early reports of measurements yielded a negative Hall coefficient but later there were reports of a sign change in the Hall coefficient suggesting the carriers were in fact holes. Recent work on both NCCO [91] and PCCO [92] has led to the explanation of a two-band model. Hall effect measurements on SCCO could confirm the results obtained from thermopower measurements, as discussed in section III.1.3, and provide comparison to Hall data taken on both NCCO and PCCO.

IV.2.3 Collaborations

Several proposed collaborations include optical spectroscopy measurements (Prof. D. Basov - UCSD), neutron scattering experiments (Prof. S. Sinha - UCSD), and penetration depth measurements (Prof. T. Lemberger - Ohio State). However, each measurement has its own requirements for the physical properties of the samples leading to various "materials" problems. For example, for optical spectroscopy measurements such as transmission, only certain substrates can be that are transparent over a certain frequency range. Magnesium oxide (MgO) is one of these substrates; however, numerous attempts with varying growth conditions failed to achieve growth of a film on this substrate. Once these "materials" problems are overcome, hopefully these collaborations, and the information they will provide, will give insight into the SCCO system and, more generally, high temperature superconductivity in the electron-doped compounds.

V

Appendix

V.1 Appendix A

There are numerous ways to calculate the starting weights of the materials needed to prepare a final compound, whether it be in the form of a flux grown single crystal or polycrystalline sample; in this case, a polycrystalline PLD target (pellet). Everyone seems to have their own method and this is easily confirmed in a laboratory such as our with several different people working on several different projects involving the growth of new materials.

The method described here was employed because of the critical nature of the doped element; as we have seen, a small change in Ce content, or rather the Ce to Sm ratio, can make a very large difference in T_c. Therefore, this method centered around the element with the smallest mole fraction in the final compound, in our case the doped atom (Ce). This ensured the best accuracy since this element would be weighed out and then the other materials would be weighed out relative to it. A general description and procedure is described below followed by a specific example for one of the SCCO targets.

Starting with the general formula of a compound, one must calculate its molecular weight and then decide the final weight desired. The general form for the reaction of oxides is:

$$\alpha X_a O_{a'} \ + \ \beta Y_b O_{b'} \ + \ \gamma Z_c O_{c'} = X_l Y_m Z_n ... O_x \tag{V.1}$$

where $X_a O_{a'}$ will be the oxide with the smallest mole fraction in the final compound and $Y_b O_{b'}$ and $Z_c O_{c'}$ are the other oxides in the compound. Other definitions used include: x = calculated weight of $X_a O_{a'}$, y = calculated weight of $Y_b O_{b'}$, z = calculated weight of $Z_c O_{c'}$, $\underline{x}$ = measured weight of $X_a O_{a'}$, and $[X_a O_{a'}]_{MW}$ = molecular weight of $X_a O_{a'}$, etc.

Therefore, to find the weight x of the element with the smallest final mole fraction, we employ the formula:

$$x = \alpha w \frac{[X_a O_{a'}]_{MW}}{[X_l Y_m Z_n ... O_x]_{MW}} \tag{V.2}$$

Then, $X_a O_{a'}$ is weighed ($\underline{x}$), close to the calculated amount (x). Having an actual weight for $X_a O_{a'}$, calculation of the weights of the other starting oxides follows from the following equations:

$$y = \underline{x} \left(\frac{[Y_b O_{b'}]_{MW}}{[X_a O_{a'}]_{MW}} \right) \left(\frac{a}{b} \right) \left(\frac{m}{l} \right) \tag{V.3}$$

$$z = \underline{x} \left(\frac{[Z_c O_{c'}]_{MW}}{[X_a O_{a'}]_{MW}} \right) \left(\frac{a}{c} \right) \left(\frac{n}{l} \right) \tag{V.4}$$

Specifically, we can see how the calculation works for $Sm_{1.85}Ce_{0.15}CuO_{4-y}$. The molecular weight is 426.8016 g/mole. A total weight of 12 g was found to correspond to a good target size once pressed into a pellet with a 3/4" die, so the desired final weight is 12 g. The oxides used are CeO_2, Sm_2O_3, and CuO. The reaction formula is then,

$$0.15 CeO_2 \ + \ 0.925 Sm_2O_3 \ + \ CuO \ = \ Sm_{1.85}Ce_{0.15}CuO_4. \tag{V.5}$$

Again, for SCCO, the element with the smallest final mole fraction is Ce, so we want to calculate x for CeO_2.

$$x = (0.15)(12\ g)\left(\frac{172.1188\ g/mole}{426.8016\ g/mole}\right) = 0.7259\ g \tag{V.6}$$

So if the actual weight measured is $\underline{x} = 0.7263$ g, then we can find the weights of Sm_2O_3 and CuO to be used:

$$y = (0.7263)\left(\frac{348.7982\ g/mole}{172.1188\ g/mole}\right)\left(\frac{1}{2}\right)\left(\frac{1.85}{0.15}\right) = 9.0764\ g \tag{V.7}$$

and

$$z = (0.7263)\left(\frac{79.5454\ g/mole}{172.1188\ g/mole}\right)\left(\frac{1}{1}\right)\left(\frac{1}{0.15}\right) = 2.2377\ g. \tag{V.8}$$

VI

Bibliography

[1] S. D. Wilson, P. Dai, S. Li, S. Chi, H. J. Kang and J. W. Lynn, Nature **442**, 59 (2006).

[2] S. D. Wilson, S. Li, H. Woo, P. Dai, H. A. Mook, C. D. Frost, S. Komiya and Y. Ando, Phys. Rev. Lett. **96**, 157001 (2006).

[3] J. F. Ready, Appl. Phys. Lett. **3**, 11 (1963).

[4] R. M. White, J. Appl. Phys. **34**, 3559 (1963).

[5] G. A. Askar'yan, A. M. Pokhorov, G. F. Chantutiya and G. P. Shipulo, Sov. Phys. JETP **17**, 6 (1963).

[6] R. G. Meyerand and A. F. Haught, Phys. Rev. Lett. **9**, 403 (1963).

[7] H. M. Smith and A. F. Turner, Appl. Opt. **4**, 147 (1965).

[8] D. Dijkkamp, T. Venkatesan, X. D. Wu, S. A. Shaheen, N. Jisrawi, Y. H. Min-Lee, W. L. McLean and M. Croft, Appl. Phys. Lett. **51**, 619 (19870.

[9] D. H. A. Blank, R. P. J. Ijsselsteijn, P. G. Out, H. J. H. Kuiper, J. Floksura and H. Rogalla, Mat. Sci. Eng. **B13**, 67 (1992).

[10] W. Kautek, B. Roas and L. Schultz, Thin Solid Films **191**, 317 (1990).

[11] B. Lewis and J. C. Anderson, *Nucleation and Growth of Thin Films* (Academic Press, New York, 1978).

[12] H. Kamerlingh Onnes, Leiden Comm. **120b, 122b, 124c** (1911).

[13] W. Meissner and R. Oschenfeld, Naturwissenschaften **21**, 787 (1933).

[14] F. London and H. London, Proc. Roy. Soc. **A149**, 71 (1935).

[15] V. L. Ginzburg and L. D. Landau, Zh. Eksperim. i Teor. Fiz. **20**, 1064 (1950).

[16] L. P. Gor'kov, Zh. Eksperim. i Teor. Fiz. **36**, 1918 (1959).

[17] G. Bednorz and K. A. M*ü*ller, Z. Phys. **B64**, 189 (1986).

[18] M. B. Maple, J. Magn. Magn. Mater. **177-181**, 18 (1998).

[19] D. S. Fisher, M. P. A. Fisher and D. A. Huse, Phys. Rev. B. **43**, 130 (1991).

[20] C. Kittel, *Introduction to Solid State Physics* 7^{th} ed. (John-Wiley and Sons, New York, 1996).

[21] M. Tinkham, *Introduction to Superconductivity* 2^{nd} ed. (McGraw-Hill, New York, 1996).

[22] K. H. Bennemann and J. B. Ketterson eds., *The Physics of Superconductors - Vol. I: Conventional and High-T_c Superconductors* (Springer, Berlin, 2003).

[23] J. Bardeen, L. N. Cooper and J. R. Schrieffer, Phys. Rev. **108**, 1175 (1957).

[24] A. A. Abrikosov, Zh. Eksperim. i Teor. Fiz. **32**, 1442 (1957).

[25] U. Essmann and H. Tr*ä*uble, Phys. Lett. **24A**, 526 (1967).

[26] H. F. Hess, R. B. Robinson, R. C. Dynes, J. M. Valles, Jr. and J. V. Waszczak, Phys. Rev. Lett. **62**, 214 (1989).

[27] H. F. Hess, R. B. Robinson and J. V. Waszczak, Phys. Rev. Lett. **64**, 2711 (1990).

[28] J. Bardeen and M. J. Stephen, Phys. Rev. **140**, A1197 (1968).

[29] P. W. Anderson, Phys. Rev. Lett. **9**, 309 (1962).

[30] P. W. Anderson and Y. B. Kim, Rev. Mod. Phys. **36**, 39 (1964).

[31] Y. B. Kim, C. F. Hempstead and A. R. Strnad, Phys. Rev. Lett. **9**, 306 (1962).

[32] M. P. A. Fisher, Phys. Rev. Lett. **62**, 1415 (1989).

[33] J. Herrmann, M. C. de Andrade, C. C. Almasan, R. P. Dickey, M. B. Maple, W. Jiang, S. N. Mao and R. L. Greene, Phys. Rev. B **54**, 3610 (1996).

[34] A. Schilling, M. Cantoni, J. D. Guo and H. R. Ott, Nature **363**, 56 (1993).

[35] R. J. Cava, R. B. van Dover, B. Batlogg and E. A. Rietman, Phys. Rev. Lett. **58**, 408 (1987).

[36] Y. Tokura, H. Takagi and S. Uchida, Nature **337**, 345 (1989).

[37] G. M. Luke, L. P. Le, B. J. Sternlieb, Y. J. Uemura, J. H. Brewer, R. Kadono, R. F. Kiefl, S. R. Kreitzman, T. M. Riseman, C. E. Stronach, M. R. Davis, S. Uchida, H. Takagi, Y. Tokura, Y. Hidaka, T. Murakami, J. Gopalakrishnan, A. W. Sleight, M. A. Subramanian, E. A. Early, J. T. Markert, M. B. Maple and C. L. Seaman, Phys. Rev. B **42**, 7981 (1990).

[38] J. M. Tranquada, S. M. Heald, A. R. Moodenbaugh, F. Liang and M. Croft, Nature **337**, 720 (1989).

[39] Y. J. Uemura, G. M. Luke, B. J. Sternlieb, L. P. Le, J. H., Brewer, R. Kandono, R. F. Kiefl, S. R. Kreitzman, T. M. Riseman, C. L. Seaman, J. J. Neumeier, Y. Dalichaouch, M. B. Maple, G. Saito and H. Yamochi, in *Dynamics of Magnetic Fluctuations in High-Temperature Superconductors* (Plenum Press, New York, 1991).

[40] K. Katsumata, J. Tuchendler, Y. J. Uemura and H. Yoshizawa, Phys. rev. B **37**, 356 (1988).

[41] R. A. Cowley, G. Shirane, R. J. Birgeneau and H. J. Guggenheim, Phys. Rev. B **15**, 4292 (1977).

[42] J. T. Markert and M. B. Maple, Solid State Comm. **70**, 145 (1989).

[43] J. T. Markert, E. A. Early, T. Bjørnholm, S. Ghamaty, B. W. Lee, J. J. Neumeier, R. D. Price, C. L. Seaman and M. B. Maple, Physica C **158**, 178 (1989).

[44] E. A. Early, N. Y. Ayoub, J. Beille, J. T Markert and M. B. Maple, Physica C **160**, 320 (1989).

[45] M. B. Maple, MRS Bulletin **15**, 60 (1990).

[46] H. Takagi, S. Uchida and Y. Tokura, Phys. Rev. Lett. **62**, 1197 (1989).

[47] E. Maiser, P. Fournier, J. -L. Peng, F. M. Araujo-Moreira, T. Venkatesan, R. L. Greene and G. Czjzek, Physica C **297**, 15 (2003).

[48] M. B. Maple, N. Y. Ayoub, T. Bjørnholm, E. A. Early, S. Ghamaty, B. W. Lee, J. T. Markert, J. J. Neumeier and C. L. Seaman, Physica C **164**, 296 (1989).

[49] J. W. Lynn, I. W. Sumarlin, S. Skanthakumar, W-H. Li, R. N. Shelton, J. L. Peng, Z. Fisk and S-W. Cheong, Phys. Rev. B **41**, 2569 (1990).

[50] I. W. Sumarlin, S. Skanthakumar, J. W. Lynn, J. L. Peng, Z. Y. Li, W. Jiang and R. L. Greene, Phys. Rev. Lett. **68**, 2228 (1992).

[51] B. T. Matthias, E. Corenzwit, J. M. Vandenberg and H. E. Barz, Proc. Nat. Acad. Sci. **74**, 1334 (1977).

[52] J. M. Vandenberg and B. T. Matthias, Proc. Nat. Acad. Sci. **74**, 1336 (1977).

[53] M. B. Maple and Ø. Fisher eds., *Superconductivity in Ternary Compounds II* (Springer-Verlag, New York, 1982).

[54] H. C. Hamaker, L. D. Woolf, H. B. MacKay, Z. Fisk and M. B. Maple, Solid State Comm. **32**, 289 (1979).

[55] R. Vaglio, B. D. Terris, J. F. Zasadzinski and K. E. Gray, Phys. Rev. Lett. **53**, 1489 (1984).

[56] S. E. Lambert, M. B. Maple and B. D. Dunlap, Phys. Rev. B **33**, 3129 (1986).

[57] Y. Dalichaouch, B. W. Lee, C. L. Seaman, J. T. Markert and M. B. Maple, Phys. Rev. Lett. **64**, 599 (1990).

[58] M. Cagigal, J. Fontcuberta, M. A. Crusellas, J. L. Vincent and S. Pinol, Phys. Rev. B **50**, 15993 (1994).

[59] Y. Dalichaouch, M. C. de Andrade and M. B. Maple, Physica C **218**, 309 (1993).

[60] Y. Dalichaouch, C. L. Seaman, C. C. Almasan, M. C. de Andrade, H. Iwasaki, P. K. Tsai and M. B. Maple, Physica B **171**, 308 (1991).

[61] Y. Lu, R. A. Hughes, T. Strach, T. Timusk, D. Poulin and J. S. Preston, Physica C **197**, 75 (1992).

[62] S. N. Mao, Jian Mao, X. X. Xi, D. H. Wu, Qi Li, S. M. Anlage, T. Venkatesan and X. D. Wu, IEEE Transactions on Applied Superconductivity **5**, 1347 (1995).

[63] E. A. Early, *Ph.D. Thesis* University of California, San Diego (1991).

[64] S. N. Mao, X. X. Xi, S. Bhattacharya, Qi Li, T. Venkatesan, J. L. Peng, R. L. Greene, Jian Mao, Dong Ho Wu and S. M. Anlage, Appl. Phys. Lett. **61** 2356 (1992).

[65] S. I. Woods, A. S. Katz, T. L. Kirk, M. C. de Andrade, M. B. Maple and R. C. Dynes, IEEE Transactions on Applied Superconductivity **9** 3917 (1999).

[66] S. I. Woods, *Ph.D. Thesis* University of California, San Diego (1998).

[67] A. Gupta, G. Koren, C. C. Tsuei, A. Segmuller and T. R. McGuire, Appl. Phys. Lett. **55**, 1795 (1989).

[68] A. Gupta, R. Gross, F. Olson, A. Segmuller, G. Koren and C. C. Tsuei, Phys. Rev. Lett. **64**, 3191 (1990).

[69] D. Prasad Beesabathina, L. Salamanca-Riba, S. N. Mao, X. X. Xi and T. Venkatesan, Appl. Phys. Lett. **62**, 3022 (1993).

[70] W. Jiang, J. L. Peng, Z. Y. Li and R. L. Greene, Phys. Rev. B **47**, 8151 (1993).

[71] P. Richard, G. Riou, I. Hetel, S. Jandl, M. Poirier and P. Fournier, Phys. Rev. B **70**, 064513 (2004).

[72] G. Riou, P. Richard, S. Jandl, M. Poirier and P. Fournier, Phys. Rev. B **69**, 024511 (2004).

[73] P. Richard, M. Poirier, S. Jandl and P. Fournier, Phys. Rev. B **72**, 184514 (2005).

[74] H. J. Kang, P. Dai, B. J. Campbell, P. J. Chupas, S. Rosenkranz, P. L. Lee, Q. Huang, S. Li, S. Komiya and Y. Ando, Nature Materials **6**, 224 (2007).

[75] C. C. Tsuei, A. Gupta and G. Koren, Physica C **161**, 415 (1989).

[76] H. S. Yang, Y. S. Chai, J. Liu, M. Yu, P. C. Li, L. Zhang, M. D. Li and L. Z. Cao, Physica C **403**, 203 (2004).

[77] P. Li, K. Behnia and R. L. Greene, arXiv:cond-mat **0611385** (2006).

[78] A. Rydh, Ö. Rapp and M. Andersson, Phys. Rev. Lett. **83**, 1850 (1992).

[79] M. Andersson, A. Rydh and Ö. Rapp, Phys. Rev. B **63**, 184511 (2001).

[80] M. C. de Andrade, C. C. Almasan, Y. Dalichaouch and M. B. Maple, Physica C **184**, 378 (1991).

[81] N.-C. Yeh, W. Jiang, D. S. Reed, A. Gupta, F. Holtzberg and A. Kussmaul, Phys. Rev. B **45**, 5710 (1992).

[82] J. M. Roberts, Brandon Brown, J. Tate, X. X. Xi and S. N. Mao, Phys. Rev. B **51**, 15281 (1995).

[83] O. M. Stoll, A. Wehner, R. P. Huebener and M. Naito, Physica C **363**, 31 (2001).

[84] G. Blatter, V. B. Geshkenbein and A. I. Larkin, Phys. Rev. Lett. **68**, 875 (1992).

[85] C. C. Almasan, S. H. Han, E. A. Early, B. W. Lee, C. L. Seaman and M. B. Maple, Phys. Rev. B **45**, 1056 (1992).

[86] R. G. Beck, D. E. Farrell, J. P. Rice, D. M. Ginsberg and V. G. Kogan, Phys. Rev. Lett. **68**, 1594 (1992).

[87] W. K. Kwok, S. Fleshler, U. Welp, V. M. Vinokur, J. Downey, G. W. Crabtree and M. M. Miller, Phys. Rev. Lett. **69**, 3370 (1992).

[88] S. Ooi, T. Shibauchi, N. Okuda and T. Tamegai, Phys. Rev. Lett. **82**, 4308 (1999).

[89] W. Jiang, S. N. Mao, X. X. Xi, X. Jiang, J. L. Peng, T. Venkatesan, C. J. Lobb and R. L. Greene, Phys. Rev. Lett. **73**, 1291 (1994).

[90] P. Fournier, X. Jiang, S. N. Mao, T. Venkatesan, C. J. Lobb and R. L. Greene, Phys. Rev. B **56**, 14149 (1997).

[91] C. H. Wang, G. Y. Wang, T. Wu, Z. Feng, X. G. Luo and X. H. Chen, arXiv:cond-mat **0506681** (2005).

[92] Y. Dagan, M. M. Qazlibash, C. P. Hill, V. N. Kulkarni and R. L. Greene, Phys. Rev. Lett. **92**, 167001 (2004).